

Calibration techniques for quantitative NO measurement using Laser-Induced Fluorescence

Marie Meulemans^{a,*}, Antoine Durocher^{a,b}, Philippe Versailles^c, Gilles Bourque^a,
Jeffrey M. Bergthorson^a

^a*Alternative Fuels Laboratory, McGill University, 817 Sherbrooke St W, Montréal, H3A 0C3, QC, Canada*

^b*Propulsion and Power Laboratory, National Research Council of Canada, 1200 Montréal Road, Ottawa, K1K 2E1, ON, Canada*

^c*Polytechnique Montréal, 2500 Chemin de Polytechnique, Montréal, H3T 1J4, QC, Canada*

Abstract

Laser-Induced Fluorescence (LIF) is an essential optical diagnostic technique for the high-resolution and low-uncertainty measurement of combustion species concentration in a variety of applications and conditions. Two different calibration techniques are explored in this study to obtain quantitative Nitric Oxide (NO) concentration measurements in flames. The first technique, the most employed in the literature, uses the extrapolation of the fluorescence signal from seeded to nascent NO and is only valid under negligible NO reburn conditions. The second technique uses the optical calibration of the experimental setup to relate it to a modelled LIF signal and can be applied regardless of NO reburn. Both of these techniques are explored under two different assumptions: constant and non-constant interfering LIF signal on the NO absorption spectrum. While the former is most often used in the literature, the latter is necessary when the LIF signal from interfering species cannot be distinguished from the NO-LIF signal, especially in high pressure conditions. Hence, a total of four techniques are presented in this work and are found to be in excellent agreement when performed in different flame conditions. The calibration techniques are applied to three lean, atmospheric, laminar, premixed, methane-air flames to explore their field of applicability. Specifically, the study explores the relevance of the techniques in reburn conditions, which occur mostly in high pressure, rich, highly-seeded, or NH₃-containing flames. This study aims to offer the reader a portfolio of calibration techniques to use according to the conditions in which they need to be applied. While this study was carried out measuring NO concentration in a stagnation flame burner, the concepts and equations presented can be transposed to the measurement of other species and to other experimental configurations.

Keywords: Laser-Induced Fluorescence, Nitric Oxide, NO-LIF calibration, Optical diagnostics, Combustion

*Corresponding author.

Email addresses: marie.meulemans@mail.mcgill.ca (Marie Meulemans), antoine.durocher@nrc-cnrc.gc.ca (Antoine Durocher), philippe.versailles@polymtl.ca (Philippe Versailles), gilles.bourque@mcgill.ca (Gilles Bourque), jeffrey.bergthorson@mcgill.ca (Jeffrey M. Bergthorson)

Nomenclature

Acronyms

BC	Boundary Condition
CRDS	Cavity Ring-Down Spectroscopy
CRECK	Chemical Reaction Engineering and Chemical Kinetics thermochemical model
DC	Dry-piston Calibrator
EET	Electronic Energy Transfer
GRI	Gas Research Institute thermochemical model
HWHM	Half-Width at Half-Maximum
LIF	Laser-Induced Fluorescence
LS	Logarithmic Sensitivity
MC	Monte-Carlo
MFC	Mass Flow Controller
PTV	Particle Tracking Velocimetry
RET	Rotational Energy Transfer
RMSE	Root Mean Square Error
RPA	Reaction Pathway Analysis
RSS	Root Square Sum
SD	San Diego thermochemical model
VET	Vibrational Energy Transfer

Greek Symbols

Γ	Overlap fraction	[-]
$\Delta\nu_L$	Laser spectral linewidth	[cm ⁻¹]
$\delta(\cdot)$	Total absolute uncertainty of quantity (\cdot)	[n/a]
$\delta_{\text{rand}}(\cdot)$	Absolute random uncertainty of quantity (\cdot)	[n/a]
$\delta_{\text{sys}}(\cdot)$	Absolute systematic uncertainty of quantity (\cdot)	[n/a]
$\epsilon(\cdot)$	Total relative uncertainty of quantity (\cdot)	[%]
$\epsilon_{\text{rand}}(\cdot)$	Relative random uncertainty of quantity (\cdot)	[%]
$\epsilon_{\text{sys}}(\cdot)$	Relative systematic uncertainty of quantity (\cdot)	[%]
λ	Wavelength	[nm]
ν	Frequency of light	[s ⁻¹]

ν''	Vibrational level in the ground state	[-]
ν'	Vibrational level in the excited state	[-]
ρ_{in}	Density of the inlet mixture	[kg·m ⁻³]
τ_2	Average lifetime of the excited molecule in state 2	[s]
τ_{pulse}	Duration of the laser pulse	[s]
ϕ	Equivalence ratio	[-]
Ω	Collection solid angle	[sr]

Roman Symbols

A	Cross-section of the laser beam	[m ²]
A_{nozzle}	Cross-section of the burner nozzle	[m ²]
A_{ul}	Einstein rate constant of spontaneous emission from an upper state u to a lower state l	[s ⁻¹]
B_{lu}	Einstein absorption coefficient from a lower state l to an upper state u	[m ² ·J ⁻¹ ·s ⁻¹]
c	Speed of light	[m·s ⁻¹]
C_{bckgd}	Background coefficient	[-]
C_{lin}	Linear calibration coefficient	[J ⁻¹ ·ppm ⁻¹]
C_{opt}	Optical calibration coefficient	[m]
du_{in}/dz	Inlet axial strain rate of the mixture	[s ⁻¹]
E_L	Incident laser energy per pulse	[J]
\mathcal{E}_c	Quantum efficiency of the camera	[count·photon ⁻¹]
f_B	Boltzmann fraction	[-]
F_{bckgd}	Background LIF signal encompassing interfering LIF and laser-related noise, normalised by the laser energy	[J ⁻¹]
F_{dark}	Signal from the camera dark noise, flame chemiluminescence, and ambient light, normalised by the laser energy	[J ⁻¹]
$F_{fluo.}$	Total fluorescence signal captured by the camera, normalised by the laser energy	[J ⁻¹]
$F_{interf.-LIF}$	Interfering LIF signal that does not originate from the excitation of the NO molecule, normalised by the laser energy	[J ⁻¹]
f_{LIF}	LIF modelling parameter	[J·s ⁻¹ ·m ⁻¹]
F_{NO-LIF}	Fluorescence signal of the laser-excited NO molecule, normalised by the laser energy	[J ⁻¹]
$F_{NO-LIF,nsct}$	Fluorescence signal of the laser-excited NO molecule, normalised by the laser energy, of an unseeded flame representative of the nascent (nsct) NO	[J ⁻¹]

$F_{\text{NO-LIF,nsct+sd}}$	Fluorescence signal of the laser-excited NO molecule, normalised by the laser energy, of a seeded flame representative of the nascent (nsct) and seeded (sd) NO	$[\text{J}^{-1}]$
$F_{\text{NO-LIF,sd}}$	Fluorescence signal of the laser-excited NO molecule, normalised by the laser energy, of an unseeded flame subtracted off the signal of a seeded flame, representative of the seeded (sd) NO	$[\text{J}^{-1}]$
$g(\nu)$	Spectral lineshape function of the absorption transition	$[\text{s}]$
g_i	Degeneracy of state i	$[-]$
h	Planck's constant	$[\text{J}\cdot\text{s}]$
I	Incident laser irradiance	$[\text{W}\cdot\text{m}^{-2}]$
J''	Rotational number of the ground state	$[-]$
J'	Rotational number of the excited state	$[-]$
$L(\nu)$	Laser spectral distribution	$[-]$
\mathcal{L}	Length of the flame domain used for simulations	$[\text{mm}]$
ℓ	Length of laser path in the measurement volume	$[\text{m}]$
M	Target molecule in the ground state and in the excited state (superscript *)	$[-]$
\dot{m}_g	Mass flow rate of a gas g	$[\text{g}\cdot\text{s}^{-1}]$
MW_g	Molar weight of gas g	$[\text{g}\cdot\text{mol}^{-1}]$
\mathcal{N}_A	Avogadro's number	$[\text{mol}^{-1}]$
n_i°	Number density of the molecule in each state i before laser excitation	$[\text{m}^{-3}]$
n_i	Number density of the molecule in each state i following laser excitation	$[\text{m}^{-3}]$
n_T°	Total number density of the molecule M in the measurement volume, prior to laser excitation	$[\text{m}^{-3}]$
\dot{N}_s	Molar flow rate of species s	$[\text{mol}\cdot\text{s}^{-1}]$
p	Pressure	$[\text{Pa}]$
Q_{ul}	Rate constant of collisional quenching from an upper state u to a lower state l	$[\text{s}^{-1}]$
\mathcal{R}_u	Universal gas constant	$[\text{J}\cdot\text{mol}^{-1}\cdot\text{K}^{-1}]$
R_{ul}	Rate of rotational energy transfer from a state u to a state l (reversible)	$[\text{s}^{-1}]$
S_{BP}	Fluorescence signal of a cold flow of NO captured by the camera at a given laser excitation wavelength	$[\text{count}]$
S_{dark}	Fluorescence signal of a flame captured by the camera without laser excitation	$[\text{count}]$
$S_{\text{fluo.}}$	Fluorescence signal of a flame captured by the camera at a given laser excitation wavelength	$[\text{count}]$
$S_{M-\text{LIF}}$	Fluorescence signal of the laser-excited molecule M	$[\text{count}]$

$\mathcal{S}_{\text{NO-LIF}}$	Fluorescence signal of the laser-excited NO, modelled by LIFSim	[W]
\mathcal{T}_λ	Transmissivity of the optical system	[-]
T	Temperature	[K]
T_{ad}	Adiabatic flame temperature	[K]
T_{in}	Inlet temperature of the mixture	[K]
T_{wall}	Wall temperature of the stagnation plate	[K]
t	Student's distribution score	[-]
u_{in}	Inlet velocity of the mixture	[m·s ⁻¹]
V_{ul}	Rate of vibrational energy transfer from a state u to a state l (reversible)	[s ⁻¹]
W_{lu}	Rate constant of laser-induced stimulated absorption from a lower state l to an upper state u	[s ⁻¹]
W_{sat}	Rate constant of the de-excitation of M^*	[s ⁻¹]
W_{ul}	Rate constant of laser-induced stimulated emission from an upper state u to a lower state l	[s ⁻¹]
$X_{\text{NO,nsct}}$	Molar fraction of nascent (nsct) NO in the flame	[ppm]
$X_{\text{NO,nsct+sd}}$	Total molar fraction of nascent (nsct) and seeded (sd) NO in the flame	[ppm]
$X_{\text{NO,sd}}$	Molar fraction of seeded (sd) NO in the flame	[ppm]
X_s	Molar fraction of species s	[-]
Y_s	Mass fraction of species s	[-]
$Y_{\text{NO,nsct}}$	Mass fraction of nascent (nsct) NO in the flame	[-]
$Y_{\text{NO,nsct+sd}}$	Total mass fraction of nascent (nsct) and seeded (sd) NO in the flame	[-]
$Y_{\text{NO,sd}}$	Mass fraction of seeded (sd) NO in the flame	[-]
z	Axial location in the flame domain	[mm]
z_f	Flame front position	[mm]
z_{in}	Inlet position of the unburnt mixture	[mm]

1. Introduction

At the heart of the current energy transition is the significant reduction in pollutant emissions, for which Nitric Oxide (NO) plays an important role [1]. Highly resolved and low uncertainty NO measurements are needed to develop state-of-the-art models to design energy systems that meet regulatory limits. Measurements have been performed for over a century and have greatly aided the development of combustion models for accurate NO predictions in practical conditions [2–4]. Many techniques have been employed to measure NO in a variety of combusting systems to meet the desired levels of accuracy and resolution, including probe measurements coupled to a gas analyser [5–8] or to a spectrometer [9, 10], broadband absorption spectroscopy [11–14], and, more recently and commonly, laser spectroscopy [15–22].

NO-Laser-Induced Fluorescence (NO-LIF) is a spectroscopy technique that offers *in-situ*, non-intrusive NO measurements with low uncertainty and high resolution down to sub-ppm levels [23]. It is performed by capturing the fluorescence emitted by the NO molecules as they transition from a laser-excited state to a lower-energy state. The light emitted is a function of the state of the molecules (density, temperature, pressure) in the given measurement volume. Thanks to this property, LIF can either be qualitative, *e.g.* the signal of a flame can be directly compared to another; or quantitative. The latter can be achieved through calibration [23–25], where prior knowledge of quantum spectroscopy of the excited molecule may, or may not, be required depending on the selected technique. This work focuses on the quantitative measurement of NO using LIF.

Calibration techniques employed in the literature are revolving around two main strategies: the linear extrapolation from seeded to nascent (*i.e.* naturally produced) NO concentrations, and the calibration of the experimental optical setup using modelled LIF parameters. Their application differs in each study according to the flame conditions in which it is performed and the set of assumptions chosen by the authors. Nevertheless, a review of their span of applicability and the assessment of their accuracy is lacking. This study aims to compare both techniques on a sample set of data. Furthermore, both calibration techniques are usually applied by assuming a spectrally constant interfering LIF signal by species other than NO (O_2 , CO_2 , H_2O , etc), which is only valid at low-pressure conditions. A comparison of both calibration techniques is then performed accounting for the variation of the interfering LIF with the absorption wavelength, as used at high-pressure conditions. Hence, this study compares four techniques to obtain quantitative NO measurements. The intent of this work is not to provide an exhaustive list of NO-LIF calibration techniques, but rather to provide guidance on the applicability of the two main techniques for different experimental conditions and assumptions. The chosen calibration techniques consist of the most commonly used in the literature to obtain quantitative, highly-resolved, low-uncertainty NO measurements.

First, the LIF theory is presented to give context to the assumptions and equations developed in this work. This provides a basis for comparing different calibration techniques used in the literature for quantitative measurements. The experimental configurations and methods are then detailed to be used as a vehicle for the comparison of the calibration techniques presented in subsequent sections. These techniques are introduced by laying out their assumptions and equations. They are then compared using a comprehensive uncertainty analysis. Finally, the advantages and disadvantages of using each technique are summarised, such that this manuscript can be used as a guide for future measurements of NO, or other species concentration, using LIF for various experimental conditions.

2. Fundamentals of Laser-Induced Fluorescence

2.1. LIF theory

This section aims to provide a summary of LIF theory sufficient to support the assumptions and equations used in the calibration techniques described later in this manuscript. The reader is invited to consult several comprehensive reviews of LIF for a deeper understanding of the theory and the fundamentals: Daily [26], Kohse-Höinghaus [24], Eckbreth [23], Laurendeau [27], Hanson *et al.* [28], and Steinberg and Roy [25].

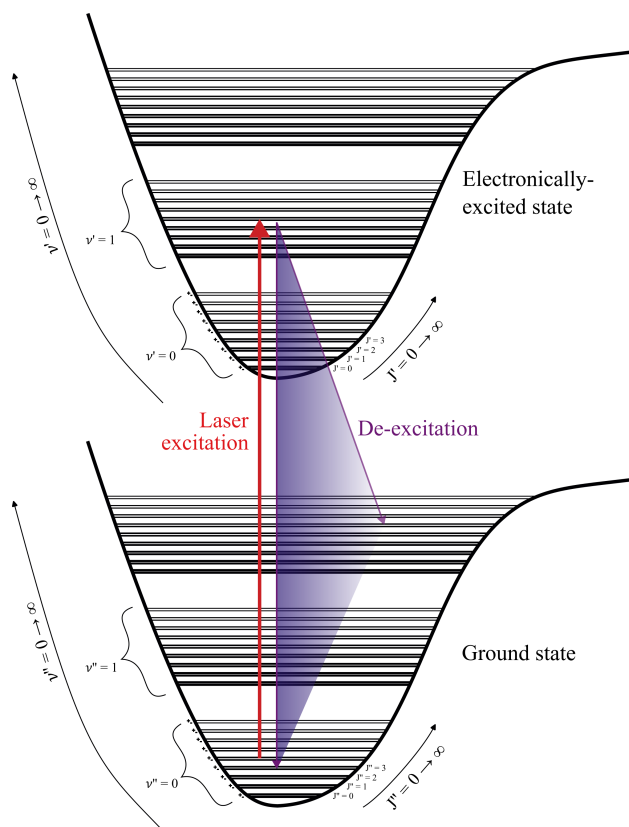


Figure 1: Illustration of LIF process through the representation of two electronic systems, the ground state (superscript $''$) and the excited state (superscript $'$). For each electronic system, several vibrational bands (ν) represent the possible vibrational levels of the excited molecule. Each band is composed of multiple pairs of rotational lines (J). Each pair of rotational line holds a positive (+) and negative (-) parity representing the spin state of the molecule. While laser excitation targets a very specific transition, represented by the red upward arrow, de-excitation can occur to any allowed de-excited state. It is thus represented by a fan-shaped downward arrow.

LIF is a non-intrusive diagnostic technique capturing the fluorescence emitted by laser-excited molecules as they revert back to a lower-energy state, as illustrated in Fig. 1. The fluorescence intensity of the molecules is directly correlated to the state of the target molecule in the measurement volume: density, temperature, and pressure. It also depends on other variables, such as the state of other species present in the measurement volume, the laser energy and efficiency to excite the molecule, and the detection system transmissivity and quantum efficiency, amongst others. Therefore, to translate a fluorescence signal into information about the state of the target molecule, LIF modelling is required. It predicts the rate at which different processes occur, responsible for populating and de-populating the different energy levels and, ultimately, how much

fluorescence is generated. Two main processes are considered in this study: collisions and radiative transitions (W). The first process includes Rotational Energy Transfer (RET), Vibrational Energy Transfer (VET), and Electronic Energy Transfer (EET). The second encompasses the laser-induced stimulated transitions and spontaneous emission. Note that in this study, pre-dissociation and photo-ionisation are neglected as typical energies used for NO-LIF are insufficient to trigger these processes [23, 25, 29–31]. Pre-dissociation refers to the phenomenon wherein the absorption of energy by a multi-atomic molecule results in its dissociation before photon emission occurs. Photo-ionisation denotes a process in which a change in the electronic configuration of a molecule (through the gain or loss of an electron) leads to a molecular ion with an emission spectrum distinct from the neutral molecule.

2.1.1. LIF signal modelling

LIF modelling can predict the transitions between different energy levels, where an energy level represents a possible state of the molecule. The simplest is the 2-level LIF model [23], often employed due to its simple and computationally-efficient description. In this approach, only transitions between the ground-state and a single electronically-excited energy level are considered. More complex models, such as a 3-level NO and O₂-LIF model developed by Bessler *et al.* [32], a 4-level CH-LIF model developed by Versailles [33], a 5-level NO-LIF model developed by Naik and Laurendeau [34], or a 6-level OH-LIF model developed by Verreycken *et al.* [35], consider additional ro-vibrational levels in the ground and electronically excited states, accessible through RET and VET, as well as spontaneous emission and quenching. These models allow more detailed and comprehensive descriptions of the technique with reduced assumptions as compared to the common 2-level LIF model, which is sufficient for most linear LIF configurations [25].

Figure 2 represents the process that the laser-excited molecule undergoes within a 3-level LIF model. For simplicity, RET and VET have been depicted together ($R + V$), although they can occur independently. RET is generally the fastest of the possible energy transfers, and VET is often slower than RET, especially in the ground state [34, 36]. Both RET and VET processes force the molecular population towards a statistical Boltzmann distribution, also called thermalisation. RET, however, is generally negligible when using low laser energies (linear LIF) [34], even in high pressure conditions. Yet, RET has still been included in the following model to correspond to the assumptions made in the LIF modelling software, LIFSim [32], used later in the study.

The process under which LIF occurs in Fig. 2 can be described as follows:

1. A narrow wavelength-tuned laser beam is used to excite a target molecule in the ground state (state 1) known to have a transition at the excitation wavelength. The target molecule, M , absorbs energy to the excited state 2. From state 1 to state 2, M gets excited through radiative transfer, changing its electronic state. The rate at which it occurs is noted W_{12} , the laser-induced stimulated absorption rate constant. The excited molecule, denoted by M^* , will remain in this state for a lifetime τ_2 , on average.
2. Once in state 2, M^* either:
 - returns to its initial ground state 1 through:
 - radiative transfer driven by the rate constant of laser-induced stimulated emission (W_{21}), and by the rate constant of spontaneous emission (A_{21}); or
 - through collisions with other species at the rate constant of collisional quenching (Q_{21}); or

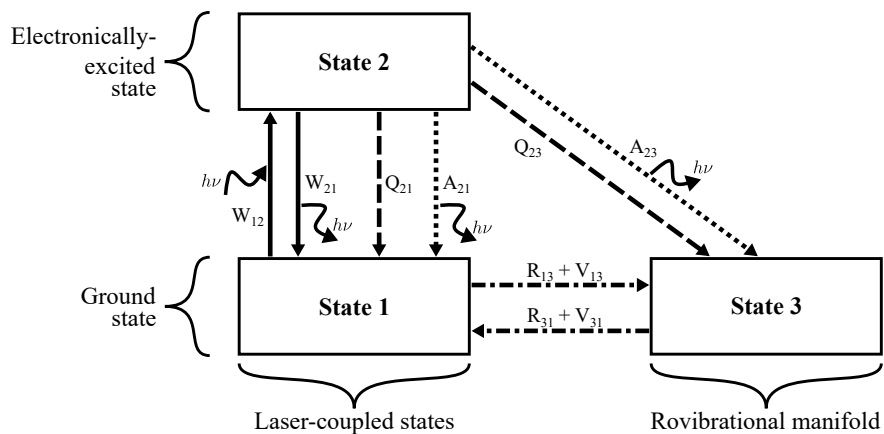


Figure 2: Schematic of a 3-level LIF model. Arrows represent the possible changes of state of the molecule through: laser-induced stimulated absorption (W_{12}) and emission (W_{21}) represented by the solid arrows, collisional quenching (Q_{ul}) represented by the dashed arrows, spontaneous emission (A_{ul}) represented by the dotted arrows, and through ro-vibrational relaxation ($R_{ul} + V_{ul}$) represented by the dot-dashed arrows. RET, VET, and EET in the electronically-excited state are neglected.

- goes to a manifold ground state 3 through spontaneous emission (A_{23}) or collisional quenching (Q_{23}).

3. From state 3, the molecule can undergo ro-vibrational relaxation back to its initial ground state ($R_{31} + V_{31}$).

Any change of state must conform to the allowed transitions. Determining the allowed transitions requires a complex description and understanding of the different quantum numbers of the excited molecule at each state. This is usually done through the use of a LIF modelling software. Ultimately, the description of the population through the different levels, as discussed in this section, elucidates the different sources of fluorescence induced by the laser.

The total fluorescence emitted by the excited molecules is a summation of all fluorescence-emitting transfers (W_{21} , A_{21} , and A_{23}), weighted by the population density of each state (n_i). The latter is calculated according to the rates at which they are either populated or depopulated by the various processes (W , A , and Q). Each of these terms can be calculated independently in order to correlate the total emitted fluorescence with the state of the pre-excited molecule in the measurement volume.

The population density of each state can be obtained through conservation equations:

$$\frac{dn_1}{dt} = -n_1 (W_{12} + R_{13} + V_{13}) + n_2 (W_{21} + Q_{21} + A_{21}) + n_3 (R_{31} + V_{31}); \quad (1)$$

$$\frac{dn_2}{dt} = n_1 W_{12} - n_2 (W_{21} + Q_{21} + A_{21} + Q_{23} + A_{23}); \quad (2)$$

$$\frac{dn_3}{dt} = n_1 (R_{13} + V_{13}) + n_2 (Q_{23} + A_{23}) - n_3 (R_{31} + V_{31}). \quad (3)$$

The sum of these terms results in:

$$\frac{dn_1}{dt} + \frac{dn_2}{dt} + \frac{dn_3}{dt} = 0; \quad (4)$$

hence,

$$n_1 + n_2 + n_3 = n_T^\circ = \text{constant}, \quad (5)$$

where n_T° is the total available population of the species of interest, M , in the measurement volume prior to laser excitation (states 1 and 3).

The rate constant at which the molecule absorbs energy through laser-induced stimulated absorption (W_{12}) is described as follows:

$$W_{12} = \frac{B_{12}}{c} \cdot \frac{I}{\Delta\nu_L} \cdot \Gamma, \quad (6)$$

where B_{12} is the Einstein absorption coefficient of the transition [$\text{m}^2 \cdot \text{J}^{-1} \cdot \text{s}^{-1}$], c is the speed of light [$\text{m} \cdot \text{s}^{-1}$], I is the incident laser irradiance [$\text{W} \cdot \text{m}^{-2}$], $\Delta\nu_L$ is the laser spectral linewidth [cm^{-1}], and Γ is the dimensionless overlap fraction. The incident laser irradiance is defined as:

$$I = \frac{E_L}{A \cdot \tau_{\text{pulse}}}, \quad (7)$$

where E_L is the average laser energy per pulse [J], A is the laser sheet cross-section [m^2], and τ_{pulse} is the laser pulse duration [s]. The dimensionless overlap fraction is defined following the formulation of Partridge and Laurendeau [37]:

$$\Gamma = \int_{\nu} L(\nu) \cdot g(\nu) d\nu, \quad (8)$$

where $L(\nu)$ is the dimensionless laser spectral distribution normalised such that $\int L d\nu = c \cdot \Delta\nu_L$, and $g(\nu)$ is the spectral lineshape function of the absorption transition normalised such that $\int g d\nu = 1$. The overlap fraction is, therefore, a parameter dependent on the laser linewidth and the flame condition through p and T , which influence $g(\nu)$ through Doppler and collisional broadening.

The rate constant at which the excited molecule returns to the ground state through laser-induced stimulated emission (W_{21}) is directly proportional to W_{12} through the degeneracies (*i.e.* the number of states with the same energy level noted g_i) of their respective energy levels:

$$W_{21} = \frac{g_1}{g_2} \cdot W_{12} = \frac{2J'' + 1}{2J' + 1} \cdot W_{12}, \quad (9)$$

where J is the rotational number of the ground (superscript $''$) and excited (superscript $'$) energy level.

The Einstein rate constant of spontaneous emission (A_{ul}) of the molecule transitioning from an upper state (u) to a lower state (l) [s^{-1}] is obtained for each transition [32, 38]. Similarly, the collisional quenching rate constant (Q_{ul}) is obtained empirically for each species contained in the measurement volume.

2.1.2. Linear steady-state LIF model assuming extremely fast RET and VET

For NO-LIF measurements, linear LIF is typically employed as less energy is available to excite interfering species that could lead to background signal in the captured NO fluorescence [39]. It is

also more difficult to reach complete saturation of the NO population, either spatially, temporally, or spectrally, especially in high pressure conditions [23]. For these reasons, the remaining of the study is conducted assuming the linear LIF regime.

In the linear LIF regime, the population in state 2 linearly increases with an increase of the laser irradiance, and is balanced by collisional quenching, the main driver of the lifetime of excited NO in state 2. When the de-excitation mechanisms are much faster ($\tau_2 \sim \frac{1}{\sum Q_{ul}}$) than the duration of the laser pulse (τ_{pulse}), steady-state can be assumed among the population densities [23, 40]. Thus, the rate of change in the population density n_i is nil ($\frac{dn_i}{dt} = 0$), and using Eq. (1–2) and Eq. (5), it leads to:

$$n_2 = n_T^\circ \cdot \frac{\left[\frac{R_{31} + V_{31}}{W_{12} + R_{13} + V_{13}} \right]}{\left[1 + \frac{R_{31} + V_{31}}{W_{12} + R_{13} + V_{13}} \right] \cdot \left[\frac{W_{21} + Q_{21} + A_{21} + Q_{23} + A_{23}}{W_{12}} \right] - \left[\frac{W_{21} + Q_{21} + A_{21} - (R_{31} + V_{31})}{W_{12} + R_{13} + V_{13}} \right]}. \quad (10)$$

Additionally, prior to laser excitation, the population density in state 2 is assumed negligible ($n_2^\circ \sim 0$), such that Eq. (1) transforms to:

$$n_1^\circ (R_{13} + V_{13}) = n_3^\circ (R_{31} + V_{31}), \quad (11)$$

where n_1° and n_3° are calculated using the Boltzmann fraction (f_B) such that $n_1^\circ = f_B \cdot n_T^\circ$, and $n_3^\circ = (1 - f_B) \cdot n_T^\circ$:

$$\frac{n_1^\circ}{n_3^\circ} = \frac{R_{31} + V_{31}}{R_{13} + V_{13}} = \frac{f_B}{1 - f_B}. \quad (12)$$

Assuming extremely fast RET and VET between state 1 and 3, consistent with the modelling software LIFSim [32], R_{13} , V_{13} , R_{31} , and V_{31} are outweighing the other terms in Eq. (10), such that:

$$n_2 = f_B \cdot n_T^\circ \cdot \frac{W_{12}}{f_B \cdot W_{12} + W_{21} + W_{\text{sat}}}, \quad (13)$$

where $W_{\text{sat}} = Q_{21} + A_{21} + Q_{23} + A_{23}$ represents the rate constant at which M^* gets de-excited, independently of the incident laser energy. Thus, the population density of state 2 is dependent on the rate of energy absorbed (W_{12}) by the target molecule at the initial laser-excitation state, and also on the rate at which the state is depleted to fill the other states.

Under the linear regime assumption, $W_{\text{sat}} \gg (f_B \cdot W_{12} + W_{21})$, simplifying Eq. (13) to:

$$n_2 = f_B \cdot n_T^\circ \cdot \frac{W_{12}}{W_{\text{sat}}}. \quad (14)$$

As seen in Fig. 2, the total fluorescence emitted, and possibly captured by the camera, results from the transitions from state 2 to state 1 (A_{21}) or to state 3 (A_{23}). For a 3-level LIF model, involving the steady-state assumption, the total LIF signal ($S_{M-\text{LIF}}$), per pulse, results from the following equation:

$$S_{M-\text{LIF}} = n_2 (A_{21} + A_{23}) \cdot \mathcal{E}_c \mathcal{T}_\lambda \frac{\Omega}{4\pi} \ell A \cdot \tau_{\text{pulse}}, \quad (15)$$

where three factors are distinguished: $n_2 (A_{21} + A_{23})$ is the rate of photon emission per unit volume [$\text{photon} \cdot \text{m}^{-3} \cdot \text{s}^{-1}$], $\mathcal{E}_c \mathcal{T}_\lambda \frac{\Omega}{4\pi} \ell A$ relates to the collection efficiency over the measurement volume [$\text{count} \cdot \text{photon}^{-1} \cdot \text{m}^3$], and τ_{pulse} is the laser pulse length [s] over which the camera integrates

the signal. \mathcal{E}_c is the quantum efficiency of the camera [count·photon⁻¹], \mathcal{T}_λ is the transmissivity of the optical system [-], Ω is the collection solid angle over which the fluorescence of M^* is captured by the detection system [sr], and ℓ is the length of the laser path through the measurement volume [m].

Thus, the total population density in the measurement volume prior to laser excitation (n_T°) can be recovered by measuring S_{M-LIF} [count] and re-arranging Eq. (14) and Eq. (15):

$$S_{M-LIF} = f_B \cdot n_T^\circ \cdot \frac{W_{12}(A_{21} + A_{23})}{W_{sat}} \cdot \mathcal{E}_c \mathcal{T}_\lambda \frac{\Omega}{4\pi} \ell A \cdot \tau_{pulse}. \quad (16)$$

The concentration is used to calculate the molar fraction of the molecule in the volume through the ideal gas law:

$$n_T^\circ = X_M \cdot \frac{p}{T \cdot \mathcal{R}_u} \cdot \mathcal{N}_A, \quad (17)$$

where n_T° is the total number density of M [m⁻³], X_M is the molar fraction of M [-], p is the pressure [Pa], T is the temperature [K] in the measurement volume, \mathcal{R}_u is the universal gas constant [J·mol⁻¹·K⁻¹], and \mathcal{N}_A is Avogadro's number [mol⁻¹].

2.1.3. Obtaining NO concentration from a 3-level linear steady-state LIF signal

For this study, NO concentration measurements are obtained by conducting NO-LIF in the linear regime and assuming steady-state, thus Eq. (16) develops to:

$$S_{NO-LIF} = X_{NO} \cdot f_B \cdot \frac{p}{T \cdot \mathcal{R}_u} \cdot \mathcal{N}_A \cdot \frac{B_{12}}{c} \cdot \frac{I}{\Delta\nu_L} \cdot \Gamma \cdot \frac{\sum A_{ul}}{\sum Q_{ul} + \sum A_{ul}} \cdot \mathcal{E}_c \mathcal{T}_\lambda \frac{\Omega}{4\pi} \ell A \cdot \tau_{pulse}, \quad (18)$$

with $\sum A_{ul} = A_{21} + A_{23}$ and $\sum Q_{ul} = Q_{21} + Q_{23}$. Normalising S_{NO-LIF} by the laser energy (linear LIF regime), the total fluorescence emitted per pulse by excited NO and captured by the detection system resolves to:

$$F_{NO-LIF} = S_{NO-LIF}/E_L, \quad (19)$$

$$= X_{NO} \cdot f_B \cdot \frac{p}{T \cdot \mathcal{R}_u} \cdot \mathcal{N}_A \cdot \frac{B_{12}}{c} \cdot \frac{\Gamma}{\Delta\nu_L} \cdot \frac{\sum A_{ul}}{\sum Q_{ul} + \sum A_{ul}} \cdot \mathcal{E}_c \mathcal{T}_\lambda \frac{\Omega}{4\pi} \ell, \quad (20)$$

where F_{NO-LIF} has the unit of [count·J⁻¹] or [J⁻¹].

Ultimately, the total fluorescence measured by the detection system and normalised by the laser energy can be expressed as:

$$F_{NO-LIF} = X_{NO} \cdot f_{LIF}(\lambda, f_B, p, T, B_{12}, \Delta\nu_L, \Gamma, A_{ul}, Q_{ul}) \cdot C_{opt}(\mathcal{E}_c, \mathcal{T}_\lambda, \Omega, \ell), \quad (21)$$

where X_{NO} is the molar fraction of NO in the measurement volume, f_{LIF} is a factor encompassing all absorption and emission parameters, and C_{opt} is the optical calibration constant regrouping all optical parameters [count·photon⁻¹·m] or [m].

f_{LIF} can also be re-arranged according to the type of terms composing it:

$$f_{\text{LIF}} = \underbrace{\frac{pf_{\text{B}}}{T}}_{\text{flame-dependent}} \cdot \underbrace{\frac{1}{\sum Q_{ul}}}_{\text{constants}} \cdot \underbrace{\frac{\mathcal{N}_{\text{A}}}{c\mathcal{R}_{\text{u}}}}_{\text{laser-dependent}} \cdot \underbrace{\frac{1}{\Delta\nu_{\text{L}}}}_{\text{line-dependent}} \cdot \underbrace{B_{12} \sum A_{ul}}_{\text{flame-laser-dependent}} \cdot \underbrace{\Gamma}_{\text{flame-laser-dependent}}, \quad (22)$$

where $(\sum Q_{ul} + \sum A_{ul}) \sim \sum Q_{ul}$ as, generally, $\sum A_{ul} \ll \sum Q_{ul}$. Thus, for a setup that is kept untouched during an experimental campaign, only few parameters related to the flame condition impact $F_{\text{NO-LIF}}$.

In this study, for a given condition, X_{NO} is determined through the measurement of $F_{\text{NO-LIF}}$, and through the inference of $(f_{\text{LIF}} \cdot C_{\text{opt}})$ obtained *via* calibration. This forms the core of quantitative NO-LIF to which different techniques of calibration vary in the application of Eq. (21).

2.2. LIF calibration techniques and assumptions

In practical settings, LIF measurements must be performed by taking into consideration two experimental effects: background subtraction and reburn. Both of these effects are tackled in this work by employing different calibration techniques and assumptions, ultimately extending the applicability of LIF for quantitative NO measurement.

2.2.1. Background subtraction

In flames, the LIF fluorescence is the result of the excitation of, not only the NO molecules, but also other species present in the volume, typically O_2 , CO_2 , and H_2O . Thus, the captured fluorescence, $F_{\text{fluo.}}(\lambda)$, integrates the light emitted by NO-LIF ($F_{\text{NO-LIF}}(\lambda)$), the LIF interfering signal ($F_{\text{interf.-LIF}}(\lambda)$), and signal related to other light sources (F_{dark}), such as flame chemiluminescence, ambient light, and camera dark noise:

$$F_{\text{fluo.}}(\lambda) = F_{\text{NO-LIF}}(\lambda) + F_{\text{bckgd}}(\lambda), \quad (23)$$

$$= F_{\text{NO-LIF}}(\lambda) + F_{\text{interf.-LIF}}(\lambda) + F_{\text{dark}}. \quad (24)$$

To obtain the signal that is only dependent on NO excitation and, therefore, solely proportional to the NO concentration at the measurement location, the total fluorescence signal needs to be rid of any background signal ($F_{\text{bckgd}}(\lambda)$). While F_{dark} can easily be measured, $F_{\text{interf.-LIF}}(\lambda)$ usually needs to be inferred as its direct measurement is practically impossible.

Assumption of constant $F_{\text{interf.-LIF}}(\lambda)$ on the spectrum

Typically, $F_{\text{interf.-LIF}}(\lambda)$ is assumed constant for small changes in the excitation wavelength. This is generally valid at atmospheric conditions where NO lines can be easily isolated from O_2 -LIF or H_2O -LIF systems and where CO_2 -LIF is a broadband faint background signal [41]. Thus, $F_{\text{interf.-LIF}}(\lambda)$ can be deduced using the measured fluorescence signal of the flame at two excitation wavelengths. These are chosen to correspond to an on-resonance peak of NO absorption (λ_{on}), and an off-resonance wavelength (λ_{off}). The subtraction of the signal $F_{\text{fluo.}}(\lambda)$ obtained at both wavelengths leads to $F_{\text{NO-LIF}}$ free from $F_{\text{bckgd}}(\lambda)$, as it is assumed that $F_{\text{interf.-LIF}}(\lambda_{\text{on}}) = F_{\text{interf.-LIF}}(\lambda_{\text{off}})$:

$$F_{\text{NO-LIF}} = F_{\text{fluo.}}(\lambda_{\text{on}}) - F_{\text{fluo.}}(\lambda_{\text{off}}) = F_{\text{NO-LIF}}(\lambda_{\text{on}}) - F_{\text{NO-LIF}}(\lambda_{\text{off}}), \quad (25)$$

where $F_{\text{NO-LIF}}(\lambda_{\text{off}}) \sim 0$.

Assumption of non-constant $F_{\text{interf.-LIF}}(\lambda)$ on the spectrum

When constant interfering LIF cannot be assumed, an alternative solution was proposed by Versailles *et al.* [22, 42]. They developed a strategy to calculate $F_{\text{interf.-LIF}}(\lambda)$ at high pressure conditions using the signal of a seeded (subscript ‘nsct+sd’) and unseeded (subscript ‘nsct’) flames¹. By recognising that $F_{\text{interf.-LIF}}(\lambda)$ is the same in seeded and unseeded flames:

$$F_{\text{interf.-LIF}}(\lambda) = F_{\text{fluo.,nsct}}(\lambda) - F_{\text{dark}} - F_{\text{NO-LIF,nsct}}(\lambda), \text{ and} \quad (26)$$

$$= F_{\text{fluo.,nsct+sd}}(\lambda) - F_{\text{dark}} - F_{\text{NO-LIF,nsct+sd}}(\lambda), \quad (27)$$

where $F_{\text{NO-LIF,nsct}}(\lambda)$ and $F_{\text{NO-LIF,nsct+sd}}(\lambda)$ are *a priori* unknown, and defining $F_{\text{NO-LIF,sd}}(\lambda)$ as the difference of signal between seeded and unseeded flames, only proportional to the seeded concentration of NO:

$$F_{\text{NO-LIF,sd}}(\lambda) = F_{\text{NO-LIF,nsct+sd}}(\lambda) - F_{\text{NO-LIF,nsct}}(\lambda), \quad (28)$$

$$= F_{\text{fluo.,nsct+sd}}(\lambda) - F_{\text{fluo.,nsct}}(\lambda), \quad (29)$$

then, $F_{\text{interf.-LIF}}(\lambda)$ can be calculated:

$$F_{\text{interf.-LIF}}(\lambda) = F_{\text{fluo.,nsct+sd}}(\lambda) - F_{\text{dark}} - F_{\text{NO-LIF,sd}}(\lambda) \cdot C_{\text{bckgd}}, \quad (30)$$

where C_{bckgd} , the dimensionless background coefficient, is obtained by removing the NO spectral features from $F_{\text{interf.-LIF}}(\lambda)$ through a fitting procedure. Using this technique, $F_{\text{interf.-LIF}}(\lambda)$ is obtained assuming a spectrally non-constant interfering LIF signal, enabling the calculation of $F_{\text{NO-LIF}}$, free from $F_{\text{bckgd}}(\lambda)$:

$$F_{\text{NO-LIF}}(\lambda) = F_{\text{fluo.}}(\lambda) - F_{\text{dark}} - F_{\text{interf.-LIF}}(\lambda). \quad (31)$$

This method was used to obtain NO-LIF measurements at high pressure conditions [22, 42, 43].

2.2.2. Reburn

Both calibration techniques that are presented in the following section rely on seeding the flame with NO in order to obtain $(f_{\text{LIF}} \cdot C_{\text{opt}})$, or some terms of it, from Eq. (21). In this work, seeding is possible because NO is a stable molecule at ambient conditions. Despite its initially-stable state, NO can react through the flame, so called reburn, leading to a lower fluorescence signal than expected from what should be a constant concentration. This occurs when seeding is performed in large quantity [44], at rich and/or high pressure conditions, and in N-containing fuels such as NH_3 . Conditions for NO reburn are explored in Appendix C.1.

As such, two calibration techniques are presented in this work: the linear extrapolation from seeded to nascent NO concentrations that cannot be applied in case of non-negligible reburn, and the optical calibration using experimental and modelled LIF parameters that can be applied in conditions of reburn or when the molecule cannot be seeded (such as CH, NH, or OH).

¹These notations were defined to be representative of the source of NO in the flame, see nomenclature.

Assumption of negligible NO reburn

Under the assumption of negligible reburn, a calibration technique can be employed to avoid calculating $(f_{\text{LIF}} \cdot C_{\text{opt}})$ explicitly in order to obtain X_{NO} from $F_{\text{NO-LIF}}$ in Eq. (21).

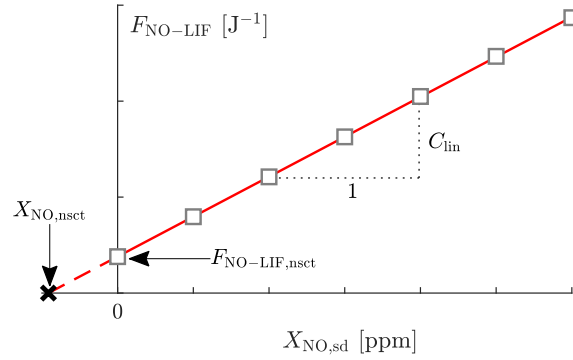


Figure 3: Illustration of the linear extrapolation from seeded to nascent NO concentrations calibration technique. The extrapolation of the measured $F_{\text{NO-LIF}}$ with the different levels of NO seeding leads to the determination of C_{lin} , valid for a given flame condition and axial location in the domain.

The calibration technique *via* the linear extrapolation involves the seeding of the measurement volume with one, or several, levels of NO concentration, as demonstrated in Fig. 3. This is possible by assuming that every term of Eq. (22) as well as C_{opt} , remain constant between the unseeded and seeded flames, at a given location, such that:

$$F_{\text{NO-LIF,nsct}} = X_{\text{NO,nsct}} \cdot f_{\text{LIF}} \cdot C_{\text{opt}}, \quad (32)$$

and,

$$F_{\text{NO-LIF,nsct+sd}} = X_{\text{NO,nsct+sd}} \cdot f_{\text{LIF}} \cdot C_{\text{opt}}, \quad (33)$$

where $X_{\text{NO,nsct}}$ is the nascent concentration of NO, *i.e.* the measurement of interest, and $X_{\text{NO,nsct+sd}}$ is the concentration of NO contained in flame after seeding, composed of the seeded NO in the initial mixture ($X_{\text{NO,sd}}$) and the nascent NO ($X_{\text{NO,nsct}}$). As such, the following applies:

$$F_{\text{NO-LIF,nsct}} = X_{\text{NO,nsct}} \cdot C_{\text{lin}}, \quad (34)$$

where C_{lin} is the linear coefficient between the LIF signal and the seeded NO level [$\text{J}^{-1} \cdot \text{ppm}^{-1}$]:

$$C_{\text{lin}} = f_{\text{LIF}} \cdot C_{\text{opt}} = \frac{F_{\text{NO-LIF,nsct+sd}} - F_{\text{NO-LIF,nsct}}}{X_{\text{NO,sd}}}, \quad (35)$$

and, ultimately, allows the calculation of $X_{\text{NO,nsct}}$.

If this technique was applied under NO reburn conditions, the actual $X_{\text{NO,sd}}$ would be lower than expected (see Fig. C.16 in Appendix), leading to a lower $F_{\text{NO-LIF,nsct+sd}}$ and C_{lin} . This would invalidate the linear extrapolation of $X_{\text{NO,nsct}}$.

This technique is valid in the three LIF regimes (linear, intermediate, saturated) and is one of the most commonly employed calibration techniques since it does not require any LIF modelling [16, 18, 20, 21, 45–48]. Nonetheless, care must be employed when performing such calculations as

it is valid only if the composition and condition (pressure and temperature) are assumed constant between the seeded and unseeded flames; thus, it is only applicable in flames that are temporally-stable and at a single given location of the flame. To apply the calibration to other conditions, corrections must be applied between the calibration flame and the measured flame, accounting for the difference in the temperature, the Boltzmann fraction, and the collisional quenching rate, as seen through the flame-dependent terms of Eq. (22), and described by Watson *et al.* [47], Sahu and Ravikrishna [48], and Brackmann *et al.* [21]. By employing such corrections, this technique is ultimately similar to the one presented next, where f_{LIF} is modelled and C_{opt} calibrated.

Assumption of non-negligible NO reburn

Under the assumption of non-negligible NO reburn, or in cases where seeding of the target molecule is not possible, a technique is used to model the terms of f_{LIF} in Eq. (22) and to calibrate C_{opt} as its terms are difficult to model and measure. With this calibration technique, the experimental LIF signal is compared to a modelled one such that:

$$F_{\text{NO-LIF}}^{\text{exp}} = X_{\text{NO}}^{\text{exp}} \cdot f_{\text{LIF}}^{\text{exp}} \cdot C_{\text{opt}}, \quad (36)$$

and,

$$F_{\text{NO-LIF}}^{\text{num}} = X_{\text{NO}}^{\text{num}} \cdot f_{\text{LIF}}^{\text{num}}, \quad (37)$$

where a distinction is made between the terms obtained numerically (superscript ‘num’) and experimentally (superscript ‘exp’). The determination of C_{opt} is done by fitting the experimental to the modelled LIF signal of a calibration flame with a known and finite concentration of seeded NO, under which assumptions of negligible NO reburn apply, such that:

$$F_{\text{NO-LIF,sd}}^{\text{num}} = \frac{F_{\text{NO-LIF,sd}}^{\text{exp}}}{C_{\text{opt}}}, \quad (38)$$

or,

$$C_{\text{opt}} = \frac{(F_{\text{NO-LIF,nsct+sd}} - F_{\text{NO-LIF,nsct}})^{\text{exp}}}{(F_{\text{NO-LIF,nsct+sd}} - F_{\text{NO-LIF,nsct}})^{\text{num}}} = \mathcal{E}_c \mathcal{T}_\lambda \frac{\Omega}{4\pi} \ell. \quad (39)$$

C_{opt} is independent of the calibration flame chosen as it only represents the experimental optical constants (see Appendix C.4). Once obtained, quantitative measurement of NO can be achieved by normalising the signal of the unseeded flame by C_{opt} , $F_{\text{NO-LIF,nsct}}/C_{\text{opt}}$, or by calculating $X_{\text{NO,nsct}}$ through the modelling of $f_{\text{LIF}}^{\text{exp}}$.

This calibration technique is, therefore, applicable to any other flame conditions, even if there is reburn of NO or if they are temporally-unstable, as long as the optical calibration coefficient is obtained in a flame without reburn, or in a flow that can be accurately modelled chemically. This considerably extends the applicability of LIF for quantitative NO measurements. It relies on the assumption that the parameters of $f_{\text{LIF}}^{\text{num}}$ are accurately captured by the numerical model in the calibration flame. This technique is also valid in the three LIF regimes as long as $f_{\text{LIF}}^{\text{num}}$ is modelled accordingly. While not always used under the same terminology, several studies use this exact technique [49–51], or a variant [21, 47, 48, 52].

The C_{opt} calibration technique is also applicable in conditions where the target molecule cannot be seeded. In this case, a surrogate molecule can be excited in place of the target molecule [53,

54], or the LIF measurement can be combined with another measurement technique, such as Rayleigh [33, 55–57] or Raman scattering [58, 59], to ultimately obtain C_{opt} . The Rayleigh and Raman calibration techniques rely on measuring the scattered signal of a stable molecule, such as N_2 , He, or H_2 , using the same experimental and optical setup than for the LIF signal measurement. The measured scattered signal is a function of the molecule cross-section and its number density, the laser parameters, and the calibration coefficient of the optical system (C_{opt}). Hence, C_{opt} can be obtained by modelling the other parameters and can then be integrated in the LIF model to obtain the absolute measurement of the short-lived species. An alternative consists of calculating the ratio of the LIF and scattering signals, leading to a fluorescence signal free of the optical calibration coefficient [33]. The measurement of the Rayleigh or Raman scattering signals can, however, lead to experimental difficulties, specifically in handling laser reflections [25].

These techniques are important for the quantitative measurement of short-lived species, though they are less commonly employed. The specifics of these techniques are beyond the scope of this work, but can readily be applied from the general principles outlined in this study.

2.2.3. Scope of the study

This work specifically focuses on the two pairs of calibration techniques and background subtraction methods aforementioned as, combined, they represent the largest span of applicability for quantitative NO measurements. Therefore, this study aims to compare four techniques by presenting their experimental strategies, mathematics, and uncertainties: the extrapolation of seeded to nascent NO concentrations assuming constant and non-constant interfering LIF, and the optical calibration using experimental and modelled LIF parameters assuming constant and non-constant interfering LIF.

3. Experimental setup and methods

The comparison of the NO quantification techniques is conducted by collecting the LIF signal of several flames at varying experimental conditions, and processed using different methodologies to obtain the measurement of NO produced by the flames. This work presents measurements from flames obtained in a stagnation flame burner, however, LIF diagnostics are applicable to a variety of different flame setups thanks to its non-intrusive *in situ* nature, such as in porous burners [16, 18, 46], Bunsen burners [59], diffusion and premixed counter-flow burners [20, 34, 48, 60], shock tubes [61], jet flames [62], and Direct-Injection engines [45].

3.1. Stagnation flame burner

Premixed, laminar, quasi-1D, methane-air flames are produced using a water-cooled stagnation plate burner, as depicted by Fig. 4a. It is placed inside a high-pressure enclosure with four windows for optical diagnostics. It is designed for gas turbine operating pressures, and has been used up to 16 atm [22, 42]. The fuel/oxidiser blend flows through a mixing tank to ensure homogeneity of the mixture. A co-flowing stream of inert gas is used to shield the flame from the surrounding gas. The flat, lifted, stagnation flame is stabilised between the nozzle and the plate, separated by a distance of ~ 9.5 mm. The stagnation plate is maintained at a constant temperature during the experiments using cooling water.

In this study, three flames are produced, covering a variety of conditions described in Tab. 1. They have been chosen to demonstrate the applicability of the calibration techniques at varying

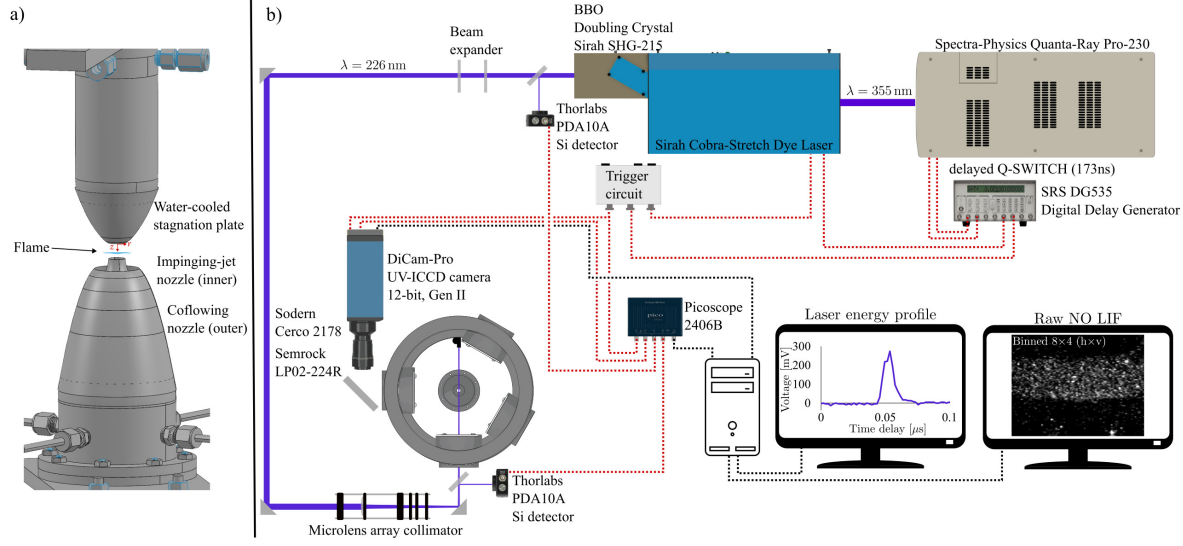


Figure 4: Side view of the stagnation flame burner (a), top view of the laser and detection system setup for NO-LIF diagnostic (b).

equivalence ratios and through a wide range of adiabatic flame temperatures. To reach a high adiabatic flame temperature ($\Phi_{0.9_Tad2500K_O40}$), oxygen-enriched air is used in combination with argon dilution in the oxidiser stream for improved flame stability. To perform NO-LIF calibration, each flame is also seeded with NO at several concentrations. The notation presented in Tab. 1 is defined as:

$$X_{O_2} = \frac{\dot{N}_{O_2}}{\dot{N}_{O_2} + \dot{N}_{N_2}}, \quad (40)$$

$$X_{Ar} = \frac{\dot{N}_{Ar}}{\dot{N}_{O_2} + \dot{N}_{N_2} + \dot{N}_{Ar}}, \quad (41)$$

$$X_{NO,sd} = \frac{\dot{N}_{NO,sd}}{\dot{N}_{total}} = \frac{\dot{N}_{NO,sd}}{\dot{N}_{CH_4} + \dot{N}_{O_2} + \dot{N}_{N_2} + \dot{N}_{Ar} + \dot{N}_{NO,sd}}, \quad (42)$$

where \dot{N}_s is the molar flow rate of species s [$\text{mol}\cdot\text{s}^{-1}$], X_{O_2} is the oxygen molar fraction of the oxidiser mixture, X_{Ar} is the argon dilution in the diluted-oxidising mixture, and $X_{NO,sd}$ is the NO mole fraction of seeded NO in the premixed flow.

The different gas flow rates are controlled using a series of thermal Mass Flow Controllers (MFCs, Bronkhorst EI-Select). They are calibrated before the measurement campaign using their respective gas with a dry-piston calibrator (DryCal ML-500), yielding an uncertainty of $\pm 0.4\%$ on the flow rate of each MFC. NO is seeded in the mixture from gas cylinders containing $247 \text{ ppm} \pm 2\%$ of NO in N_2 for the undiluted flames, and $2965 \text{ ppm} \pm 2\%$ of NO in Ar for the Ar-diluted flames. The NO gas mixture is further diluted to the desired seeding concentration using additional bath gas. In the case of non-diluted flames ($\Phi_{0.9_Tad2130K_O21}$ and $\Phi_{0.7_Tad1830K_O21}$), enriched oxygen is used to compensate for the extra dilution of N_2 due to the seeding of NO, ensuring a final 3.76:1 ratio of N_2 to O_2 in the oxidiser stream.

Boundary conditions needed to perform simulations are acquired during the experiments with

Table 1: Flame conditions used in this study.

Flame nomenclature	Fuel species	ϕ [-]	T_{ad} [K]	p [atm]	X_{O_2} [-]	X_{Ar} [-]	$X_{NO,sd}$ [ppm]	Experimental samples	
								Constant	Non-constant
								$F_{interf.-LIF}$	$F_{interf.-LIF}$
Phi0.9_Tad2130K_O21	CH ₄	0.9	2130	1	0.21	0.0000	0	6	4
							25	3	2
							50	4	2
							75	5	2
Phi0.7_Tad1830K_O21	CH ₄	0.7	1830	1	0.21	0.0000	0	2	-
							50	2	-
Phi0.9_Tad2500K_O40	CH ₄	0.9	2500	1	0.40	0.3085	0	2	-
							150	2	-

Particle Tracking Velocimetry (PTV) [33, 40, 63, 64]. Type-K thermocouples are used to measure the inlet temperature of the mixture (T_{in}) and the stagnation plate temperature (T_{wall}) within ± 2 K and ± 5 K, respectively. The length of the domain used for the simulations (\mathcal{L}) is determined at the location of minimum uncertainty of the velocity, in the unburnt region, which is where the inlet velocity (u_{in}) and the axial strain rate (du_{in}/dz) are extracted. The boundary conditions for each flame and their respective uncertainties are presented in Appendix A.

3.2. Laser and detection system

Figure 4b presents the hardware setup to obtain NO-LIF data. Light is emitted by a pulsed Nd:YAG laser (Spectra-Physics Quanta-Ray Pro-230) using the third harmonic at 355 nm. Short and energetic pulses are achieved by delaying the Q-switch by 173 ns using a delay generator (SRS DG535). The laser beam passes through a wavelength-tunable dye laser (Sirah Cobra-Stretch) containing a Coumarin 450/methanol dye solution, and through a frequency-doubling crystal (Sirah BBO SGH-215). The resulting laser beam can be tuned to a wavelength of ~ 226 nm with a pulse duration of ~ 10.5 ns at a repetition rate of 10 Hz. A series of lenses shape the beam into a thin sheet (~ 9 mm tall and ~ 1 mm wide) focused above the centre of the burner. A micro-lens array system is also used to ensure beam homogeneity [65]. The laser beam is used to excite the A–X (0, 0) electronic system of NO at different wavelengths around 226 nm (see theoretical excitation spectrum in Fig. 5). This spectral region was chosen, following the recommendation of DiRosa [66] and Bessler *et al.* [41, 67], to minimise the impact of interfering LIF signal and to maintain a strong LIF signal with an increasing temperature of the mixture.

The wavelength of the laser is monitored several times per day to ensure that the laser beam is produced at the desired wavelength. This is done by comparing a theoretical excitation spectrum to one obtained experimentally. The experimental spectrum is obtained by varying the wavelength of the dye laser from ~ 226.00 nm to ~ 226.06 nm and capturing the LIF signal of a cold flow of constant NO concentration. The resulting comparison is presented in Fig. 5.

This routine procedure also permits to obtain the laser beam profile, often not perfectly homogeneous when resulting from a dye laser, to correct the signal for any spatial fluctuation. An example of such inhomogeneity is depicted later in this paper (see Fig. 6).

The emitted fluorescence from excited NO molecules is captured by a UV-Intensified CCD camera (DiCam-Pro 12-bit, Gen II). The ICCD camera records the LIF signal at 90° from the laser sheet. It is equipped with extension tubes and an UV achromatic lens (Sodern Cerco 2178),

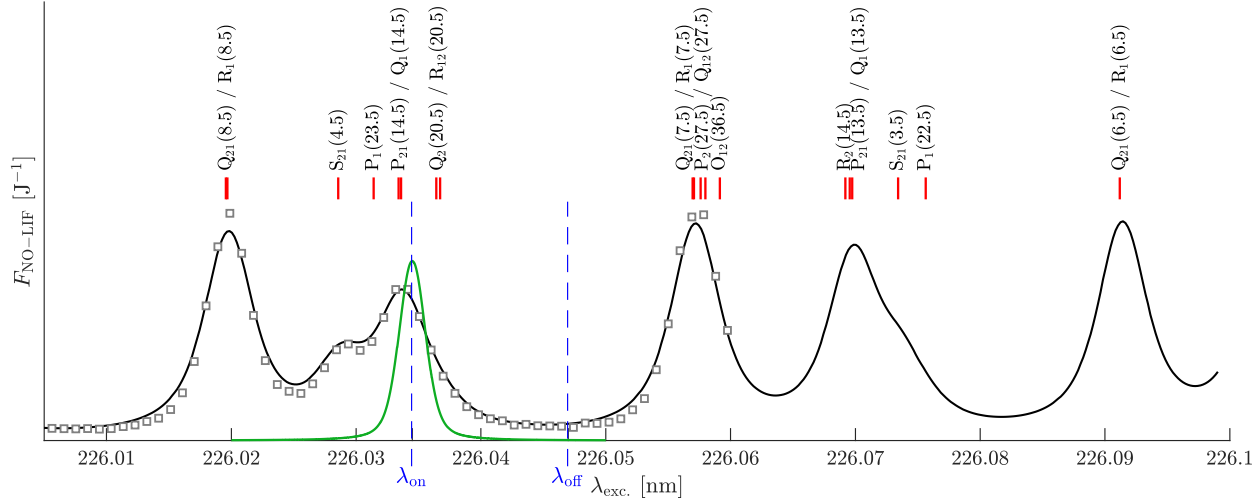


Figure 5: NO excitation spectrum obtained experimentally (squares) and with LIFSim (black curve) at a temperature of 300 K. The NO transition lines positions and labels are also specified. The nomenclature of each NO transition is specific to the quantum features of the transition. The position of the online (λ_{on}) and offline (λ_{off}) excitation wavelengths, used experimentally, is also shown (blue dashed lines). The laser lineshape, inferred experimentally, is displayed *via* the green curve, centred around λ_{on} .

yielding a resolution of $26.3 \pm 0.1 \mu\text{m}/\text{pix}$. The camera is also equipped with a 235 nm long-pass filter to remove Rayleigh scattering and reflections. The image is binned 4×8 (vertically and horizontally, respectively) to enhance the signal-to-noise ratio. Finally, a gating of 300 ns is used to capture the entirety of the fluorescence emitted and reduce the contribution from the flame chemiluminescence.

Two photo-diodes (Thorlabs PDA10A), each coupled to a 90:10 beamsplitter, monitor the laser energy and pulse duration along the optical path and allow the assessment of the shot-to-shot change in laser energy used for the normalisation of the experimental LIF signal. As it is impossible to measure the absolute laser energy at the location of the flame, a measurement of the laser energy is obtained ~ 30 cm upstream of the flame and is assumed proportional to the energy irradiating the NO molecules. An absolute measurement of the laser energy prior to each measurement is performed at the exit of the dye laser (~ 300 cm upstream of the flame) and leads to ~ 0.7 mJ/pulse spread on an unfocused sheet of ~ 1 mm width by ~ 9 mm height. Additionally, linearity was verified by comparing experimentally-obtained spectra with theoretical linear spectra obtained from LIFSim [32], as seen in Fig. 5. It was also confirmed that the response of the signal for a given concentration of NO in a cold flow is linear with a change in the laser energy. The camera and photo-diodes are triggered synchronously with the dye laser gating with each signal collected using a 1 GHz sampling rate oscilloscope (Picoscope 2406B).

The acquired data results in a set of 2D fluorescence images ($S_{\text{flu.o.}}(\lambda)$) with their associated shot-to-shot laser energy ($E_L(\lambda)$). The signal of each image is averaged along the centre-line of the burner and is normalised by the average laser energy leading to a signal, $F_{\text{flu.o.}}(\lambda)$, composed of $F_{\text{NO-LIF}}(\lambda)$, $F_{\text{interf.-LIF}}(\lambda)$, and F_{dark} , as seen in Eq. (24).

For each calibration technique presented, strategies must be employed to: 1) rid the signal $F_{\text{flu.o.}}(\lambda)$ from any background signal $F_{\text{bckgd}}(\lambda)$ to obtain $F_{\text{NO-LIF}}(\lambda)$; and 2) relate $F_{\text{NO-LIF}}(\lambda)$ to the concentration or molar fraction of NO to solve Eq. (21).

4. NO-LIF calibration techniques

This section presents four techniques to transform $F_{\text{fluo.}}(\lambda)$ into quantitative NO measurements. Two calibration methodologies are employed: the linear extrapolation from seeded to nascent NO concentration (C_{lin}) and the optical calibration using experimental and modelled LIF parameters (C_{opt}). Both techniques are used under two background subtraction methods, assuming spectrally constant and non-constant interfering LIF signal. They differ in the way that $F_{\text{NO-LIF}}(\lambda)$ is calculated. The four techniques are presented and compared using the sample data obtained as described in the previous section.

4.1. Calculation of $F_{\text{NO-LIF}}(\lambda)$ using $F_{\text{fluo.}}(\lambda)$

The experimental methodology to measure $F_{\text{fluo.}}(\lambda)$ differs according to the assumption formulated about $F_{\text{interf.-LIF}}(\lambda)$. This leads to a different calculation of $F_{\text{NO-LIF}}(\lambda)$.

4.1.1. Assumption of constant $F_{\text{interf.-LIF}}(\lambda)$ on the spectrum

As presented in Section 2.2.1, the interfering LIF signal can be assumed constant under low pressure conditions, up to 4 atm [22]. In such conditions, the contribution of $F_{\text{interf.-LIF}}(\lambda)$ can be removed from $F_{\text{fluo.}}(\lambda)$ by subtracting the signal of an off-resonance absorption from an on-resonance absorption signal, as recalled from Eq. (25).

The axially-resolved signal produced within the measurement volume ($F_{\text{fluo.}}(\lambda)$) is obtained by averaging the LIF signal of 5,000 images at two wavelengths, indicated in Fig. 5. An online signal ($S_{\text{fluo.,on}}$) is captured at a wavelength $\lambda_{\text{on}} = 226.0345$ nm corresponding to a peak in absorption of the NO molecules comprising the $P_1(23.5)$, $Q_1+P_{21}(14.5)$, and $Q_2+P_{12}(20.5)$ lines. Additionally, an offline signal ($S_{\text{fluo.,off}}$) is captured at a wavelength $\lambda_{\text{off}} = 226.0470$ nm corresponding to a minimum in absorption. The signal of the flame without laser illumination (S_{dark}) is also captured (1,000 images) to obtain the flame chemiluminescence, ambient light, and camera dark noise signals. Finally, the laser beam profile is obtained (S_{BP}) in a cold flow of NO (1,600 images) and is used to correct the signal for spatial inhomogeneity in the laser sheet.

The background signal is subtracted from the online and offline signals, and these are normalised by their corresponding laser energies ($E_{\text{L,on}}$ and $E_{\text{L,off}}$). The offline fluorescence is used to remove the contribution from any interfering LIF signals from the online fluorescence. The subtraction of the two signals is normalised by the laser beam profile (S_{BP} , normalised such that $\int S_{\text{BP}} dz = 1$), and results in a signal ($F_{\text{NO-LIF}}$) that is only proportional to the NO concentration in the measurement volume. These operations are conducted as follows:

$$F_{\text{NO-LIF}} = (F_{\text{fluo.}}(\lambda_{\text{on}}) - F_{\text{dark}}) - (F_{\text{fluo.}}(\lambda_{\text{off}}) - F_{\text{dark}}), \quad (43)$$

$$= \left[\frac{(S_{\text{fluo.,on}} - S_{\text{dark}})}{E_{\text{L,on}}} - \frac{(S_{\text{fluo.,off}} - S_{\text{dark}})}{E_{\text{L,off}}} \right] \cdot \frac{1}{S_{\text{BP}}}. \quad (44)$$

Each step of the LIF processing is presented in Fig. 6. A sample image is presented on the left-hand side of the figure, along with its extracted signal profile on the right-hand side. Each profile is extracted at the centre line of the nozzle (r_0) and averaged radially from $r_0 - \Delta r$ to $r_0 + \Delta r$, representing a band of ~ 4.2 mm. Figure 6a presents the laser beam profile in a cold flow of NO. In the profile, the laser inhomogeneity can clearly be distinguished. Despite the use of a micro-lens array [65], fluctuations in the laser energy occur throughout the domain. Slight laser

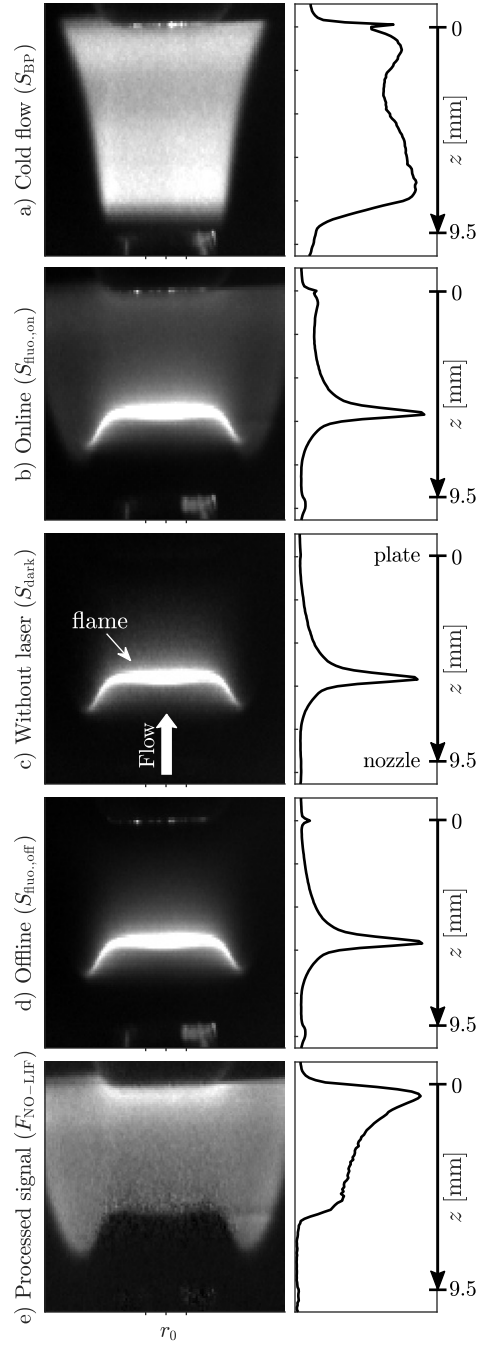


Figure 6: LIF signal obtained at several steps of the experimental process: a) in a cold flow of NO; and b-e) in the unseeded Phi0.9_Tad2130K_O21 flame.

reflections on the stagnation plate ($z = 0$ mm) and on the nozzle ($z = 9.5$ mm) can also be seen in the image and on the profile. Figure 6b presents the LIF signal obtained at the online wavelength in an unseeded flame. The signal is nil in the cold unburnt region of the flow as the flow is not seeded with NO, and naturally, does not produce NO. In the flame front, the signal is stronger due to flame chemiluminescence. This leads to background in the signal that needs to be accounted for. The signal in the post-flame region is mostly produced by the NO naturally formed by the flame. The

signal seems to decrease in the post-flame region, opposite to what is expected from the formation of NO in the post-flame region through the thermal-NO pathway. This artificial effect is due to the laser spatial inhomogeneity and background signal discussed previously, and hence, requires the signal to be corrected for it. Figure 6c depicts the image obtained without laser illumination to obtain the dark signal, encompassing the flame chemiluminescence, camera dark noise, and ambient light. This signal is later removed from the online and offline profiles. Figure 6d shows the image obtained at the offline wavelength. Despite production of NO in the post-flame region, the signal cannot be clearly distinguished because the offline excitation wavelength represents a minimal absorption of the NO molecules, as seen in Fig. 5. The flame chemiluminescence, and the laser reflections on the plate and nozzle can still be seen in the image and profile. Finally, Fig. 6e presents the processed signal following the methodology described below and in Eq. 44. The resulting signal is rid of laser inhomogeneity, flame chemiluminescence, camera dark noise, reflections, and ambient light. The signal sharply increases through the flame front, followed by a slower increase through the post-flame region. The increase of the signal near the plate is due to the thermal boundary layer of the cold plate, increasing the LIF signal despite no production of NO in this region.

4.1.2. Assumption of non-constant $F_{\text{interf.-LIF}}(\lambda)$ on the spectrum

In conditions where the interfering LIF signal cannot be assumed constant, as discussed in Section 2.2.1, another experimental methodology needs to be employed to infer $F_{\text{interf.-LIF}}(\lambda)$ without its direct measurement. In such conditions, $F_{\text{interf.-LIF}}(\lambda)$ is determined by measuring the signal of a seeded and an unseeded flame at varying excitation wavelengths.

The signal produced within the measurement volume ($F_{\text{flu.}}(\lambda)$) is calculated using the average of the captured signals of 120 laser pulses at 80 different excitation wavelengths from ~ 226.006 nm to ~ 226.116 nm, in steps of 1.4 pm. The resulting signal is axially- and spectrally-resolved. Similar to the previous experimental technique, S_{dark} and S_{BP} are captured to rid the signal of flame chemiluminescence, camera dark noise, ambient light, and the laser sheet spatial inhomogeneity, as per the subsequent equations:

$$F_{\text{NO-LIF}}(\lambda) = (F_{\text{flu.}}(\lambda) - F_{\text{dark}}) - F_{\text{interf.-LIF}}(\lambda), \quad (45)$$

$$= \left[\frac{(S_{\text{flu.}}(\lambda) - S_{\text{dark}})}{E_L(\lambda)} \right] \cdot \frac{1}{S_{\text{BP}}} - F_{\text{interf.-LIF}}(\lambda). \quad (46)$$

Following Eq. (46), $F_{\text{interf.-LIF}}(\lambda)$ needs to be inferred in order to obtain $F_{\text{NO-LIF}}(\lambda)$.

The measurements are carried out in a seeded and unseeded flame, and examples of images captured during the process are shown in Fig. 7. Selected images of the excitation spectrum in a flame seeded with 50 ppm of NO are displayed on the top row of Fig. 7. They represent either an on-resonance (Fig. 7a, b, and d), or an off-resonance excitation (Fig. 7c and e). The associated excitation spectrum, $S_{\text{flu.},\text{nsc}+\text{sd}}(\lambda)$ extracted at $z = 3$ mm, is plotted in red in the middle of the figure. Similarly, images captured in the unseeded flame are displayed on the bottom row of the figure. Its associated excitation spectrum, $S_{\text{flu.},\text{nsc}}(\lambda)$ also extracted at $z = 3$ mm, is plotted in blue in the middle of the figure. The wavelengths at which the images were extracted are indicated by the dashed lines. The brightness of the images was kept constant with wavelength for qualitative comparison. Naturally, the signal is stronger in the cold seeded region of the flame on an on-resonance wavelength due to the increased number density and the reduced quenching rate. For a

given wavelength, on or off-resonance, the signal is also stronger in the seeded flame than it is in the unseeded flame due to the increased concentration of NO. The signal remains to be corrected for the background signal (especially flame chemiluminescence) and the laser inhomogeneity, as described in Eq. (46).

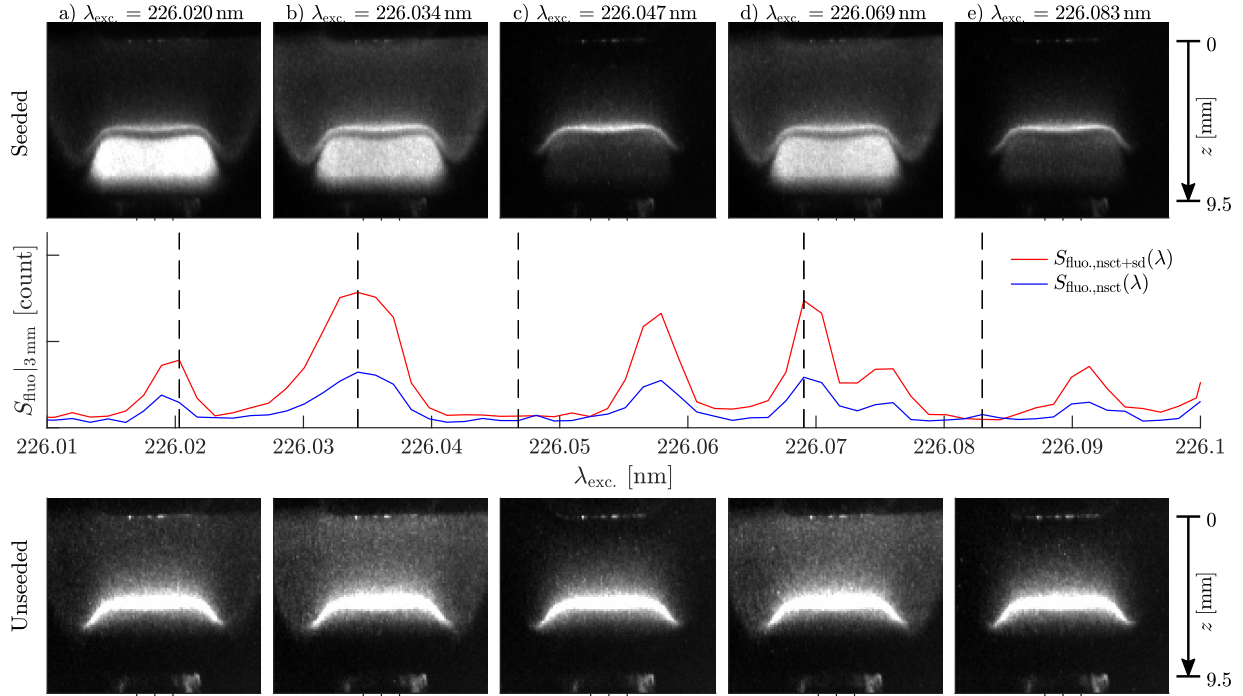


Figure 7: LIF signal obtained at several excitation wavelengths during the experimental process in the seeded (top) and unseeded (bottom) Phi0.9_Tad2130K_O21 flame. The fluorescence signal ($S_{\text{fluo.}}(\lambda)$), extracted at $z = 3$ mm, is plotted for both flames in the centre of the figure. The dashed lines represent the excitation wavelength at which each image was extracted. Note that the brightness of the images from the unseeded flame are enhanced compared to those from the seeded flame.

The interfering LIF signal is determined by eliminating any contribution from the NO lines on a seeded NO-LIF spectrum. Following the previous logic described in Eq. (24), the fluorescence signal of the flame is rid of its dark signal, such that for a seeded flame, the following equation is obtained:

$$F_{\text{fluo.,nsct+sd}}(\lambda) - F_{\text{dark}} = F_{\text{NO-LIF,nsct+sd}}(\lambda) + F_{\text{interf.-LIF}}(\lambda), \quad (47)$$

and by defining:

$$F_{\text{NO-LIF,sd}}(\lambda) = F_{\text{NO-LIF,nsct+sd}}(\lambda) - F_{\text{NO-LIF,nsct}}(\lambda), \quad (48)$$

the following relationships apply:

$$F_{\text{fluo.,nsct+sd}}(\lambda) - F_{\text{dark}} = F_{\text{NO-LIF,sd}}(\lambda) + F_{\text{NO-LIF,nsct}}(\lambda) + F_{\text{interf.-LIF}}(\lambda), \quad (49)$$

$$= F_{\text{NO-LIF,sd}}(\lambda) \cdot \left[1 + \frac{F_{\text{NO-LIF,nsct}}(\lambda)}{F_{\text{NO-LIF,sd}}(\lambda)} \right] + F_{\text{interf.-LIF}}(\lambda), \quad (50)$$

$$= F_{\text{NO-LIF,sd}}(\lambda) \cdot C_{\text{bckgd}} + F_{\text{interf.-LIF}}(\lambda), \quad (51)$$

where C_{bckgd} represents a scaling coefficient between the interfering LIF signal and the signal of a

known concentration of NO, necessary for the calculation of the total seeded fluorescence signal, with:

$$C_{\text{bckgd}} = 1 + \frac{F_{\text{NO-LIF,nsct}}(\lambda)}{F_{\text{NO-LIF,sd}}(\lambda)}. \quad (52)$$

The coefficient is not wavelength-dependent due to the division of the two wavelength-dependent signals, that spectrally scale uniformly with NO concentration.

To obtain C_{bckgd} , Eq. (52) cannot be used as $F_{\text{NO-LIF,nsct}}(\lambda)$ is unknown without the prior knowledge of $F_{\text{interf.-LIF}}(\lambda)$. Instead, C_{bckgd} is obtained through Eq. (51) by fitting $F_{\text{interf.-LIF}}(\lambda)$ on measured profiles as follows:

$$F_{\text{interf.-LIF}}(\lambda) = (F_{\text{fluo.,nsct+sd}}(\lambda) - F_{\text{dark}}) - F_{\text{NO-LIF,sd}}(\lambda) \cdot C_{\text{bckgd}}, \quad (53)$$

where $F_{\text{NO-LIF,sd}}(\lambda)$ is obtained by subtracting the signal of an unseeded flame from a seeded flame. This applies if the NO seeding is assumed to not change the concentration of interfering species and therefore remains constant for a given wavelength (see Appendix C.2). The determination of C_{bckgd} is performed by iterative least-squares minimisation of the difference between the calculated $F_{\text{interf.-LIF}}(\lambda)$ and a filtered (smoothed) version of itself, using Eq. (53) to remove any NO spectral features from $F_{\text{interf.-LIF}}(\lambda)$. The filtering of $F_{\text{interf.-LIF}}(\lambda)$ removes the effect of experimental noise.

This process is demonstrated in Fig. 8 for a given axial location of a flame. In Fig. 8a, each term of Eq. (53) is presented, including the final calculated interfering LIF spectrum, obtained after the iteration process of C_{bckgd} . Figure 8b-d presents the iteration process of C_{bckgd} , where $F_{\text{interf.-LIF}}(\lambda)$ is plotted with its smoothed counterpart for different values of C_{bckgd} .

The iteration of C_{bckgd} is performed to obtain $F_{\text{interf.-LIF}}(\lambda)$ under three constraints:

1. $F_{\text{interf.-LIF}}(\lambda)$ must not contain NO features;
2. $F_{\text{interf.-LIF}}(\lambda)|_{\text{smoothed}}$ must be non-negative, as a negative signal is non-physical; and
3. C_{bckgd} must minimise the least-square difference between $F_{\text{interf.-LIF}}(\lambda)$ and $F_{\text{interf.-LIF}}(\lambda)|_{\text{smoothed}}$.

In the event that C_{bckgd} is too small (Fig. 8b), $F_{\text{interf.-LIF}}(\lambda)$ still displays contributions of the NO-lines captured in the peaks of the grey curve aligning with the peaks present in the red, blue, and black curves of Fig. 8a. In the event that C_{bckgd} is too large (Fig. 8c), $F_{\text{interf.-LIF}}(\lambda)|_{\text{smoothed}}$ becomes negative and is, thus, a non-physical solution showing negative NO-LIF features. The appropriately fitted $F_{\text{interf.-LIF}}(\lambda)$ is displayed in Fig. 8d where negative values in the grey curve are limited to experimental noise, and where NO features cannot be clearly distinguished.

As the sample data was collected at atmospheric conditions, Fig. 8a validates the assumption of a nearly constant interfering LIF signal between the online (λ_{on}) and offline (λ_{off}) wavelengths. Hence, the previous experimental methodology assuming constant interfering LIF signal is demonstrated valid in these conditions, as per [22].

It is important to note that C_{bckgd} can be determined in flames with significant reburn, as long as the flame can be seeded and that the NO-LIF features of $F_{\text{fluo.,nsct+sd}}(\lambda)$ and $F_{\text{fluo.,nsct}}(\lambda)$ can be distinguished from the interfering LIF profile.

Finally, C_{bckgd} is computed for each axial location, and the profile is approximated by a sextic Bézier curve to reduce noise [42]. Once $F_{\text{interf.-LIF}}(\lambda)$ is obtained, $F_{\text{NO-LIF}}(\lambda)$ is calculated following Eq. (46) for a given wavelength. For the remaining of this work, the $F_{\text{NO-LIF}}$ profile is calculated using the signal at λ_{on} as it possesses the best signal-to-noise ratio, as well as the least temperature dependency.

4.1.3. Comparison of $F_{\text{NO-LIF}}$ profiles considering both assumptions on $F_{\text{interf.-LIF}}(\lambda)$

The calculated $F_{\text{NO-LIF}}$ profiles are compared for the Phi0.9_Tad2130K_O21 flames in Fig. 9. Only the unseeded and one seeding level ($X_{\text{NO,sd}} = 50$ ppm) are displayed for clarity. They are presented with their respective uncertainty quantification through the error-bar at $z = 3$ mm. Profiles are normalised by the optical calibration coefficient (C_{opt}) for a quantitative comparison as they have been measured using a different experimental configuration. The methodology to do so is presented in Section 4.2.2.

Profiles obtained using constant and non-constant $F_{\text{interf.-LIF}}(\lambda)$ assumptions show a perfect agreement for each level of seeding along the entire domain. Discrepancies can be observed in the region near the plate ($z \sim 0 - 1$ mm) due to larger scatter and a smaller data set for the technique assuming non-constant $F_{\text{interf.-LIF}}(\lambda)$, but is, usually, not the region of interest in the measurement of NO. These results demonstrate the effectiveness of both assumptions in the calculation of $F_{\text{NO-LIF}}$, as expected for atmospheric conditions.

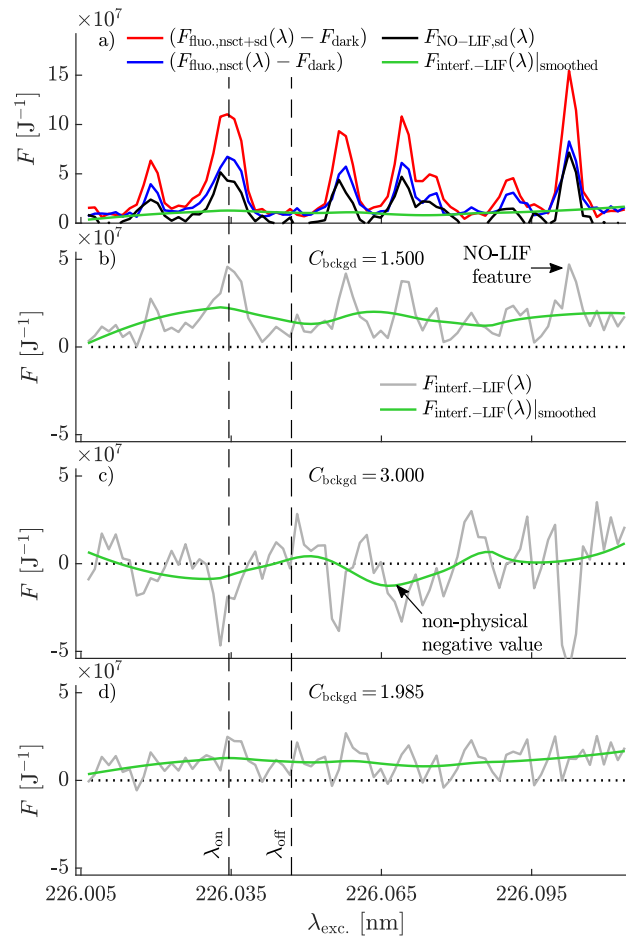


Figure 8: Determination process of C_{bckgd} via iteration, at a given position of the post-flame region of the Phi0.9_Tad2130K_O21 flame ($p = 1$ atm): a) signals composing the terms of Eq. (53); b-d) inference of $F_{\text{interf.-LIF}}(\lambda)$ using different values of C_{bckgd} (b - too small, c - too large, d - optimal).

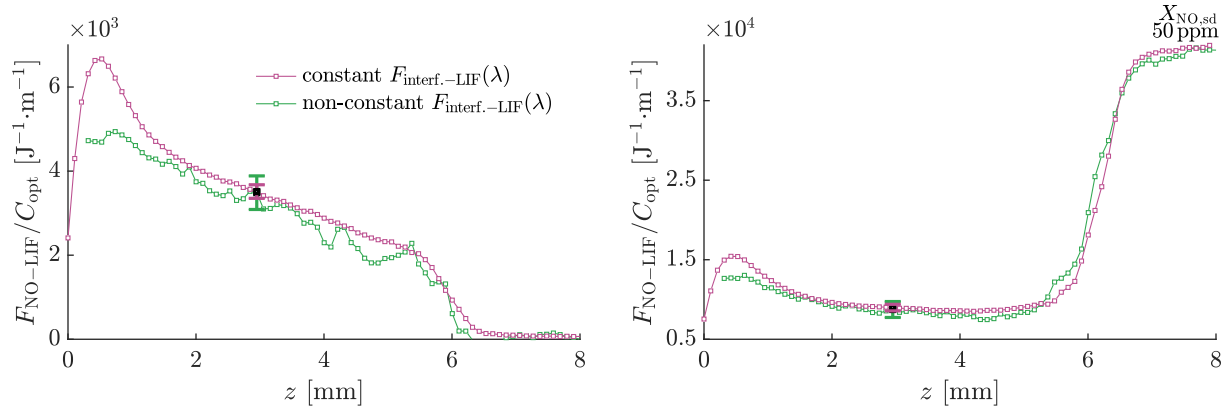


Figure 9: Comparison of the $F_{\text{NO-LIF}}/C_{\text{opt}}$ profiles of the unseeded (left) and seeded (right) Phi0.9_Tad2130K_O21 flames using the assumptions of constant (purple) and non-constant (green) $F_{\text{interf.-LIF}}(\lambda)$. Note the different scales of the vertical axis between both figures.

4.2. Calculation of $X_{\text{NO,nsct}}$ using $F_{\text{NO-LIF}}(\lambda)$

Once $F_{\text{NO-LIF}}(\lambda)$ is rid of $F_{\text{bckgd}}(\lambda)$, it can be used to calculate the amount of NO in the volume, as per Eq. (21). The application of this equation differs according to the assumption of NO re-burn that is formulated. This translates into a different post-processing of the experimental results through two distinct calibration techniques.

4.2.1. C_{lin} : Linear extrapolation from seeded to nascent NO concentrations - Assumption of negligible NO reburn

This calibration technique relies on the determination of a coefficient, C_{lin} , representing the linear proportionality of a signal for a given molar fraction of NO. As discussed in Section 2.2.2, C_{lin} replaces $(f_{\text{LIF}} \cdot C_{\text{opt}})$ in Eq. (21), and is found by assuming that:

1. there is negligible reburn of the NO molecules through the flame front (see Appendix C.1);
2. the temperature and species composition (except NO molar fraction) is identical in the unseeded and seeded flames (see Appendix C.2); and
3. the LIF signal scales linearly with NO concentration (see Fig. 10b).

To obtain C_{lin} , the signal of several flames, unseeded and seeded, are needed to calculate the proportionality of the captured fluorescence signal with NO molar fraction. The NO molar fraction produced by the unseeded flame can later be inferred from the proportionality coefficient, such that:

$$X_{\text{NO,nsct}} = \frac{F_{\text{NO-LIF,nsct}}}{C_{\text{lin}}}, \quad (54)$$

where C_{lin} represents the slope of a linear fit between $F_{\text{NO-LIF}}$ (seeded and unseeded) and $X_{\text{NO,sd}}$, and $F_{\text{NO-LIF,nsct}}$ is the intercept of the fit at $X_{\text{NO,sd}} = 0$. Thus, the accuracy of $X_{\text{NO,nsct}}$ results from the confidence interval of the fit² (see Appendix D).

²Note that the fit is not forced to have a positive intercept.

Interestingly, C_{bckgd} can also be used directly to derive $X_{\text{NO,nsct}}$ without the explicit calculation of C_{lin} . This is shown using Eq. (35) to develop Eq. (54) into the following:

$$X_{\text{NO,nsct}} = \frac{F_{\text{NO-LIF,nsct}}}{F_{\text{NO-LIF,nsct+sd}} - F_{\text{NO-LIF,nsct}}} \cdot X_{\text{NO,sd}}. \quad (55)$$

Similarly, Eq. (52) can be derived to:

$$X_{\text{NO,nsct}} = (C_{\text{bckgd}} - 1) \cdot X_{\text{NO,sd}}, \quad (56)$$

which is directly equivalent to Eq. (55). Hence, when C_{bckgd} is obtained under the assumption of non-constant $F_{\text{interf.-LIF}}(\lambda)$, the calculation of C_{lin} can be avoided as it is already contained in C_{bckgd} . Such methodology, however, leads to an extrapolation of $X_{\text{NO,nsct}}$ from $F_{\text{NO-LIF}}$ using only one seeding level³, while several seeding levels can be used in the derivation of C_{lin} . Similar to C_{lin} , however, the transformation from C_{bckgd} to $X_{\text{NO,nsct}}$ must be performed under negligible NO reburn.

This leads to an important point when using this calibration technique under reburn conditions. When seeding the flame with several NO levels, reburn can be observed through a non-linearity of the LIF signal with seeding, assuming a non-linearity of the reburn fraction as seen in Fig. C.16 in Appendix. Instead, if only one seeding level is performed, it is impossible to determine if reburn is affecting the flames. Hence, it is preferable to ensure that there is no reburn in the flames (through a numerical or experimental analysis), and to proceed with at least two seeding levels, when possible.

Both techniques are compared later, in Fig. 10 and Fig. 11, where $F_{\text{NO-LIF}}(\lambda)$ is obtained using constant and non-constant $F_{\text{interf.-LIF}}(\lambda)$, respectively.

Assuming constant interfering LIF signal

The C_{lin} calibration methodology using the assumption of constant $F_{\text{interf.-LIF}}(\lambda)$ is presented in Fig. 10. Figure 10a presents the LIF profiles of flames with varying levels of NO seeding from 0 to 75 ppm as defined by Eq. (42). The measurements were repeated at least twice for each seeding level to ensure repeatability of the results, but only the averaged profiles are displayed for clarity. The $F_{\text{NO-LIF}}$ profiles demonstrate the scaling of the signal with the several levels of seeding. Additionally, it is clear that the temperature is the main driver of the signal through the change in NO number density, as shown through the strong signal in the unburnt region ($T \sim 300$ K) compared to the post-flame region ($T \sim 2000$ K). This highlights that the calibration coefficient is dependent on the local thermodynamic conditions and is, therefore, not applicable at other conditions unless correction for temperature, Boltzmann fraction, and quenching coefficient rates are applied [21]. This is also shown in Fig. 10b where the linear fit is performed in the unburnt and post-flame regions. For both positions, the extrapolation of the fit to a zero LIF signal leads to the produced NO molar fraction. Results of the extrapolation at each point of the axial domain are reported in Fig. 10c where the complete NO molar fraction profile of the flame is presented in ppm along with its uncertainty (shaded grey area). It presents the expected characteristics of a NO profile of a methane-air flame at moderate temperatures: first, a rapid production of NO through the

³Nevertheless, the calculation could be performed several times using several seeding levels.

flame front mostly attributable to the prompt-NO pathway and, second, a slower increase of NO in the post-flame region mostly driven by the thermal-NO pathway [63]. The determination of $X_{\text{NO},\text{nsc}}$ through this technique leads to an uncertainty of $\epsilon_{X_{\text{NO},\text{nsc}}|C_{\text{lin,constant interf.-LIF}}} \sim 3\text{--}8\%$, for which calculations are detailed in Appendix D.

Assuming non-constant interfering LIF signal

The linear extrapolation from seeded to nascent NO concentrations calibration methodology using the assumption of non-constant $F_{\text{interf.-LIF}}(\lambda)$ is presented in Fig. 11. The iterative process to determine C_{bckgd} is applied to each axial location of the domain for a given seeding level, as shown in Fig. 11a, along with its sextic Bézier curve. The higher is the seeding, the lower is the value of C_{bckgd} , as expected from Eq. (52). With the knowledge of C_{bckgd} , $F_{\text{NO-LIF,nsc}}(\lambda_{\text{on}})$ can be calculated

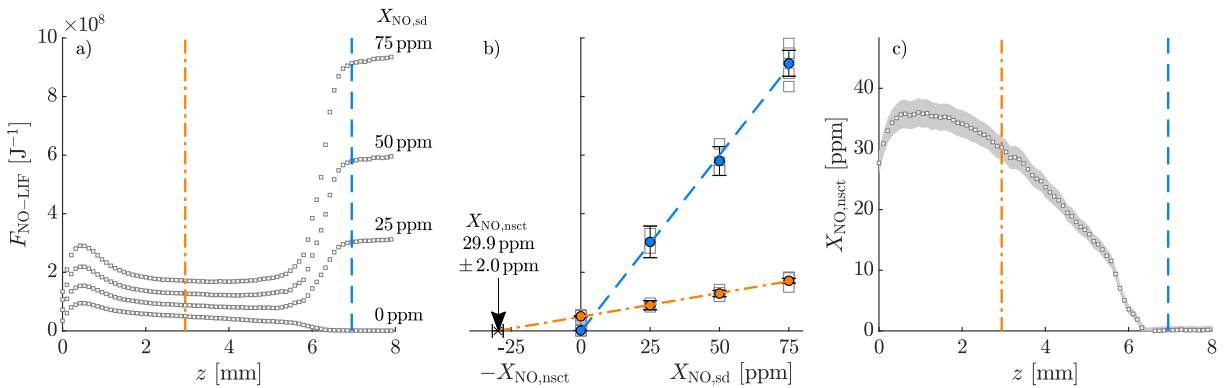


Figure 10: Linear fit calibration technique applied on the Phi0.9_Tad2130K_O21 flame assuming constant $F_{\text{interf.-LIF}}(\lambda)$: a) Experimental NO-LIF profiles obtained for an unseeded and three NO-seeding levels; b) Linear fit applied on the NO-LIF signal versus the known NO molar fraction at two axial locations (blue at $z = 7$ mm and orange at $z = 3$ mm) allowing the extrapolation of NO produced by the unseeded flame; c) Post-calibration NO molar fraction profile in ppm.

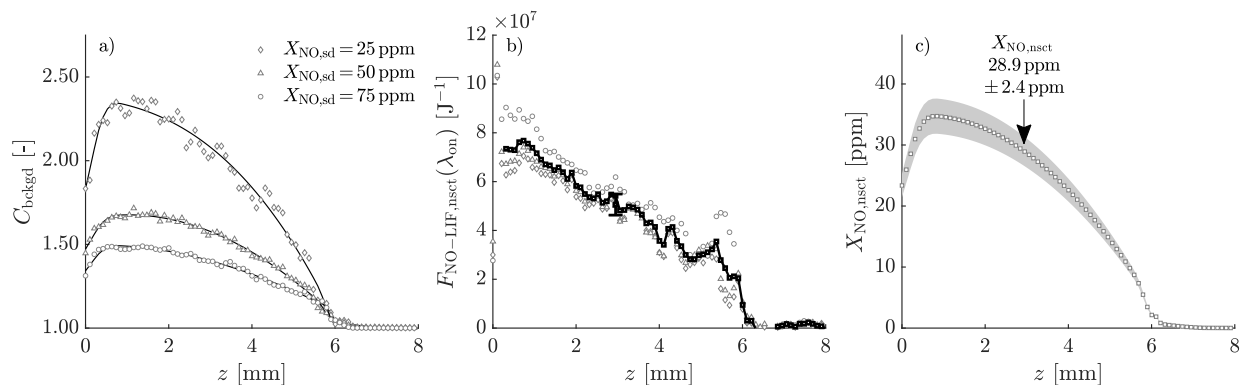


Figure 11: Transformation of the NO-LIF signal obtained for the Phi0.9_Tad2130K_O21 flame using C_{bckgd} to calculate $X_{\text{NO,nsc}}$: a) C_{bckgd} profiles (symbols) obtained for a single flame using three seeding levels and its fitted sextic Bézier curve (lines); b) $F_{\text{NO-LIF,nsc}}(\lambda_{\text{on}})$ calculated for an unseeded flame at every point of the domain using the three C_{bckgd} profiles (diamonds, triangles, and circles) and its average (black line and squares); c) $X_{\text{NO,nsc}}$ profile calculated using Eq. (56), resulting from an averaging of profiles.

as shown in Fig. 11b. Fig. 11a-b demonstrates that $F_{\text{NO-LIF,nsct}}(\lambda)$ can be calculated independently of the seeding value used. This is seen through the consistency of the calculated $F_{\text{NO-LIF,nsct}}(\lambda_{\text{on}})$ profiles from the three different C_{bckgd} profiles in Fig. 11b. Note that, for clarity, only the averaged profile for each seeding was presented, despite several measurements being performed to ensure repeatability.

As mentioned previously, the profile obtained in Fig. 11b is not directly comparable to the one obtained in Fig. 10a because the experimental configuration has been modified between the measurements. Specifically, the number of laser pulses and, therefore, images accumulated on the ICCD camera, per wavelength, is different, changing the signal-to-noise ratio. Additionally, the subtraction of $F_{\text{NO-LIF,nsct}}(\lambda_{\text{off}})$ from $F_{\text{NO-LIF,nsct}}(\lambda_{\text{on}})$ performed assuming constant $F_{\text{interf.-LIF}}(\lambda)$ can lead to an underestimated signal if some NO-LIF signal is present at the offline wavelength (through broadening for example), whereas the technique performed assuming non-constant $F_{\text{interf.-LIF}}(\lambda)$ ensures that $F_{\text{interf.-LIF}}(\lambda)$ is free of any unduly subtracted NO-LIF contribution. Hence, in order to be comparable to one another, the flame data need to be normalised by C_{opt} obtained in each experimental configuration, as seen in Fig. 9, and explained later in this work, see Section 4.2.2.

Finally, the calculation of $X_{\text{NO,nsct}}$ using Eq. (56) is shown in Fig. 11c. The NO molar fraction profile of the flame is presented in ppm along with its uncertainty. The determination of $X_{\text{NO,nsct}}$ through this technique leads to an uncertainty of $\epsilon_{X_{\text{NO,nsct}}|C_{\text{lin,non-constant interf.-LIF}}} \sim 8.5\%$, and its calculation is detailed in Appendix D. The profile presents similar characteristics to the one presented in Fig. 10c. The direct comparison of both profiles is performed later in this study, see Section 5.

Applicability of the technique

This calibration technique yields a quantitative measurement of the NO contained in the flame regardless of the assumption formulated on $F_{\text{interf.-LIF}}(\lambda)$. The resulting NO molar fraction profiles obtained experimentally are directly comparable to numerical results obtained from a thermochemical model through the use of a combustion modelling software.

To measure the NO produced by a flame, this calibration technique requires the seeding of the flame by at least one seeding level in order to obtain C_{lin} or C_{bckgd} depending on the assumption on $F_{\text{interf.-LIF}}(\lambda)$. Naturally, the higher the number of seeded flames, the more certain is the fit, and the more constrained the confidence interval, see Appendix D. Additionally, it is crucial that the experimental setup remains undisturbed between the unseeded and seeded flame measurements to ensure the consistency of $(f_{\text{LIF}} \cdot C_{\text{opt}})$.

This technique is often used in the literature, see Section 2.2.2, as it is simple to post-process, does not require any LIF modelling, is based on assumptions that are easy to verify and fulfil, and is valid for the entire flame domain. It can, however, be challenging to use if many flames have to be studied, as it requires at least twice the experimental time and cost to obtain quantitative NO measurements of a single flame. Furthermore, an *a priori* estimation of the NO produced in the flame is required in order to seed the flame with NO levels of the same order of magnitude as the NO produced by the unseeded flame. Seeding levels that are too far from the produced NO would lead to a more uncertain extrapolation. Additionally, seeding levels that are too large would lead to significant reburn throughout the flame domain. This is demonstrated in Appendix C.1 where, for some flame conditions, significant reburn is present with even low levels of seeding, especially in rich flames. This leads to a calibration technique whose applicability is limited mostly to lean to stoichiometric and low to moderate pressure premixed flames. This technique is also inapplicable

in the case of flames containing molecules that are known to favour reburn, such as NH_3 , regardless of the pressure or stoichiometry of the flame. Finally, this technique can only be performed in flames that are time-averaged due to the requirement to seed the flame. Hence, it can be applied in temporally-stable flows, such as bunsen or flat flames, leading to an accurate quantification of the NO produced. It can also be applied in temporally-unstable flows, such as turbulent flames, but this will result in a less resolved and accurate measurement of NO due to the time-averaging of the signal.

To avoid significant experimental time, the calibration can also be done on a single flame and at a single point of the domain. This is done by accounting for the quenching effects and temperature differences between the calibration point and the points on which the transformation is applied. Therefore, this technique requires an assumption of the flame composition to extract the quenching coefficients, as well as the temperature, at each point of the domain [21, 47]. This variant of the calibration technique is effectively equivalent to the methodology presented next, using C_{opt} , where f_{LIF} is modelled.

4.2.2. C_{opt} : Optical calibration using experimental and modelled LIF parameters - Assumption of non negligible NO reburn

As discussed in the previous section, the calculation of $X_{\text{NO,nsct}}$ using C_{lin} or C_{bckgd} is only valid for a given axial position of the flame domain as the changes in temperature and composition throughout the domain affect f_{LIF} . This can be resolved by modelling the signal using its local flame-dependent parameters: the temperature and pressure, the quenching rate, the overlap fraction, and the Boltzmann fraction, as seen in Eq. (21). While, in theory, these parameters could be obtained experimentally, it is easier to get them numerically. Therefore, this technique depends on obtaining the LIF parameters through modelling.

This calibration technique relies on the determination of C_{opt} , a flame- and axially-independent coefficient that represents the optical parameters of the experimental setup⁴. As discussed in Section 2.2.2, C_{opt} is obtained by fitting experimental and modelled $F_{\text{NO-LIF}}$ profiles, as seen in Eq. (38). The comparison is performed on net profiles obtained through the difference of $F_{\text{NO-LIF}}(\lambda)$ of seeded and unseeded flames, such that the resulting signal, $F_{\text{NO-LIF,sd}}(\lambda)$, is only proportional to the known seeded molar fraction of NO ($X_{\text{NO,sd}}$), removing the contribution of the flame-produced NO (unknown *a priori*):

$$F_{\text{NO-LIF,sd}}^{\text{exp}}(\lambda) = F_{\text{NO-LIF,nsct+sd}}^{\text{exp}}(\lambda) - F_{\text{NO-LIF,nsct}}^{\text{exp}}(\lambda), \quad (57)$$

$$= [X_{\text{NO,nsct+sd}}^{\text{exp}} \cdot f_{\text{LIF}}^{\text{exp}} - X_{\text{NO,nsct}}^{\text{exp}} \cdot f_{\text{LIF}}^{\text{exp}}] \cdot C_{\text{opt}}, \quad (58)$$

$$\approx X_{\text{NO,sd}}^{\text{exp}} \cdot f_{\text{LIF}}^{\text{exp}} \cdot C_{\text{opt}}, \quad (59)$$

and similarly,

$$F_{\text{NO-LIF,sd}}^{\text{num}}(\lambda) = F_{\text{NO-LIF,nsct+sd}}^{\text{num}}(\lambda) - F_{\text{NO-LIF,nsct}}^{\text{num}}(\lambda), \quad (60)$$

$$= [X_{\text{NO,nsct+sd}}^{\text{num}} \cdot f_{\text{LIF}}^{\text{num}} - X_{\text{NO,nsct}}^{\text{num}} \cdot f_{\text{LIF}}^{\text{num}}], \quad (61)$$

$$\approx X_{\text{NO,sd}}^{\text{num}} \cdot f_{\text{LIF}}^{\text{num}}. \quad (62)$$

⁴Conveniently, the determination of C_{opt} could also be grouped with any other linear effects that cannot be easily measured in Eq. (21), such as an absolute energy measurement of the laser beam.

This relationship is particularly useful for this calibration technique where thermochemical models are used to obtain a calibration coefficient through LIF modelling. By using the net signal, $F_{\text{NO-LIF,sd}}(\lambda)$ is only dependent on $X_{\text{NO,sd}}^5$ and not on $X_{\text{NO,nsct}}$ for which thermochemical models can vary significantly. This is valid assuming that f_{LIF} is independent from the thermochemical model employed, as demonstrated in Appendix C.3. This requires that all thermochemical models predict the temperature and main quenching species (CO_2 , H_2O , N_2 , O_2 , and OH) profiles accurately.

The experimental net signal, $F_{\text{NO-LIF,sd}}^{\text{exp}}(\lambda)$, is obtained by subtracting the LIF signal of an unseeded flame from the seeded one. $F_{\text{NO-LIF,nsct+sd}}^{\text{exp}}(\lambda)$ and $F_{\text{NO-LIF,nsct}}^{\text{exp}}(\lambda)$ are calculated using either methodologies described in Section 4.1.

The numerical net signal, $F_{\text{NO-LIF,sd}}^{\text{num}}(\lambda)$, is also obtained by subtracting the LIF signal of an unseeded flame from the seeded one. $F_{\text{NO-LIF,nsct+sd}}^{\text{num}}(\lambda)$ and $F_{\text{NO-LIF,nsct}}^{\text{num}}(\lambda)$ are obtained using flame simulation and LIF modelling. Similarly to the experiments, simulations are performed by virtually seeding the flame with $X_{\text{NO,sd}}$. The Impinging Jet model in Cantera 3.0 [68] is used to simulate the experimental flames using the measured boundary conditions presented in Tab. 1 and Appendix A. Three thermochemical models are used: CRECK (v.2003) [69, 70], GRI (v.3.0) [71], and SD (v.2016-12+v.2018-07) [72]. They have been chosen due to their span of accuracy in predicting NO measurements in a previous methane-air flame campaign [63]. The CRECK and GRI thermochemical models have shown the best agreement with the measured NO, while SD displayed the worst. Additionally, CRECK is one of the most comprehensive thermochemical models available to the community, while GRI and SD are simpler models validated for a limited set of fuels [51]. The choice of these models was made to demonstrate that the C_{opt} calibration technique is minimally dependent on the accuracy of the thermochemical model in predicting $X_{\text{NO,nsct}}$ (see Appendix C.3 for demonstration).

The numerical flame results are fed to LIFSim [32], a linear 3-level NO-LIF model, to transform a numerically-obtained NO molar fraction profile ($X_{\text{NO}}^{\text{num}}$) to a numerical LIF profile ($F_{\text{NO-LIF}}^{\text{num}}(\lambda)$) by modelling $f_{\text{LIF}}^{\text{num}}$. Calculations are made assuming a linear regime, consistent with the experimental conditions used in this study. Extremely fast Rotational Energy Transfer (RET) is assumed leading to an equilibrium population in the ground states. The fluorescence modelled by the software is a summation of A_{21} and A_{23} , neglecting pre-dissociation and photo-ionisation. In the case of several transitions being excited by the laser, the total LIF signal is a summation of the fluorescence calculated for each individual transition. The output is a spectrally-resolved LIF signal, per pulse, $\mathcal{S}_{\text{NO-LIF}}$ [10^{-17} W], for a given set of flame condition, and laser and detection parameters. To appropriately model the experimental configuration that comprises a filter and a camera with their own transmissivity and quantum efficiency, the LIF signal obtained from LIFSim is integrated from 220 nm to 340 nm (corresponding to the 8th vibrational band) at each location of the domain. Finally, the integrated signal is multiplied by the NO number density from the flame simulation, such that:

$$F_{\text{NO-LIF}}^{\text{num}}(\lambda) = \int_{\lambda_{\text{collection}}} \mathcal{S}_{\text{NO-LIF}} \cdot n_{\text{NO}}^{\circ} \cdot d\lambda_{\text{collection}}. \quad (63)$$

Additional parameters used in LIFSim to obtain $F_{\text{NO-LIF}}^{\text{num}}(\lambda)$ are detailed in Appendix B.

⁵This is valid assuming negligible reburn.

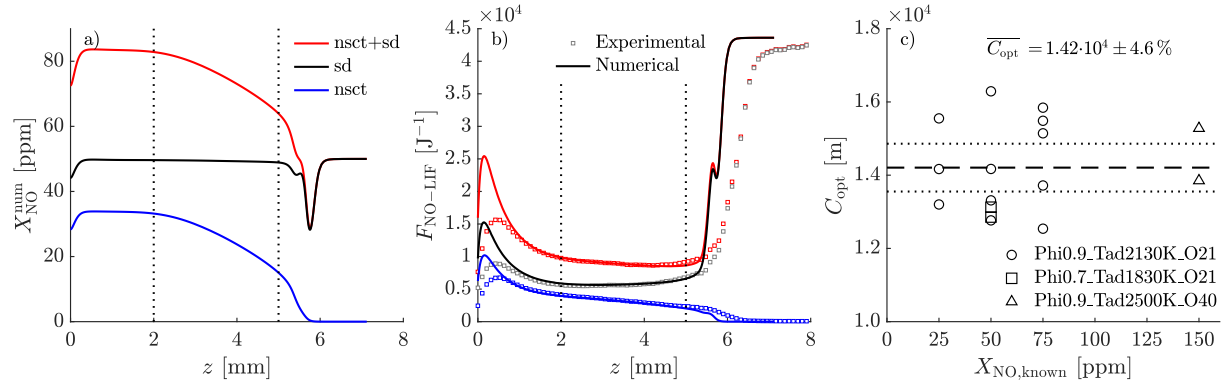


Figure 12: C_{opt} calibration technique: a) Numerical NO profiles for the flame Phi0.9_Tad2130K_O21 unseeded (blue line), seeded with 50 ppm of NO (red), and the resulting net profile (black) using the GRI thermochemical model, along with the axial bounds within which $X_{\text{NO}}^{\text{num}}$ remains constant (dotted lines); b) LIF numerical profiles (solid lines) and C_{opt} -normalised experimental LIF profiles (squares) of the flame unseeded (blue), seeded (red), and net (black), along with the axial bounds within which C_{opt} was fitted (dotted lines); c) Calibration coefficient C_{opt} obtained for 16 flames at varying levels of seeding and flame conditions, along with its average (dashed line) and its 95% confidence interval (dotted lines).

Assuming constant interfering LIF signal

Similar to the experiments, the numerical-LIF signal of each flame is obtained by calculating the difference between the online and offline signals:

$$F_{\text{NO-LIF}}^{\text{num}} = F_{\text{NO-LIF}}^{\text{num}}(\lambda_{\text{on}}) - F_{\text{NO-LIF}}^{\text{num}}(\lambda_{\text{off}}). \quad (64)$$

The direct comparison of $F_{\text{NO-LIF,sd}}^{\text{num}}$ and $F_{\text{NO-LIF,sd}}^{\text{exp}}$ allows the optical calibration coefficient (C_{opt}) to be determined, as depicted in Fig. 12. C_{opt} is found by fitting the experimental profile to the numerical one using a least-square fit, leading to:

$$F_{\text{NO-LIF}} = \frac{F_{\text{NO-LIF,sd}}^{\text{exp}}}{C_{\text{opt}}} = F_{\text{NO-LIF,sd}}^{\text{num}}, \quad (65)$$

within the selected axial locations where there is negligible reburn, as discussed in Appendix C.1.

Once the LIF experimental signal of a flame is normalised by C_{opt} , the signal becomes independent of the optical parameters. Therefore, the C_{opt} -normalised signal obtained from several flames using different optical setups can be compared quantitatively relative to each other. On the contrary to the C_{lin} extrapolation technique, C_{opt} can be obtained once, and applied to any flame produced using the same optical configuration; it relies on the assumption that the optical parameters remain constant between the calibration and measurement flames. Hence, the technique can be applied regardless of NO reburn; if the coefficient is obtained under conditions of negligible reburn, it can then be applied to measured flames experiencing reburn or not. If the coefficient is obtained under non-negligible reburn, the C_{opt} calibration technique can still be applied provided that the thermochemical model correctly predicts the reburn chemistry⁶.

⁶This is necessary to assume $X_{\text{NO,sd}}^{\text{num}} = X_{\text{NO,sd}}^{\text{exp}}$ in the demonstration performed in Appendix C.4.

Figure 12 displays the process for determining C_{opt} . Figure 12a presents the NO molar fraction profiles of a numerical flame without, and with, NO seeding. The difference of these two signals, $X_{\text{NO,sd}}^{\text{num}}$, is also plotted. This curve shows that the NO molar fraction remains constant within the axial bounds chosen in the post-flame region to determine C_{opt} (dotted lines). These axial bounds were chosen as they represent the post-flame region where NO reburn is negligible, as shown in Appendix C.1, and where composition of the main species, specifically the quenchers, have reached equilibrium.

The numerical profiles are processed through LIFSim and subtracted from one another to obtain the net NO-LIF numerical profile $F_{\text{NO-LIF,sd}}^{\text{num}}$ as shown in Fig. 12b. Following Eq. (65), $F_{\text{NO-LIF,sd}}^{\text{exp}}$ is fitted to $F_{\text{NO-LIF,sd}}^{\text{num}}$ within the axial bounds by adjusting C_{opt} through a least-square minimisation. The resulting C_{opt} -normalised experimental profiles ($F_{\text{NO-LIF}}^{\text{exp}}/C_{\text{opt}}$) are also shown on Fig. 12b. Within the axial bounds, the numerical and experimental profiles match almost perfectly using the GRI thermochemical model. Using another thermochemical model whose accuracy in the prediction of the NO formation is worse than GRI would, however, lead to discrepancies between the numerical and experimental seeded and unseeded profiles. Nevertheless, it is demonstrated that despite these mispredictions, the net profiles remain almost perfectly predicted regardless of the model and the amount of seeding (see Appendix C.3). This demonstrates the effectiveness of using the net profile to determine the calibration coefficient since it is independent of the thermochemical model prediction accuracy.

This technique is valid with greater accuracy in the post-flame region where the net NO molar fraction remains constant. Potential mispredictions in the flame kinetics by thermochemical models can also lead to displacement of the profile in the axial direction, as seen with the unseeded flame in Fig. 12b. Furthermore, misprediction of temperature-dependent parameters seem to lead to the disagreement observed in the unburnt region, between the net experimental and modelled LIF signal. Due to the incapacity to prove that experimentally, the authors believe that this disagreement stems from an inaccurate prediction of the temperature-dependent quenching cross-section of the species involved in the cold and hot regions of the flame by LIFSim. Indeed, the calculation of the quenching cross-section in LIFSim is performed using the experimental results of Paul *et al.* [73, 74], while more recent results, published by Tamura *et al.* [75] and Settersten *et al.* [76, 77] indicate different temperature-dependencies for several of the most important quenchers. An inaccurate description of the laser linewidth (experimentally inferred) could also lead to the observed temperature-dependent mispredictions in the unburnt region. As NO is not produced at very low temperatures, the fit of C_{opt} is better performed in the hot flow, a region representative of the conditions for NO formation. The fit would therefore be biased if the cold region was included. Despite this, the determination of the profile ($F_{\text{NO-LIF}}^{\text{exp}}/C_{\text{opt}}$) is still valid outside of the axial bounds, as C_{opt} is independent of the flame.

As discussed, the obtained C_{opt} is minimally dependent of the thermochemical model employed for simulations, it is also independent of the amount of NO seeded in the unburnt mixture, and to the flame condition used (under the assumption of negligible reburn), as shown in Fig. 12c. For the three flames presented in Tab. 1, several levels of NO seeding were used to calculate C_{opt} . Measurements were performed several times to ensure repeatability and to reduce random uncertainty. The calculated C_{opt} for all these conditions demonstrate the independence of the technique with the flame condition and is presented in Appendix C.4. Therefore, only one calibration flame is needed for flames going from lean to rich conditions, although several flames would be recommended for higher confidence in the calculation of C_{opt} . In cases where reburn is not avoidable, this technique

remains valid but needs to be employed with a thermochemical model that accurately predicts the reburn chemistry for at least one condition targeted by the experimental study.

Assuming non-constant interfering LIF signal

The calculation process was repeated assuming non-negligible interfering LIF. For consistency with the experimental profiles, $F_{\text{NO-LIF}}^{\text{num}}$ is obtained by calculating the signal at the online wavelength:

$$F_{\text{NO-LIF}}^{\text{num}} = F_{\text{NO-LIF}}^{\text{num}}(\lambda_{\text{on}}), \quad (66)$$

as LIFSim only outputs the fluorescence of the NO molecules and does not contain the fluorescence of interfering species⁷. Hence, $F_{\text{NO-LIF}}^{\text{num}}$ slightly differs between both assumptions, $\sim 9\%$, proportional to the numerical signal produced at the offline wavelength due to line broadening, see Fig. 5.

A new C_{opt} is required as the experimental configuration is slightly different for both background subtraction methods, as discussed in Section 4.1, namely the number of images captured on the camera per pulse and the calculation of $F_{\text{NO-LIF}}^{\text{num}}$. The process to obtain C_{opt} , however, does not differ between both assumptions. Results are not presented for the sake of conciseness. The newly obtained averaged C_{opt} ($1.55 \cdot 10^4$ m) is of the same order of magnitude, and, unsurprisingly, $\sim 9\%$ higher than the one obtained previously ($1.42 \cdot 10^4$ m). Nevertheless, once normalised by C_{opt} , the profiles obtained using both assumptions on $F_{\text{interf.-LIF}}(\lambda)$ are directly comparable. These are presented in Fig. 9, and thus, prove the effectiveness of C_{opt} in yielding experimental LIF profiles independent from their configurations.

The C_{opt} -normalisation of the $F_{\text{NO-LIF}}^{\text{exp}}$ profiles renders this calibration technique quantitative. The profiles are directly proportional to n_{NO}° . In contrast to the extrapolation technique, however, the profiles are not readily comparable to simulation profiles. In order to do so, two comparison methodologies can be employed: transforming numerical NO molar fraction profiles into NO-LIF profiles, or transforming experimental NO-LIF profiles into NO molar fraction profiles.

Transforming numerical NO molar fraction profiles into NO-LIF profiles

The advantage of comparing the numerical to experimental results in experimental units, *i.e.* transforming the numerical molar fraction profiles into predicted NO-LIF signals through Eq. (21), is to separate the propagation of numerical and experimental uncertainties and, therefore, perform a more accurate comparison of the results [78]. As per Eq. (22), the accurate measurement of some terms, such as the temperature or quencher concentrations, would be required to accurately obtain $f_{\text{LIF}}^{\text{exp}}$. With the availability of the complete simulation solution, however, it is easier and more accurate to transform the numerical NO molar fraction profile using its own prediction of temperature and quencher concentrations to obtain $f_{\text{LIF}}^{\text{num}}$.

To do so, the numerical NO molar fraction profiles are transformed into NO-LIF profiles using the methodology discussed previously to obtain $F_{\text{NO-LIF}}^{\text{num}}$. Thus, the uncertainties in the simulated NO-LIF profiles are limited to numerical ones: in the thermochemical model, Cantera, and LIF-Sim; while the experimental uncertainties are limited to the measurement of $F_{\text{NO-LIF}}$ and C_{opt} . The

⁷LIFSim has the possibility to generate O₂-LIF signals, but it was not used in this study.

experimental uncertainty of $F_{\text{NO-LIF}}/C_{\text{opt}}$ is estimated at $\epsilon_{F_{\text{NO-LIF,nsct}}/C_{\text{opt}}}|_{\text{constant interf.-LIF}} \sim 6\%$ under the assumption of constant $F_{\text{interf.-LIF}}(\lambda)$ and $\epsilon_{F_{\text{NO-LIF,nsct}}/C_{\text{opt}}}|_{\text{non-constant interf.-LIF}} \sim 12\%$ under the assumption of non-constant $F_{\text{interf.-LIF}}(\lambda)$.

While this transformation leads to a more accurate comparison of the numerical to experimental results, an absolute NO molar fraction, or concentration may, in certain instances, be required.

Transforming experimental NO-LIF profiles into NO molar fraction profiles

As discussed, the transformation of experimental NO-LIF profiles into NO molar fraction profiles is feasible if $f_{\text{LIF}}^{\text{exp}}$ can be measured or calculated. In this work, the direct measurement of the quencher concentration is not performed and, thus, $f_{\text{LIF}}^{\text{exp}}$ cannot be estimated directly. Under the assumptions of negligible NO reburn, and that thermochemical models can reproduce the general kinetics of the flame accurately, *i.e.* the flame temperature and main species concentrations, the experimental and numerical f_{LIF} can be assumed constant, such that:

$$X_{\text{NO,nsct}}^{\text{exp}} = \frac{F_{\text{NO-LIF,nsct}}^{\text{exp}}}{C_{\text{opt}}} \cdot \frac{X_{\text{NO,nsct}}^{\text{num}}}{F_{\text{NO-LIF,nsct}}^{\text{num}}}, \quad (67)$$

obtained by re-arranging Eq. (36–37), and Eq. (65).

With this technique, any numerical uncertainty will be propagated to the experimental NO molar fraction profile. It is, however, relatively difficult to obtain a quantification of the numerical uncertainties at play in such a scenario, either within the thermochemical model, the combustion simulation software, or the LIF modelling software. This is why, to apply Eq. (67) with minimal uncertainty, it is crucial to select the thermochemical model with the best agreement in terms of flame kinetics, through the measurement of the flame speed and temperature profiles, and through the direct comparison of the NO-LIF profiles aforementioned. Such methodology and its limitation are demonstrated in Fig. 13.

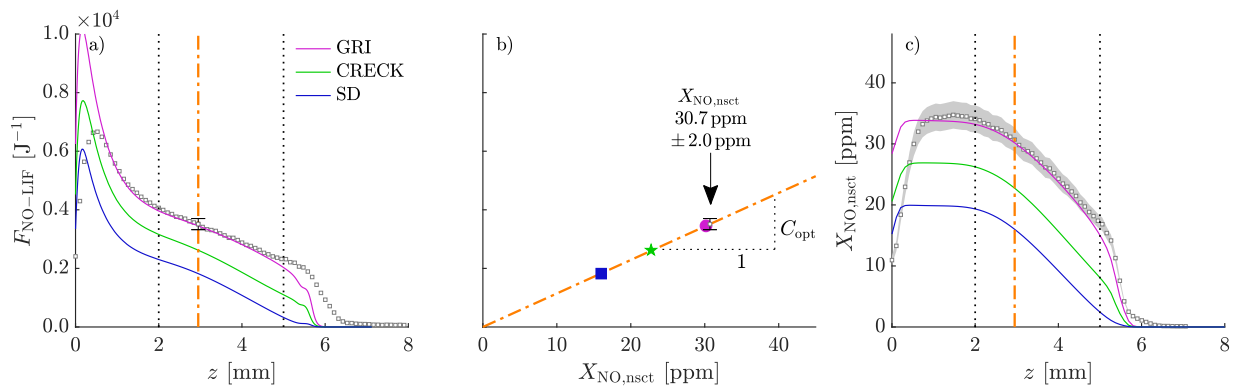


Figure 13: Transformation of the NO-LIF signal obtained using C_{opt} to $X_{\text{NO,nsct}}^{\text{exp}}$ on the Phi0.9_Tad2130K_O21 flame: a) Comparison of the experimental (squares) to the numerical (coloured lines) NO-LIF profiles using different thermochemical models (GRI - magenta, CRECK - green, SD - blue), b) Linear fit of the NO-LIF signal to NO concentration at a given location, c) Post-transformation NO concentration profile in ppm compared to the numerical predictions using the GRI thermochemical model.

In Fig. 13a, the C_{opt} -normalised experimental NO-LIF profile ($F_{\text{NO-LIF}}^{\text{exp}}/C_{\text{opt}}$) is compared to numerical NO-LIF profiles ($F_{\text{NO-LIF}}^{\text{num}}$), using three thermochemical models of varying degrees of

accuracy in predicting NO concentration. This comparison is in itself enough to compare numerical to experimental NO-LIF profiles, as discussed above. In this figure, GRI leads to the best agreement in predicting the NO-LIF profile of the flame, while CRECK and SD show worse agreement. Importantly, none of the three models can accurately predict the flame front position as seen at $z \sim 6$ mm, showing a misprediction of the flame kinetics.

Following the observations made on the comparison of the NO-LIF profiles, the transformation of the experimental NO-LIF profile was performed using the GRI thermochemical model⁸ in Eq. (67). The calculation is performed at each axial location of the domain and is demonstrated at $z = 3$ mm in Fig. 13b. The calculation of $X_{\text{NO,nsct}}^{\text{exp}}$ follows closely the prediction made by GRI, as it is also the case for the NO-LIF profiles in Fig. 13a. It is interesting to note that all three thermochemical models fall on the same line whose slope is C_{opt} , further demonstrating the minimal dependence of C_{opt} (or $F_{\text{NO-LIF,sd}}^{\text{num}}$) on the thermochemical models under all assumptions mentioned before. Hence, due to a similar misprediction of the flame kinetics by all three models, the transformation of $F_{\text{NO,nsct}}^{\text{exp}}$ to $X_{\text{NO,nsct}}^{\text{exp}}$ could have been performed with any of the three models.

The resulting $X_{\text{NO,nsct}}^{\text{exp}}$ profile is plotted in Fig. 13c along with its uncertainty (shaded grey area). The numerical molar fraction are also plotted using coloured lines, similar to Fig. 13a. It is evident that the calculated NO molar fraction profile follows the trend seen in the NO-LIF profiles, it is best predicted by GRI and underestimated by CRECK and SD. With this methodology, the transformation is only valid in the region where C_{opt} is extracted due to the errors present in the thermochemical models predictions in the flame kinetics, seen through the delta in the flame front position. This is demonstrated in the flame-front region ($z \sim 6.5 - 5$ mm) where the experimental profile sits upstream of the numerical profiles in Fig. 13a, but is shifted downstream in Fig. 13c due to the model misprediction of the flame front position. A similar phenomenon is also occurring near the stagnation plate. This effect supports the use of a comparison based on the NO-LIF profiles rather than a transformation in molar fraction. Despite that, the NO concentration profile follows the expected trend of a methane-air flame at moderate temperatures, and leads to an uncertainty of $\epsilon_{X_{\text{NO,nsct}}}|_{C_{\text{opt,constant}} \text{ interf.-LIF}} \sim 6-12\%$ on $X_{\text{NO,nsct}}^{\text{exp}}$ depending on the flame condition, in the post-flame region. A larger uncertainty is present for the flame with a larger misprediction of the flame front position by the thermochemical model (Phi0.9_Tad2500K_O40).

Applicability of the technique

This calibration technique leads to a quantitative measurement of the NO contained in the domain, regardless of the assumption formulated on $F_{\text{interf.-LIF}}(\lambda)$. The experimentally obtained profiles can be compared to numerical results either through raw experimental units, or through molar fraction, leading to different uncertainties as described before.

To limit the propagation of numerical uncertainties (thermochemical model, Cantera, or LIF-Sim inaccuracies), the experimental and numerical results should be compared in experimental units [78]. In cases where an absolute NO measurement is needed, however, the experimental results can be transformed using numerical results of a thermochemical model that best reproduces the flame kinetics. In such instances, numerical inaccuracies are necessarily propagated to the NO molar fraction profile.

⁸The transformation is performed, despite mispredictions in the flame kinetics by GRI, for the sake of explanation and demonstration of its limit.

This calibration technique requires less experimental time and resources than the one employing seeding of the flame at several concentration levels. When employed with a LIF modelling software, it avoids the explicit calculation of each term of f_{LIF} . This technique has been employed in the literature, either through the denotation of C_{opt} [40, 43, 49–51, 63], or not [21, 34, 47, 48, 52, 79] where the parameters of f_{LIF} were individually determined. In conditions where modelling cannot be employed or where seeding cannot be performed, C_{opt} can be obtained experimentally, such as in another flow or flame that can be modelled, or using Rayleigh or Raman scattering signals [40, 58, 59], as long as the optical system of the experimental setup is kept the same. Finally, with C_{opt} being independent of the calibration flame (see Appendix C.4), the calibration can be performed once, on any flame, or flow, in which the previously-cited assumptions hold, and can then be applied to flames at any other condition. Therefore, in contrast to the C_{lin} calibration technique, C_{opt} could be obtained in lean, laminar, and low-pressure calibration flames, and then be applied to rich turbulent and non-premixed flames where NO reburn might be present.

The C_{opt} calibration technique, combined with the calculation of $F_{\text{NO-LIF}}(\lambda)$ under the assumption of non-constant interfering LIF signal, represents the largest span of applicability of the four techniques explored in this work. Hence, quantitative NO measurements can be obtained in flames with non-negligible NO reburn and non-constant interfering LIF signal, such as in high-pressure rich flames.

5. Comparison of the calibration techniques

Two calibration techniques for quantitative NO-LIF measurements have been presented in this article. Both techniques have been applied under two sets of assumptions regarding the calculation of $F_{\text{interf.-LIF}}(\lambda)$. The set of assumptions and hypotheses on which the four techniques rely must be carefully considered when comparing the obtained results in either $X_{\text{NO,nsct}}$ or $F_{\text{NO-LIF}}/C_{\text{opt}}$ form. Hence, the comparison of the techniques is performed in Fig. 14 through NO molar fraction profiles applied on a set of three flames, and in Tab. 2 where they are summarised in terms of their assumptions and experimental complexity.

Figure 14 presents the NO concentration profiles obtained for three flames, using the four quantitative techniques, as indicated in Tab. 1. For each technique and each flame, the NO concentration throughout the flame domain is plotted along with its individual uncertainty. Figure 14a presents the results of the four techniques for the flame Phi0.9_Tad2130K_O21. The results show a very good agreement, especially in the post-flame region where the prediction of $X_{\text{NO,nsct}}$, and its uncertainty, overlap almost perfectly. In this region, the uncertainty of each technique is in between ~ 6 and $\sim 13\%$. Some discrepancies can, however, be observed in the flame-front region, and close to the stagnation plate. This is mostly due to transformation of the $F_{\text{NO-LIF,nsct}}/C_{\text{opt}}$ profiles into $X_{\text{NO,nsct}}$ using a thermochemical model that inaccurately predicts the flame front position. Therefore, a larger uncertainty in these two regions is expected⁹. These results demonstrate the applicability of the four techniques on lean flames and moderate adiabatic temperatures.

Figure 14b presents the results of the C_{lin} and the C_{opt} calibration techniques on the low temperature flame Phi0.7_Tad1830K_O21 under the assumption of constant $F_{\text{interf.-LIF}}(\lambda)$. The results show a relatively good agreement between the two calibration techniques, within their uncertainty ranges of ~ 6 – 8% .

⁹The uncertainty analysis has been performed at $z = 3$ mm and applied to the rest of the profile, see Appendix D.

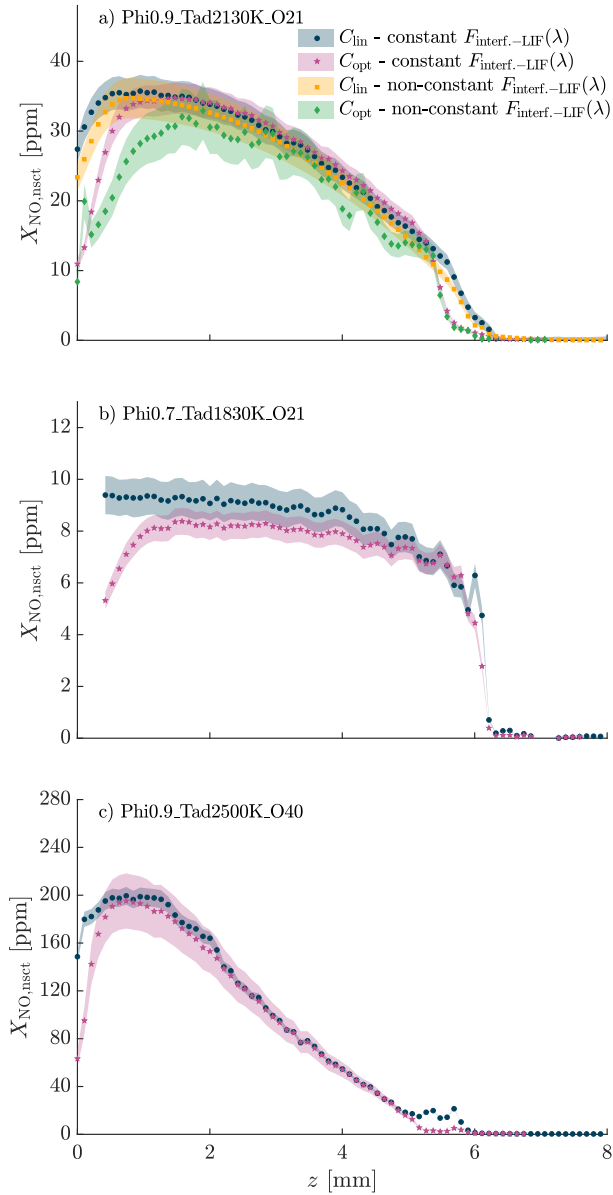


Figure 14: Comparison of the four quantitative techniques yielding $X_{NO,nsct}$ applied on three atmospheric, lean, methane flames.

Finally, Fig. 14c presents the results of the C_{lin} and the C_{opt} calibration techniques for the high temperature flame Phi0.9_Tad2500K_O40 under the assumption of constant $F_{interf.-LIF}(\lambda)$. For this flame, both techniques lead to a perfect overlap of $X_{NO,nsct}$, especially in the post flame region. As explained previously, discrepancies in the prediction of the flame front position by the thermochemical model underpredicts $X_{NO,nsct}$ in the flame front region for the C_{opt} technique.

These results demonstrate the applicability of each of the four techniques in the flame conditions performed in this work to obtain quantitative NO measurements through $X_{NO,nsct}$ or F_{NO-LIF}/C_{opt} , seen through Fig. 14 and Fig. 9, respectively. Furthermore, the assumptions, flame conditions, and experimental difficulty of each technique in the determination of $X_{NO,nsct}$ or F_{NO-LIF}/C_{opt} are sum-

marised in Tab. 2.

Table 2: Calibration techniques assumptions, applicability, and uncertainty.

Calibration technique	C_{lin}		C_{opt}	
	$X_{NO,nsct}$	$X_{NO,nsct}$	$X_{NO,nsct}$	$F_{NO-LIF,nsct}/C_{opt}$
Experimental results				
Assumption on $F_{nsct,LIF}(\lambda)$	Constant between λ_{on} and λ_{off}	Non-constant	Constant between λ_{on} and λ_{off}	Non-constant
Assumption on reburn	Negligible NO reburn in all flames.		Negligible NO reburn only in the calibration flame to obtain C_{opt} unless the reference thermochemical model can accurately predict it.	
Assumption on the thermochemical model	N/A		The reference thermochemical model must predict the flame kinetics and reburn accurately.	The reference thermochemical model must predict the flame kinetics accurately or another experimental methodology can be used to extract C_{opt} experimentally without numerical profiles.
Assumption on the calibration flame LIF regimes	The temperature and concentration of the main species remain constant between the unseeded and seeded flames.			
Preferred calibration flame conditions	Can be applied regardless of the LIF regime. Lean to stoichiometric flames. Low to moderate pressures. Low level of NO seeding.	Can be applied regardless of the LIF regime as long as the LIF modelling software is used in the same regime as the experimental one. Lean to stoichiometric flames. Low to moderate pressures. Low level of NO seeding.	Can be applied regardless of the LIF regime. Lean to stoichiometric flames. Low to moderate pressures. Low level of NO seeding.	Lean to stoichiometric flames. Low to high pressures. Low level of NO seeding.
Measured flame conditions	The calibration and measured flames must be the same.	C_{opt} can be applied to any flame condition under low to moderate pressures if the measured flame kinetics properties are accurately predicted by the reference model.	C_{opt} can be applied to any flame condition under low to moderate pressures. If the measured flame kinetics properties are accurately predicted by the reference model.	C_{opt} can be applied to any flame condition. $C_{hs,sgl}$ must be calculated for each measured flame.
Experimental and post-processing time and difficulty	Significant experimental time, as one to several seeding levels are required per flame to obtain C_{lin} . Relatively simple post-processing as LIF modelling is not required.	Extensive experimental time, as one seeding level is required per flame to obtain C_{lin} , as well as an excitation spectrum to obtain $C_{hs,sgl}$. Relatively simple post-processing as LIF modelling is not required.	Limited experimental time, only one C_{opt} is required per experimental configuration. Significant post-processing time through LIF modelling.	Limited experimental time, only one C_{opt} is required per experimental configuration. Significant post-processing time through LIF modelling.
Total uncertainty (see Appendix D for details on random and systematic sources)	~3–15% for one seeding level and depending on the flame condition. Decreases with the number of seeding levels.	~6–12% depending on the flame condition.	~13% for a given flame condition.	~6% for a given flame condition. ~12% for a given flame condition.

6. Conclusion

Four techniques to obtain quantitative NO-LIF measurements are compared in this work. The different experimental and post-processing approaches have been presented in detail, including uncertainty analysis, to collect available methods used in the community and provide an exhaustive guide for researchers to decide on an appropriate method of calibration in the context of their own experiments. The demonstration of the techniques is performed on three atmospheric, methane-air, stagnation flames with different adiabatic flame temperatures and equivalence ratios to study the applicability of the calibration techniques under varying experimental conditions. The four quantitative techniques result from the application of two calibration methodologies under which two background subtraction methods are applied. They all address two main difficulties in LIF measurement: background subtraction under the assumption of spectrally constant or non-constant interfering LIF signal, and seeding stability of the NO molecules through reburn. The comparison of the techniques, in atmospheric and lean conditions, has shown excellent agreement, highlighting their accuracy.

The first calibration methodology (C_{lin}) uses the linear extrapolation of the LIF signal from seeded to nascent NO concentrations. Used in combination with the assumption of spectrally constant interfering LIF signal from species other than NO, this technique is the most often used in the literature, but it also the one whose applicability is the most limited. It can only be applied under the condition of negligible reburn and constant flame conditions between the calibration seeded flames and the measured flame. This limits its application to flames from low to moderate pressures, at least to stoichiometric equivalence ratios, and whose seeding must be performed carefully to avoid reburn. Whilst the technique does not require LIF modelling and post-processing of the signal, it requires significant experimental time and samples to obtain the proportionality coefficient for each individual flame measured. The same calibration technique can be used under the assumption of non-constant interfering LIF signal. In this case, the technique could be applied to high pressures under the assumption of negligible reburn. This technique requires extensive experimental time, since the excitation spectrum of seeded and unseeded flames is required to obtain the quantification of NO produced by the flame.

The second calibration technique (C_{opt}) uses modelled LIF parameters to obtain the optical collection system coefficient. The calibration is performed on a single calibration flame (unseeded and seeded) and applicable to any other flame using the same experimental setup. This is possible through the independence of C_{opt} from the thermochemical employed to generate numerical LIF profiles. This calibration technique, when used under the assumption of constant interfering LIF signal, can be applied to any low to moderate pressure flames, even if there is reburn. This is possible if C_{opt} is obtained in a flame without reburn, or in cases where reburn is not avoidable, the thermochemical model used to determine C_{opt} must accurately predict the main thermodynamic and kinetic properties of the flame (temperature, main species concentrations, reburn) at least for one experimental condition. This methodology reduces the experimental time compared to the first calibration technique, but increases the time of post-processing because LIF modelling is required. Under the assumption of non-constant interfering LIF, the calibration technique can be extended to high pressure flames. Similarly to the previous approach, C_{opt} can be obtained once and applied to any flame. The interfering LIF signal, however, must be measured for all flames, increasing the experimental time required for this technique. The C_{opt} calibration technique, combined to the assumption of non-constant interfering LIF signal, has the largest span of applicability of the

four techniques presented. This calibration technique bears less uncertainty when experimental and numerical results are compared in raw experimental units [78]. In this instance, quantitative measurement of the NO contained in the flame can be performed once the LIF signal profiles are normalised by C_{opt} . In cases where an absolute molar fraction of NO is required, however, the signal can be transformed using the numerical solution, at the expense of propagating the uncertainty of the numerical model, whose quantification is challenging, onto experimental results. Hence, this calibration technique and its uncertainty was presented under both approaches.

This study presents a comprehensive demonstration of employing two calibration techniques for quantitative NO concentration measurements using LIF. While the LIF diagnostic techniques are performed on stagnation flames, their applicability also extends to other flames, provided that they can be seeded under similar conditions to the unseeded flame. Moreover, each approach, while demonstrated using NO, could be transposed to the concentration measurement of other species, as long as they are stable and can be seeded. When not possible, as for short-lived species such as CH or OH, the optical calibration methodology could still be employed, combined with another measurement, such as Rayleigh scattering [33, 58], to determine the C_{opt} of the experimental setup.

Ultimately, all techniques were proven to yield the same response, within uncertainty, either in molar fraction or in C_{opt} -normalised LIF profiles. Therefore, the choice of the calibration technique should be based on the test conditions and the resolution of the test matrix employed by the researcher. To support this choice, this work provides the theoretical models and underlying assumptions necessary to guide the use of each technique in future quantitative speciation measurements using Laser-Induced Fluorescence.

Acknowledgements

The authors would like to acknowledge the support of the Natural Sciences and Engineering Research Council of Canada (NSERC), Siemens Energy Canada Limited, Clinicals, and the Fonds de Recherche du Québec - Nature et Technologies (FRQNT).

CRedit authorship contribution statement

Marie Meulemans: Project administration, Conceptualization, Investigation, Methodology, Software, Formal analysis, Visualization, Writing – original draft.

Antoine Durocher: Conceptualization, Investigation, Methodology, Writing - Review and Editing.

Philippe Versailles: Conceptualization, Methodology, Formal analysis, Validation, Writing - Review and Editing.

Gilles Bourque: Supervision, Writing - Review and Editing.

Jeffrey M. Berghthorson: Conceptualization, Funding acquisition, Supervision, Writing - Review and Editing.

Appendix A. Experimentally measured boundary conditions

Table A.3 reports the experimental boundary conditions used to perform simulations of quasi-1D stagnation flames, along with their respective uncertainty in parentheses.

Table A.3: Boundary conditions and their respective uncertainty (in parentheses) for each flame produced in this study.

	p [atm]	\mathcal{L} [mm]	T_{in} [K]	T_{wall} [K]	u_{in} [m.s ⁻¹]	du_{in}/dz [s ⁻¹]	$X_{NO,sd}$ [ppm]	ϕ [-]	X_{O_2} [-]	X_{Ar} [-]
Phi0.9_Tad2130K_O21	1 (0.005)	7.12 (0.01)	291.3 (2)	402.3 (5)	0.545 (0.001)	156.4 (2.58)	0 (0.0)	0.90 (0.005)	0.21 (0.001)	0 (0)
							25 (0.1)	0.90 (0.096)	0.21 (0.023)	0 (0)
							50 (0.1)	0.90 (0.096)	0.21 (0.023)	0 (0)
							75 (0.2)	0.90 (0.096)	0.21 (0.023)	0 (0)
Phi0.7_Tad1830K_O21	1 (0.005)	7.62 (0.01)	293.5 (2)	361.5 (5)	0.266 (0.001)	61 (3.87)	0 (0.0)	0.70 (0.004)	0.21 (0.001)	0 (0)
							50 (0.1)	0.70 (0.167)	0.21 (0.051)	0 (0)
Phi0.9_Tad2500K_O40	1 (0.005)	6.84 (0.01)	291.9 (2)	501.9 (5)	1.575 (0.003)	472.7 (5.38)	0 (0.0)	0.90 (0.005)	0.40 (0.002)	0.3085 (0.00175)
							150 (0.4)	0.90 (0.005)	0.40 (0.002)	0.3085 (0.00840)

Appendix B. LIFSim parameters

Table B.4 presents the constants used in LIFSim to calculate the numerical NO-LIF signal.

Table B.4: Parameters used to obtain f_{LIF} in Eq. (21) using LIFSim.

Parameter	Notation	Value	Units	Source
LIFSim version		E 3.17		
Target molecule		NO		
Online excitation wavelength	λ_{on}	226.0345	[nm]	Experimental condition
Offline excitation wavelength	λ_{off}	226.0470	[nm]	Experimental condition
Laser energy density	I	7.8	[mJ·cm ²]	Experimentally measured
Laser pulse duration	τ_{pulse}	10.5	[ns]	Experimentally measured
HWHM of laser instrument Gauss function	$\Delta\nu_{L,Gauss}$	0.3926/2	[cm ⁻¹]	Experimentally inferred*
HWHM of laser instrument Lorentz function	$\Delta\nu_{L,Loren}$	0.1664/2	[cm ⁻¹]	Experimentally inferred*
Minimum detection wavelength	λ_{min}	220	[nm]	
Maximum detection wavelength	λ_{max}	340	[nm]	
Detection resolution	$\Delta\lambda$	0.01	[cm ⁻¹]	
HWHM of detection instrument function	$\Delta\nu_{det,Gauss}$	100	[cm ⁻¹]	LIFSim default value
HWHM of detection instrument function	$\Delta\nu_{det,Loren}$	10	[cm ⁻¹]	LIFSim default value
Detection instrument transmissivity	\mathcal{T}_λ	λ -dependent	[-]	Long-pass filter manufacturer
Pressure	p	1	[bar]	Experimental condition
Temperature	$T(z)$	z -dependent	[K]	Numerical solution
Composition	$X(z)$	z -dependent	[-]	Numerical solution
Quenching cross-section	σ_M	species-dependent**	[Å ²]	[73, 74]
Collisional coefficient	2γ	species-dependent***	[cm ⁻¹ ·atm ⁻¹]	[80–82]
Collisional shift coefficient	δ	species-dependent***	[cm ⁻¹ ·atm ⁻¹]	[80–82]

* Experimentally inferred by fitting a Voigt profile on an isolated NO transition

** Species included: N₂, O₂, CO₂, CO, H₂O, CH₄, C₂H₆, C₃H₈, C₂H₄, C₂H₂, NO, NO₂, N₂O, NH₃, NH, H₂, O, H, OH, CH, He, Ne, Ar, Kr, Xe

*** Species included: N₂, O₂, H₂O, Ar, CO₂, CO, CH₄

Appendix C. Assumptions and supporting evidence

C.1. Negligible NO reburn conditions

The assumption that negligible reburn occurs through the flame is valid depending on the amount of NO that is seeded in the flame. This is verified experimentally in lean low pressure methane-air flames seeded with up to 30,000 ppm [44]. This is also explored numerically for this

study. Figure C.15 presents the simulation results of NO-seeded flames at different levels ($X_{\text{NO,sd}}$). The flames were simulated according to the conditions presented in Tab. 1, and using three thermochemical models: CRECK [69, 70], GRI [71], and SD [72]. When seeding a flame, the mass flow rate of seeded NO ($\dot{m}_{\text{NO,sd}}$) is expected to remain constant. The calculation is performed on a mass basis as it is a conserved quantity, as opposed to a molar basis that changes with the formation or reaction of species other than NO. The mass flow rate of seeded NO can be calculated numerically through the difference of the NO produced in a seeded and unseeded flame. Calculations were performed such that:

$$\dot{m}_{\text{NO,sd}}(z) = \dot{m}_{\text{NO,nsct+sd}}(z) - \dot{m}_{\text{NO,nsct}}(z), \quad (\text{C.1})$$

and with

$$\dot{m}_{\text{NO,nsct+sd}}(z) = Y_{\text{NO,nsct+sd}}(z) \cdot \rho_{in} \cdot u_{in} \cdot A_{\text{nozzle}}, \text{ and} \quad (\text{C.2})$$

$$\dot{m}_{\text{NO,nsct}}(z) = Y_{\text{NO,nsct}}(z) \cdot \rho_{in} \cdot u_{in} \cdot A_{\text{nozzle}}. \quad (\text{C.3})$$

Hence, reburn can be defined as any mass flow rate of seeded NO that is lower than the initial seeded mass flow rate:

$$\text{Reburn fraction} = \frac{\dot{m}_{\text{NO,sd}}(z) - \dot{m}_{\text{NO,sd}}(z_{in})}{\dot{m}_{\text{NO,sd}}(z_{in})}, \quad (\text{C.4})$$

such that the reburn fraction represents the proportion of the seeded NO that reacted through the flame.

For each flame, the largest reburn occurs in the flame-front and close to the stagnation plate. A Reaction Pathway Analysis (RPA) performed on N from the inlet to the peak of NO reburn in the flame-front indicates that NO reacts to form mainly NO_2 . Near the stagnation plate, a RPA shows that NO reacts to form HONO instead. Most of the mass flow rate of NO is restored after the peak in the flame front thanks to the formation of NO from species such as HNO_2 , N, and NH. It demonstrates that calibration techniques assuming negligible NO reburn are only valid in the post-flame region, and should be used with care in the flame-front region of the flames. As seen through the reburn fraction evolution with z , NO reburn remains well under 5% for the three flames and for all seeding levels performed in this study, as well as for the three thermochemical models used.

An investigation is performed as well on which flame condition would lead to significant NO reburn. Figure C.16 presents the NO reburn fraction for a given thermochemical model at a fixed position of the post-flame region, by varying the level of seeded NO ($X_{\text{NO,sd}}$) in the initial mixture. The reburn fraction of flames at varying conditions is presented for lean ($\phi = 0.7$) and rich ($\phi = 1.3$) stoichiometries, and at atmospheric ($p = 1$ atm) and elevated pressures ($p = 8$ atm).

In lean and atmospheric conditions, the NO reburn fraction remains under 5% up to large NO seeding levels. In these conditions, the assumption that negligible reburn occurs is valid. With increasing pressure, still in lean conditions, reburn fractions above 5% occur at about 250 ppm of seeded NO. This indicates that, at elevated pressure conditions, lower seeding should be employed than for atmospheric conditions to avoid significant NO reburn. On the rich side, reburn fractions are consistently above 5%, except for very low seeding at atmospheric pressure (5 ppm), and three to four times more important at elevated pressures. Therefore, the assumption of negligible NO reburn in rich conditions ($\phi = 1.3$) is not valid, as expected.

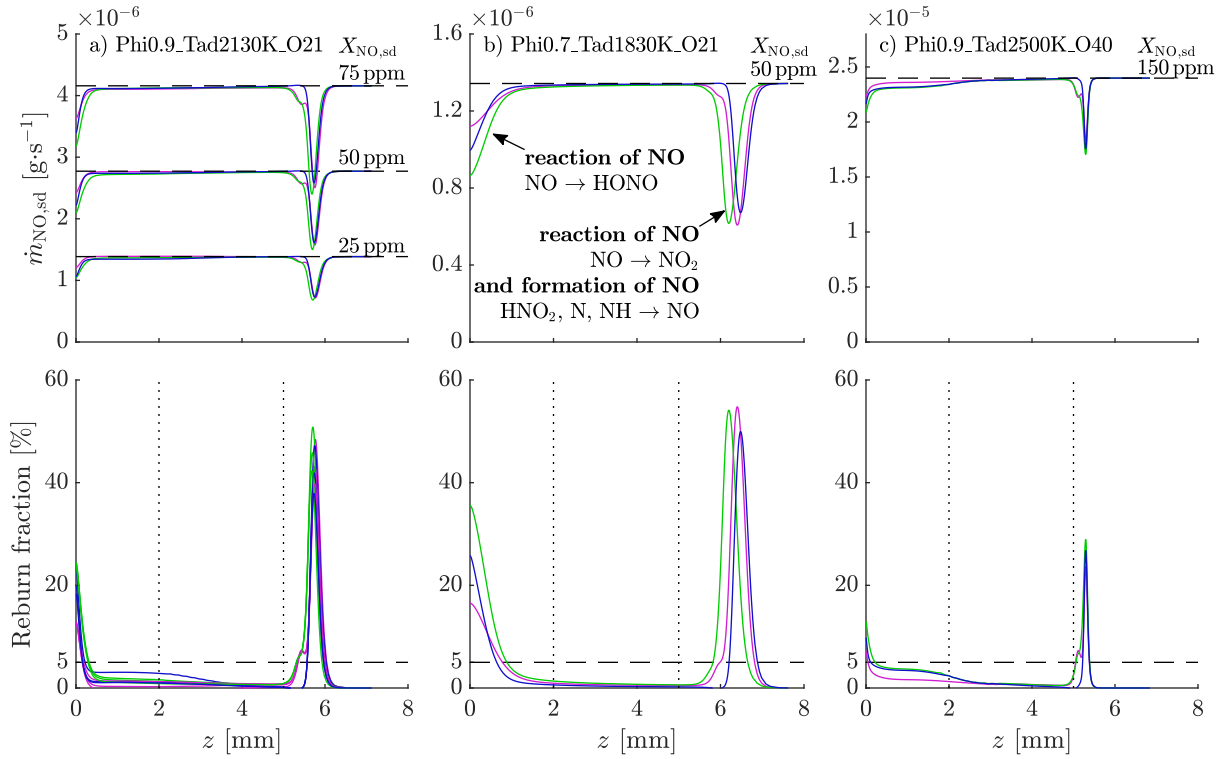


Figure C.15: NO reburn simulations performed for three flames: a) Phi0.9_Tad2130K_O21, b) Phi0.7_Tad1830K_O21, and c) Phi0.9_Tad2500K_O40, using three thermochemical models (CRECK —, GRI —, and SD —).

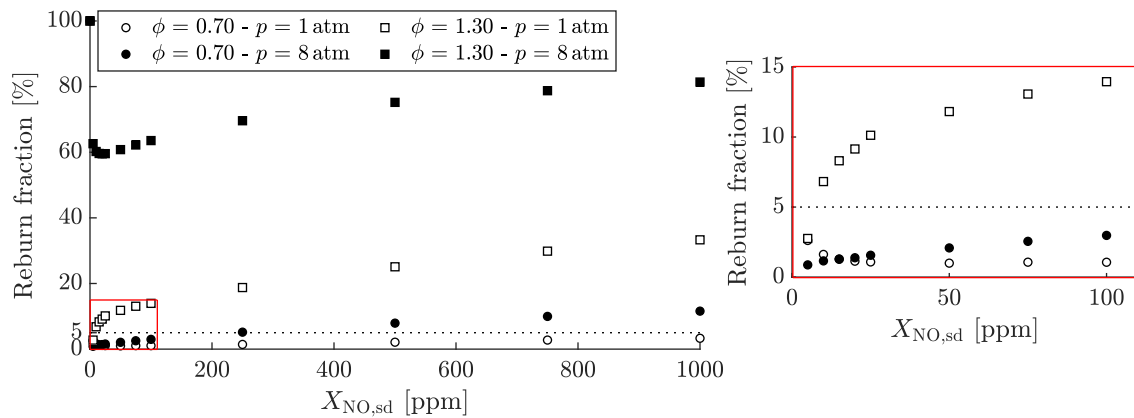


Figure C.16: NO reburn fraction calculated for several seeding levels in the post-flame region of four flame conditions: lean and atmospheric pressure (hollow circle), lean and elevated pressure (solid circle), rich and atmospheric pressure (hollow square), and rich and elevated pressure (solid square).

Ideally, these claims should be verified experimentally in conditions in which the flames will be performed. In conditions where NO reburn is observed, only the calibration technique employing the optical constant C_{opt} is valid. Two scenarios can occur using the C_{opt} calibration technique: 1) There is reburn in the measured flame but a calibration flame can be produced in conditions of negligible reburn. In this case, the determination of C_{opt} is not impacted by reburn, and the

coefficient can be applied to any flame. 2) There is reburn in the measured flame and in the calibration flame. In such scenario, it is important to select a thermochemical model that accurately predicts reburn to determine C_{opt} . Once obtained, the coefficient can be applied to any flame condition.

This investigation points at the applicability of the two calibration techniques presented in the main article. In the case of the extrapolation from seeded to nascent NO technique (C_{lin}), its applicability is limited to lean low-pressure flames. In the case of the optical calibration technique (C_{opt}), its applicability is not limited by reburn, as long as the coefficient is obtained in a flame that does not experience any reburn. As such, the coefficient can be obtained in low pressure lean flames and applied to rich or high pressure flames.

C.2. Constant temperature and concentration between the unseeded and seeded flames

The assumption of constant temperature and concentration of the main species between unseeded and seeded flames is necessary in order to assume that f_{LIF} remains constant between both flames. This is confirmed by calculating the relative difference of molar fraction of every major specie (defined as $X_s > 0.1$ ppm) of each seeded flame compared to the unseeded flame, as well as for the temperature, at the point of analysis (in the post-flame region). As only the molar fraction of NO is expected to vary significantly, due to the seeding, it is removed from the analysis.

Figure C.17 presents the relative difference calculated for each parameter, at a given location of the post-flame region, between each seeding level and the unseeded condition of the three flames performed in this study. For each flame, the relative difference remains under 1%. This demonstrates that negligible differences in temperature and species concentration occur between the unseeded and seeded flames. Therefore, the assumption that f_{LIF} remains relatively constant between the unseeded and seeded flame is valid for the flame and seeding levels studied.

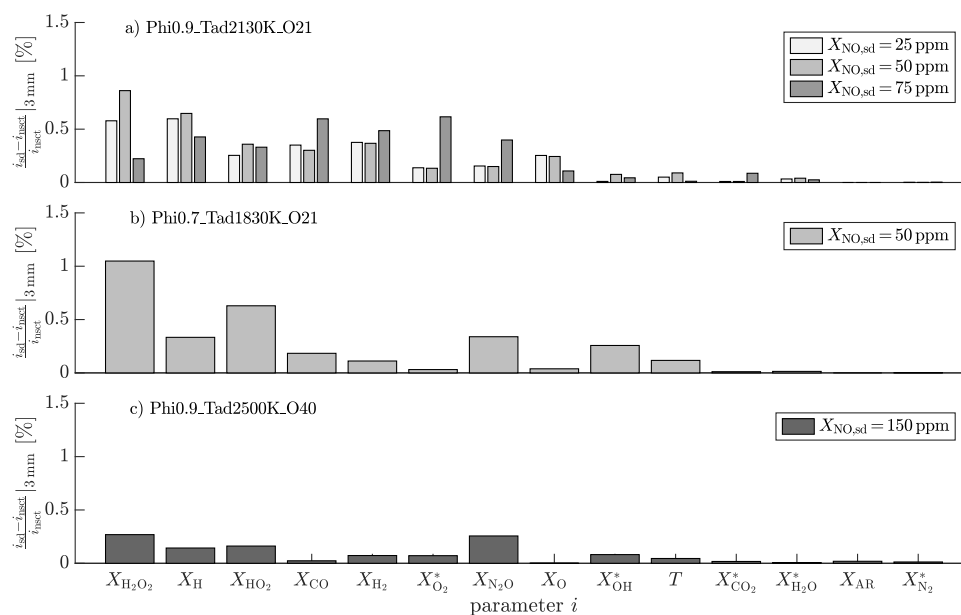


Figure C.17: Relative difference of parameter i between the seeded and unseeded simulation of a given flame: a) Phi0.9_Tad2130K_O21, b) Phi0.7_Tad1830K_O21, and c) Phi0.9_Tad2500K_O40, using the CRECK thermochemical model, at $z = 3$ mm. Molar fractions marked with * identify the main quenchers of these flames, see Section C.3.

C.3. The C_{opt} calibration technique is minimally dependent on the thermochemical model employed

In order to obtain C_{opt} , the flame is simulated using a thermochemical model and then transformed into a NO-LIF signal that can be compared to the experimental LIF signal. In the article, it is stated that any thermochemical model could be used to calculate C_{opt} , as long as the model captures relatively well the kinetics of the flame. This is possible through the use of the net LIF signal between a seeded and the unseeded flame to calculate C_{opt} .

This can be demonstrated using the 3-level linear LIF equation developed in Section 2.1.3, see Eq. (20-22):

$$F_{\text{NO-LIF}} = X_{\text{NO}} \cdot \overbrace{\frac{pf_B}{T}}^{\text{flame-dependent}} \cdot \overbrace{\frac{1}{\sum Q_{ul}}}^{\text{constants}} \cdot \overbrace{\frac{\mathcal{N}_A}{c\mathcal{R}_u}}^{\text{laser-dependent}} \cdot \overbrace{\frac{1}{\Delta\nu_L}}^{\text{line-dependent}} \cdot \overbrace{B_{12} \sum A_{ul}}^{\text{flame-laser-dependent}} \cdot \overbrace{\Gamma}^{\text{flame-laser-dependent}} \cdot \overbrace{\varepsilon_c \mathcal{T}_\lambda \frac{\Omega}{4\pi} \ell}^{\text{setup-dependent}}, \quad (\text{C.5})$$

Regrouping all experimental constants under the term α , the previous relationship simplifies to:

$$F_{\text{NO-LIF}} = X_{\text{NO}} \cdot \frac{pf_B}{T} \cdot \frac{1}{\sum Q_{ul}(X_s, p, T)} \cdot \Gamma \cdot \alpha, \quad (\text{C.6})$$

where only X_{NO} , p , T , f_B , Q_{ul} , and Γ are flame-dependent. Note that B_{12} and A_{ul} are only line-dependent and are also experimental constants in this case. In LIFSim, most of the setup-dependent parameters are not modelled, bringing their values to 1. Therefore, when determining C_{opt} following Eq. (65) by replacing $F_{\text{NO-LIF,sd}}^{\text{num}}$ with Eq. (C.6), it becomes¹⁰:

$$C_{\text{opt}} = \frac{F_{\text{NO-LIF,sd}}^{\text{exp}}}{\alpha \frac{X_{\text{NO,sd}} \cdot \frac{pf_B}{T} \cdot \Gamma}{\sum Q_{ul}(X_s, p, T)}}, \quad (\text{C.7})$$

where only $X_{\text{NO,sd}}$, p , T , f_B , Q_{ul} , and Γ are dependent on the prediction of the thermochemical model employed. As previously discussed, the pressure and temperature is generally properly captured by the thermochemical models, as it relies on the accurate prediction of major species. Thus, C_{opt} becomes only dependent on the thermochemical model through $X_{\text{NO,sd}}$ and X_s .

As shown in Fig. C.18, regardless of the level of accuracy of the thermochemical models (see Fig. 13), the profile of $X_{\text{NO,sd}}$ remains consistent. Therefore, C_{opt} is independent of the choice of the thermochemical model through $X_{\text{NO,sd}}$.

As for X_s , a sensitivity analysis is used to determine the most important species driving Q_{ul} for the three flames of the study. Figure C.19 presents the result of the sensitivity analysis performed on $F_{\text{NO-LIF}}^{\text{num}}$ at a given location of the post-flame region of the flames, for which the molar fraction of each quenching species was perturbed by 1%. Results show that, for all three flames, only about five species drive the quenching process: CO_2 , H_2O , N_2 , O_2 , and OH .

Comparing the predictions of the three thermochemical models for the species driving Q_{ul} , it shows that the predictions are relatively consistent between the thermochemical models, as shown

¹⁰Note that a simplification is done here, the direct measurement of the fluorescence of $X_{\text{NO,sd}}$ is not feasible, instead the difference of the seeded and unseeded fluorescence signal is obtained, following Eq. (59) and Eq. (62).

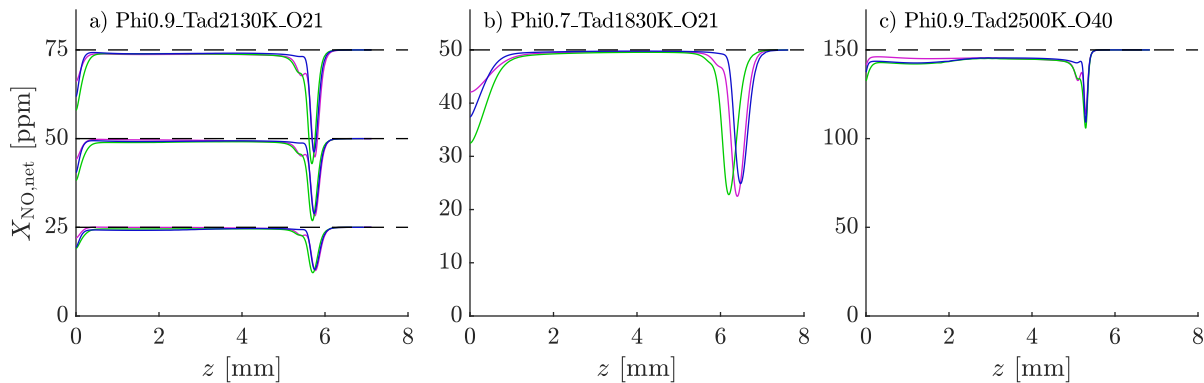


Figure C.18: Predictions of $X_{\text{NO,net}}$ for three flames: a) Phi0.9_Tad2130K_O21, b) Phi0.7_Tad1830K_O21, and c) Phi0.9_Tad2500K_O40, using three thermochemical models (CRECK —, GRI —, and SD —).

in Fig. C.20. Note that, even if the molar fraction of OH shows the largest variation between the models, it is also the species with the least impact on quenching, as seen in Fig. C.19. Thus, C_{opt} is also independent of Q_{ul} as the species driving it are consistently predicted by the different models.

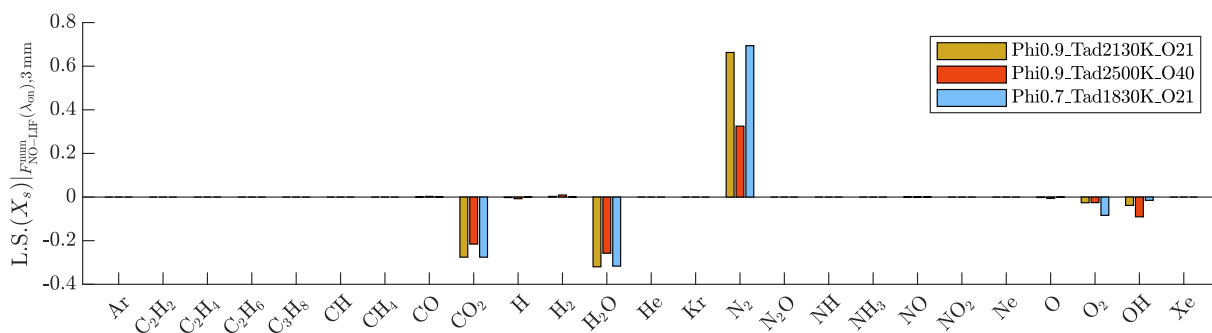


Figure C.19: L.S. of the NO-LIF signal by perturbing the molar fraction of the quenching species for the three flames, at $z = 3$ mm, using the CRECK thermochemical model.

These assumptions are also verified by generating C_{opt} for the three thermochemical models, widely varying in their level of accuracy in predicting NO (see Fig. 13). Results are shown in Fig. C.21. The values of C_{opt} obtained by averaging the results of the 16 individual flames for each thermochemical model are consistent and within the 95% confidence interval. This can be better understood by looking at individual profiles on which C_{opt} is calculated, as presented in Fig. C.22. For a selected seeding at each flame condition, it is evident that, despite the discrepancies observed in the seeded or unseeded profiles between the thermochemical model prediction and the experimental results, the net profile is in good agreement.

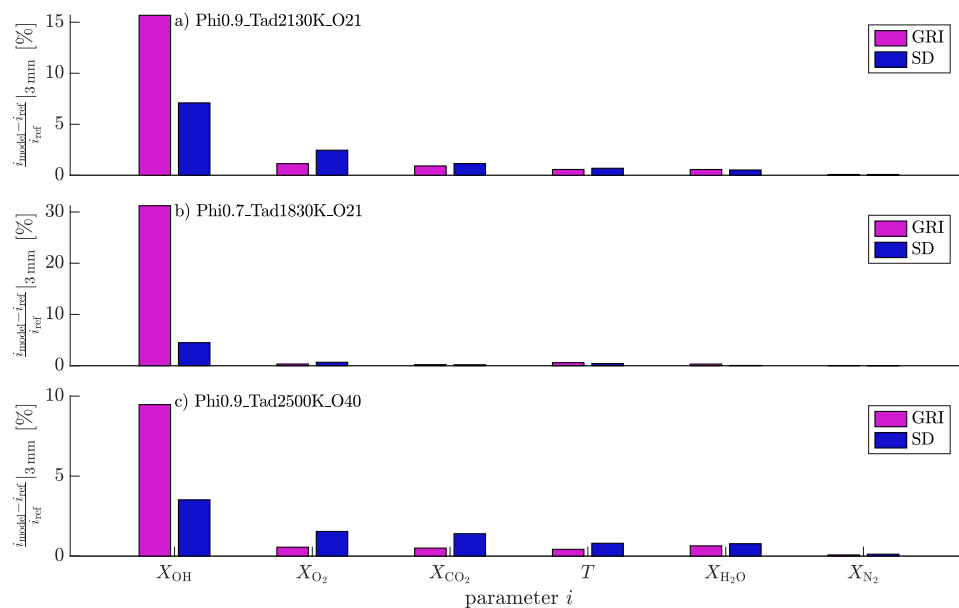


Figure C.20: Relative difference of parameter i between the CRECK model (reference) and the GRI and SD models of a given unseeded flame: a) Phi0.9_Tad2130K_O21, b) Phi0.7_Tad1830K_O21, and c) Phi0.9_Tad2500K_O40, at $z = 3 \text{ mm}$.

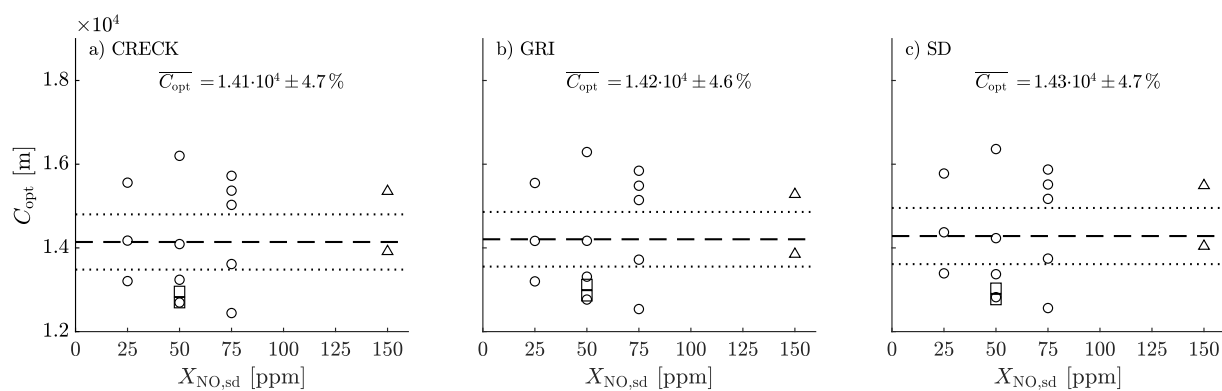


Figure C.21: C_{opt} calculated for all flame conditions (\square Phi0.9_Tad2130K_O21, \circ Phi0.7_Tad1830K_O21, \triangle Phi0.9_Tad2500K_O40), using three thermochemical models: a) CRECK, b) GRI, and c) SD. The dashed line represents the average value and the dotted lines represent the 95% confidence interval around the average.

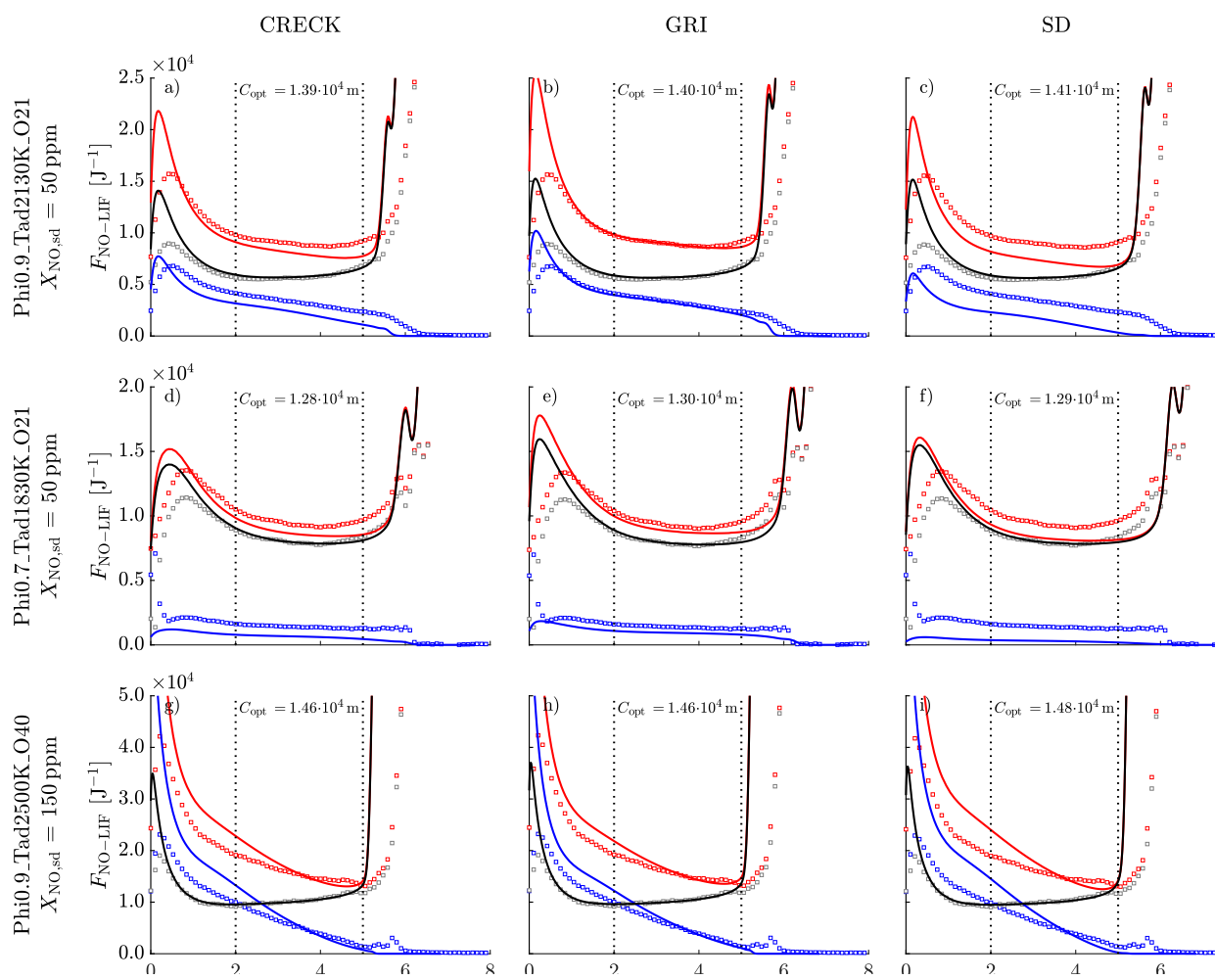


Figure C.22: LIF numerical profiles (solid lines) and LIF C_{opt} -normalised experimental profiles (squares) of the flame unseeded (blue), seeded (red), and net (black) for a selected seeding of each flame condition and for each thermochemical model.

C.4. C_{opt} is independent from the calibration flame

Similar to the previous demonstration, C_{opt} is demonstrated to be independent from the calibration flame, as long as the flame is not affected by NO reburn. As recalled from Eq. (39), C_{opt} is simply a coefficient regrouping all optical constants of the experimental setup.

In continuity with the previous demonstration, see Eq. (C.5), and assuming negligible NO reburn, C_{opt} is equivalent to:

$$C_{\text{opt}} = \frac{[X_{\text{NO,sd}} \cdot \frac{pf_B}{T} \cdot \frac{1}{\sum Q_{ul}} \cdot \frac{N_A}{cR_u} \cdot \frac{1}{\Delta\nu_L} \cdot B_{12} \sum A_{ul} \cdot \Gamma \cdot \mathcal{E}_c \mathcal{T}_\lambda \frac{\Omega}{4\pi} \ell]_{\text{exp}}}{[X_{\text{NO,sd}} \cdot \frac{pf_B}{T} \cdot \frac{1}{\sum Q_{ul}} \cdot \frac{N_A}{cR_u} \cdot \frac{1}{\Delta\nu_L} \cdot B_{12} \sum A_{ul} \cdot \Gamma \cdot \mathcal{E}_c \mathcal{T}_\lambda \frac{\Omega}{4\pi} \ell]_{\text{num}}}, \quad (\text{C.8})$$

where constants between the experiments and the simulations cancel each other, such that:

$$C_{\text{opt}} = \frac{X_{\text{NO,sd}}^{\text{exp}}}{X_{\text{NO,sd}}^{\text{num}}} \cdot \left(\frac{\mathcal{E}_c \mathcal{T}_\lambda \Omega \ell}{\sum Q_{ul}} \right)_{\text{exp}} \cdot \left(\frac{\sum Q_{ul}}{\mathcal{E}_c \mathcal{T}_\lambda \Omega \ell} \right)_{\text{num}} \quad (\text{C.9})$$

where T can be cancelled as it is measured experimentally, compared to predictions, and shown to be consistent; therefore $f_B(T)$ is also considered constant; p is also cancelled as the pressure is maintained constant throughout the experiments; B_{12} and A_{21} can be cancelled as they are constants relating to the LIF model chosen to model experiments; $\Delta\nu_L$ is measured experimentally and specified in LIFSim; and Γ is assumed perfectly modelled by LIFSim. Furthermore, assuming that $X_{\text{NO,sd}}^{\text{exp}} = X_{\text{NO,sd}}^{\text{num}}$ through the assumption that there is negligible NO reburn, and assuming that the major quenching species are properly modelled through simulations, such that $\sum Q_{ul}^{\text{exp}} = \sum Q_{ul}^{\text{num}}$, C_{opt} becomes fully independent of the flame condition, as well as the LIF model employed. It is a coefficient representing a conversion between the experimental and numerical optical parameters, encompassing the collection solid angle, the laser path length, the transmissivity of the optics, and the camera sensitivity:

$$C_{\text{opt}} = (\mathcal{E}_c \mathcal{T}_\lambda \Omega \ell)_{\text{exp}} \cdot \underbrace{\left(\frac{1}{\mathcal{E}_c \mathcal{T}_\lambda \Omega \ell} \right)_{\text{num}}}_{\sim 1}. \quad (\text{C.10})$$

Appendix D. Uncertainty analysis

Uncertainty calculations were performed for each calibration technique under both assumptions on $F_{\text{interf.-LIF}}(\lambda)$. The major terms driving the uncertainty are presented in the following section. Calculations were performed for each seeded and unseeded flame at $z = 3$ mm. For the sake of conciseness, only some results are shown below for the Phi0.9_Tad2130K_O21 flame.

D.1. Uncertainty on the experimental boundary conditions

Each boundary condition uncertainty specified in Tab. A.3 was calculated as follows:

- $\delta(p)$, $\delta(T_{\text{in}})$, and $\delta(T_{\text{wall}})$ stem from the experimental equipment;
- $\delta(\mathcal{L})$, $\delta(u_{\text{in}})$, and $\delta(\text{d}u_{\text{in}}/\text{d}z)$ are extracted from the post-processing of velocity measurements; and
- $\delta(X_{\text{NO,sd}})$, $\delta(\phi)$, $\delta(X_{\text{O}_2})$, and $\delta(X_{\text{Ar}})$ are calculated based on the number of MFCs used, their flow rates, and accuracy.

The uncertainty in $\delta(X_{\text{NO,sd}})$, $\delta(\phi)$, $\delta(X_{\text{O}_2})$, and $\delta(X_{\text{Ar}})$ is reduced when a minimal number of MFCs are used (as little as two MFCs controlling the fuel and air streams in an unseeded undiluted flame), and their individual flow rate is maximised since it is weighted by the uncertainty of the DryCal Piston calibrator, such that $\delta(\dot{m}_g) = \epsilon_{\text{DC}} \cdot \dot{m}_g$, with $\epsilon_{\text{DC}} = 0.4\%$.

D.2. Uncertainty on $F_{\text{NO-LIF}}(\lambda)$

D.2.1. Assuming constant $F_{\text{interf.-LIF}}(\lambda)$

The uncertainty on the averaged profile of $F_{\text{NO-LIF}}(\lambda)$ for an unseeded and seeded flames results from the contribution of the random and systematic errors. The first term encompasses experimental scatter and is reduced by the number of images captured and the number of flames performed for each condition, leading to a $\frac{\delta_{\text{rand}}(F_{\text{NO-LIF}})}{F_{\text{NO-LIF}}} \sim 3-4\%$.

The systematic uncertainty results from errors in the boundary conditions of the flames propagated to a fluorescence signal. Systematic errors in the photodiodes, the camera, and the long-pass filter are nil as they are assumed to have a linear effect on the signal captured and, thus, cancel through the calculation of $F_{\text{NO-LIF}}$. Hence,

$$\frac{\delta_{\text{sys}}(F_{\text{NO-LIF}})}{F_{\text{NO-LIF}}} = \left[\sum_{\text{BC}_j} \left(\text{L.S.}(\text{BC}_j) \Big|_{F_{\text{NO-LIF}}^{\text{num}}} \cdot \frac{\delta_{\text{sys}}(\text{BC}_j)}{\text{BC}_j} \right)^2 \right]^{1/2}, \quad (\text{D.1})$$

where $\text{L.S.}(\text{BC}_j) \Big|_{F_{\text{NO-LIF}}^{\text{num}}}$ is the logarithmic sensitivity (L.S.) of each boundary condition propagated to a fluorescence signal using Cantera and LIFSim and evaluated at $z = 3$ mm. Each term composing Eq. (D.1) can be found in Fig. D.23, where their L.S. (top), uncertainties (middle), and uncertainty-weighted L.S. (bottom) are shown. Results are presented for the unseeded and seeded (50 ppm) flames. The root-square-sum (RSS) of the terms leads to $\frac{\delta_{\text{sys}}(F_{\text{NO-LIF}})}{F_{\text{NO-LIF}}} \sim 3\% - 17\%$. For all flames, three parameters are driving the uncertainty: the equivalence ratio, the seeded NO molar fraction, and the argon molar fraction (when applicable). For these terms, the uncertainty is larger for flames performed with more MFCs and with low flow rates, such as seeding the flame with low levels of NO, or using a diluent.

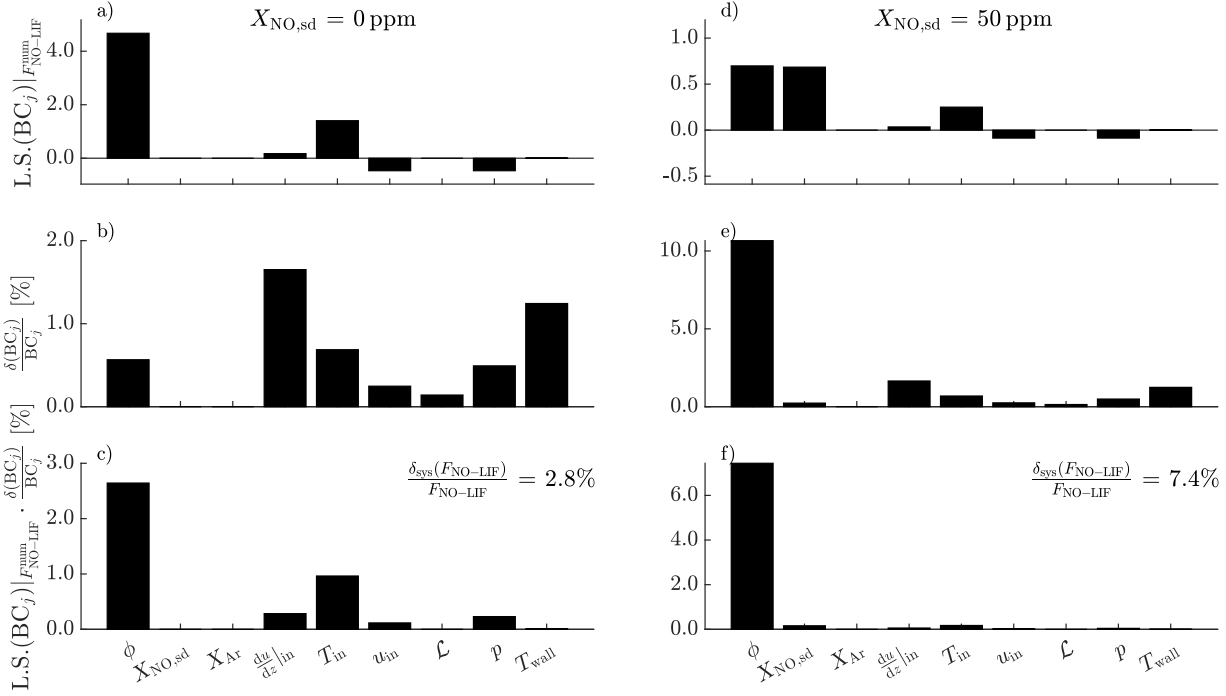


Figure D.23: L.S. (top), uncertainty (middle), and uncertainty-weighted L.S. (bottom) of the terms involved in the calculation of $\frac{\delta_{\text{sys}}(F_{\text{NO-LIF}})}{F_{\text{NO-LIF}}}$, for the unseeded (left) and seeded (right) Phi0.9_Tad2130K_O21 flames evaluated at $z = 3$ mm, assuming constant $F_{\text{interf.-LIF}}(\lambda)$, using the CRECK thermochemical model.

The total uncertainty for each unseeded and seeded averaged $F_{\text{NO-LIF}}(\lambda)$ profiles assuming constant $F_{\text{interf.-LIF}}(\lambda)$ results from the RSS of the random and systematic uncertainties, and is plotted in Fig. 10b. It is calculated at $\epsilon_{F_{\text{NO-LIF},\text{nsc}}}|_{\text{constant interf.-LIF}} \sim 4-18\%$, depending on the seeded level.

D.2.2. Assuming non-constant $F_{\text{interf.-LIF}}(\lambda)$

The uncertainty in $F_{\text{NO-LIF}}(\lambda)$ assuming non-constant $F_{\text{interf.-LIF}}(\lambda)$ is calculated at λ_{on} . Similar to the previous calculation, it results from both random and systemic terms.

The random error in $F_{\text{NO-LIF}}$ results from the experimental scatter and is reduced by the number of measurements performed for each flame condition. Unlike the previous methodology, it is hardly reduced by the number of images captured at each wavelength as only 120 laser shots are generated, as opposed to 5,000 in the technique assuming constant $F_{\text{interf.-LIF}}(\lambda)$. It leads to $\frac{\delta_{\text{rand}}(F_{\text{NO-LIF}})}{F_{\text{NO-LIF}}} \sim 3\%$.

The systematic term results from the propagation of the errors in the experimental boundary conditions on the fluorescence of an unseeded flame, as well as the error in $F_{\text{interf.-LIF}}(\lambda)$. For the latter, it is assumed that the uncertainty is a direct representation of the uncertainties in $F_{\text{NO-LIF},\text{sd}}(\lambda)$ and $F_{\text{NO-LIF},\text{nsc}+\text{sd}}(\lambda)$. Thus, it is calculated as the RSS of the residuals between $F_{\text{interf.-LIF}}(\lambda)$ and $F_{\text{interf.-LIF}}(\lambda)|_{\text{smoothed}}$, see Fig. 8, and is reduced by the number of points in the spectral range on which it is fitted. Similar to the previous assumption, the systematic errors in the photodiodes, the camera, and the long-pass filter are assumed nil. Hence, $\frac{\delta_{\text{sys}}(F_{\text{NO-LIF}})}{F_{\text{NO-LIF}}} \sim 8\%$ and results from the RSS of the terms presented in Fig. D.24.

The total uncertainty for each unseeded averaged $F_{\text{NO-LIF}}(\lambda)$ profiles assuming non-constant $F_{\text{interf.-LIF}}(\lambda)$ is calculated as the RSS of the random and systematic uncertainties, and is plotted in

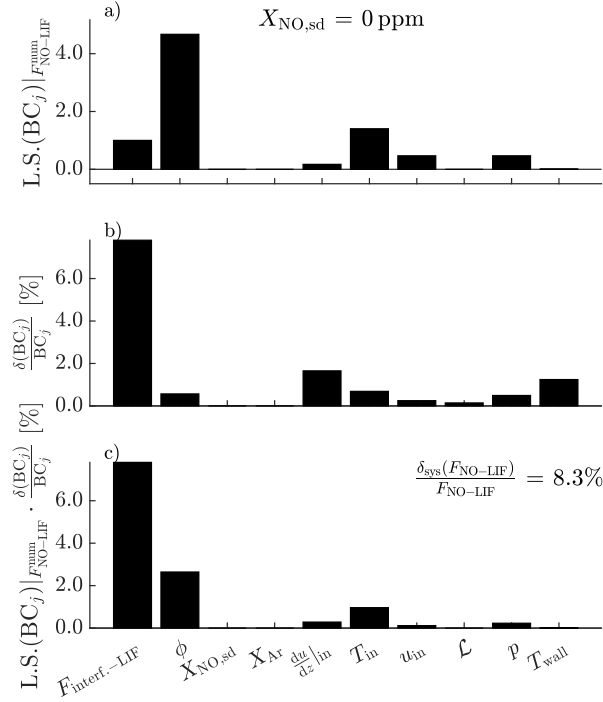


Figure D.24: L.S. (top), uncertainty (middle), and uncertainty-weighted L.S. (bottom) of the terms involved in the calculation of $\frac{\delta_{\text{sys}}(F_{\text{NO-LIF}})}{F_{\text{NO-LIF}}}$ for the Phi0.9_Tad2130K_O21 flame evaluated at $z=3$ mm, assuming non-constant $F_{\text{interf.-LIF}}(\lambda)$, using the CRECK thermochemical model.

Fig. 11b. It is evaluated as $\epsilon_{F_{\text{NO-LIF,nsct}} | \text{non-constant interf.-LIF}} \sim 9\%$.

D.3. Uncertainty on $F_{\text{NO-LIF,nsct}}/C_{\text{opt}}$

The uncertainty in $F_{\text{NO-LIF,nsct}}/C_{\text{opt}}$ results from the RSS of the random and systematic errors associated with the measurement and calculation of $F_{\text{NO-LIF,nsct}}$ and C_{opt} .

The random error is composed of the experimental scatter in the measurement of $F_{\text{NO-LIF,nsct}}^{\text{exp}}$ and $F_{\text{NO-LIF,sd}}^{\text{exp}}$, and is reduced by the number of measurements performed per flame condition. It leads to $\frac{\delta_{\text{rand}}(F_{\text{NO-LIF}}/C_{\text{opt}})}{F_{\text{NO-LIF}}/C_{\text{opt}}} \sim 0.1\%$ and 0.6% under the assumption of constant and non-constant $F_{\text{interf.-LIF}}(\lambda)$, respectively.

The systematic uncertainty encompasses the systematic error in the measurement of $F_{\text{NO-LIF,nsct}}^{\text{exp}}$ and C_{opt} . The error in $F_{\text{NO-LIF,nsct}}^{\text{exp}}$ is calculated according to the assumption formulated on $F_{\text{interf.-LIF}}(\lambda)$, as discussed previously, and is mostly driven by the propagation of the boundary condition uncertainties on $F_{\text{NO-LIF}}^{\text{num}}$. The systematic error in C_{opt} results from errors in both $F_{\text{NO-LIF,sd}}^{\text{num}}$ and $F_{\text{NO-LIF,sd}}^{\text{exp}}$. The quantification of the systematic error in $F_{\text{NO-LIF,sd}}^{\text{num}}$ would require an extensive investigation of the parameters used in the thermochemical model, Cantera, and LIFSim and was not performed in this work. Instead the scatter in the determination of C_{opt} was assumed to be representative of the combined uncertainty in $F_{\text{NO-LIF,sd}}^{\text{num}}$ and $F_{\text{NO-LIF,sd}}^{\text{exp}}$. Hence, $\frac{\delta_{\text{sys}}(F_{\text{NO-LIF}}/C_{\text{opt}})}{F_{\text{NO-LIF}}/C_{\text{opt}}} \sim 5\%$ and 11% under the assumption of constant and non-constant $F_{\text{interf.-LIF}}(\lambda)$, respectively.

The RSS of the random and systematic uncertainties leads to $\epsilon_{F_{\text{NO-LIF,nsct}}/C_{\text{opt}} | \text{constant interf.-LIF}} \sim 5.5\%$ and $\epsilon_{F_{\text{NO-LIF,nsct}}/C_{\text{opt}} | \text{non-constant interf.-LIF}} \sim 12\%$.

D.4. Uncertainty on $X_{\text{NO},\text{nscf}}$

D.4.1. Using the linear extrapolation calibration technique C_{lin}

D.4.1.1. Assuming constant $F_{\text{interf.-LIF}}(\lambda)$

The uncertainty on $X_{\text{NO},\text{nscf}}$ results from the linear fit performed between $F_{\text{NO-LIF}}$ and $X_{\text{NO},\text{sd}}$. To account for the uncertainty in $F_{\text{NO-LIF}}$, the fit is performed using a Monte-Carlo (MC) methodology. The averaged $F_{\text{NO-LIF}}$ is varied within its uncertainty range, considering a uniform distribution and assuming no uncertainty in $X_{\text{NO},\text{sd}}$ ¹¹. The fit is performed 1,000 times and the resulting $X_{\text{NO},\text{nscf}}$ is extracted through Eq. (54). The 1,000 calculations of $X_{\text{NO},\text{nscf}}$ follow a normal distribution that is fitted to obtain the nominal value (50% of the cumulative distribution function) and its uncertainty (95% confidence interval on the cumulative distribution function), as seen in Fig. D.25.

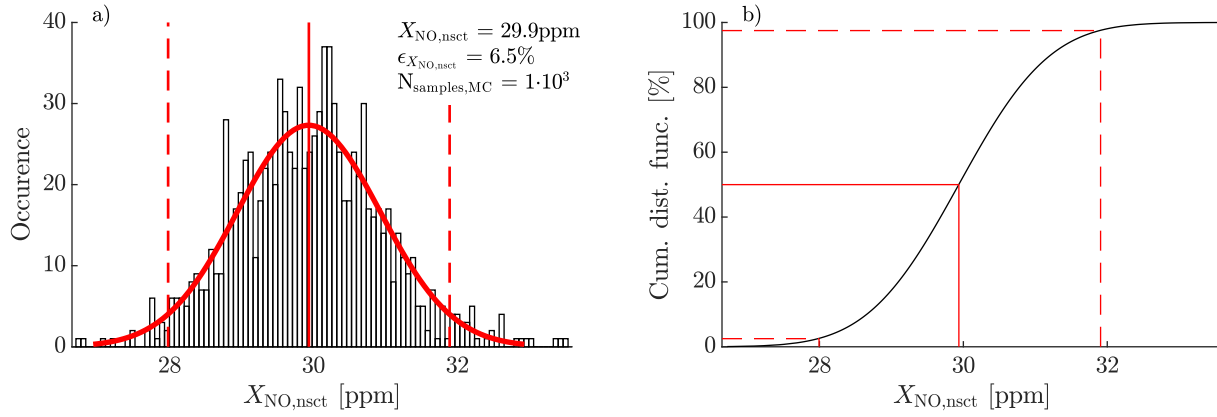


Figure D.25: Distribution of $X_{\text{NO},\text{nscf}}$ from 1,000 fits following a MC sampling technique for the flame Phi0.9_Tad2130K_O21 at $z = 3$ mm.

Using three seeding levels, this calibration technique leads to $\epsilon_{X_{\text{NO},\text{nscf}}|C_{\text{lin,constant interf.-LIF}}} \sim 6\%$, as displayed through the shaded area in Fig. 10b. An evaluation of the uncertainty was also performed by varying the number of seeded levels. An uncertainty of $\sim 15\%$ was found for one seeding level (25 ppm) and $\sim 7\%$ for two levels (25 and 50 ppm). It is evident that a larger number of seeding levels will lead to a more certain extrapolation, hence, reducing the uncertainty on $X_{\text{NO},\text{nscf}}$.

D.4.1.2. Assuming non-constant $F_{\text{interf.-LIF}}(\lambda)$

Due to the simplification that can be performed using C_{bckgd} instead of the explicit calculation of C_{lin} , see Eq. (56), a specific uncertainty calculation is performed for this method.

The uncertainty in C_{bckgd} is assumed equivalent to the the uncertainty in $F_{\text{interf.-LIF}}(\lambda)$. As performed in Section D.2.2, it results from the RSS of the residuals between $F_{\text{interf.-LIF}}(\lambda)$ and its smoothed profile, and is assumed to represent the uncertainties in both $F_{\text{NO-LIF,sd}}(\lambda)$ and $F_{\text{NO-LIF,nscf+sd}}(\lambda)$.

Hence, assuming no uncertainty in $X_{\text{NO},\text{sd}}$, the uncertainty in $X_{\text{NO},\text{nscf}}$ is calculated as the RSS of the error in $F_{\text{interf.-LIF}}(\lambda)$ (systematic) and the scatter in the calculation of $X_{\text{NO},\text{nscf}}$ that is reduced by the number of flames performed. Thus, it leads to $\epsilon_{X_{\text{NO},\text{nscf}}|C_{\text{lin,non-constant interf.-LIF}}} \sim 8.5\%$, and is plotted through the shaded area of Fig. 11c.

¹¹The uncertainty in $X_{\text{NO},\text{sd}}$ is already taken into account in the uncertainty of $F_{\text{NO-LIF}}$.

D.4.2. Using the optical calibration technique C_{opt}

As discussed previously, the calculation of this uncertainty is delicate as it would require the calculation of the uncertainty in the thermochemical model, Cantera, and LIFSim. Additionally, the calculation of $X_{\text{NO-LIF,nsct}}$ through the assumption that $f_{\text{LIF}}^{\text{exp}} = f_{\text{LIF}}^{\text{num}}$ is only valid if the thermochemical model can accurately predict the flame speed and main species concentrations. Hence, the uncertainty in $X_{\text{NO-LIF,nsct}}$ must include a term representing the inaccuracy of the model in predicting the kinetics of the flame, such as its position. A linear effect is assumed between an inaccurate prediction of the flame front position and the fluorescence generated at a given point of the domain. Hence, a numerical flame that is predicted downstream of its experimental position will lead to a lower predicted fluorescence, assuming a constant slope post-flame. Similarly, a numerical flame that is predicted upstream of the experimental flame will lead to a stronger predicted fluorescence. Thus, a systematic uncertainty on the numerical fluorescence is calculated as the delta in the flame front position between the numerical and experimental profiles. A systematic uncertainty is also present in the measurement of $F_{\text{NO-LIF,nsct}}/C_{\text{opt}}$ as discussed previously. Therefore, the systematic uncertainty in $X_{\text{NO-LIF,nsct}}$ is calculated as the RSS of $\epsilon_{F_{\text{NO-LIF,nsct}}/C_{\text{opt}}}$ and $\frac{\delta(z_f)}{z_f}$ defined as the relative error of the numerical flame front position (z_f) to the experimental one. It leads to $\frac{\delta_{\text{sys}}(X_{\text{NO-LIF,nsct}})}{X_{\text{NO-LIF,nsct}}} \sim 6.5\%$ and 12.5% under the assumption of constant and non-constant $F_{\text{interf.-LIF}}(\lambda)$, respectively, and with $\frac{\delta(z_f)}{z_f} \sim 4\%$ using the GRI thermochemical model. This points at the importance of choosing a thermochemical model that can the most accurately reproduce the flame kinetics to limit the propagation of uncertainties.

The random uncertainty results only from the scatter in $F_{\text{NO-LIF,nsct}}/C_{\text{opt}}$ and is calculated as mentioned above, leading to $\frac{\delta_{\text{rand}}(X_{\text{NO-LIF,nsct}})}{X_{\text{NO-LIF,nsct}}} \sim 0.1\%$ and 0.6% assuming constant and non-constant $F_{\text{interf.-LIF}}(\lambda)$, respectively.

The total uncertainty is calculated as the RSS of both random and systematic errors, such that $\epsilon_{X_{\text{NO,nsct}}|C_{\text{opt,constant interf.-LIF}}} \sim 6.5\%$, and $\epsilon_{X_{\text{NO,nsct}}|C_{\text{opt,non-constant interf.-LIF}}} \sim 13\%$.

D.5. Summary of uncertainties

Table D.5 presents the uncertainty calculation for each flame condition, seeding, calibration technique, and assumption.

Table D.5: Random, systematic, and total uncertainties of some keys experimental results using the different quantification techniques. All values are presented in %.

Flame		Phi0.7_Tad1830K_O21		Phi0.9_Tad2130K_O21				Phi0.9_Tad2500K_O40	
X_{sd} [ppm]		0	50	0	25	50	75	0	150
$\epsilon_{F_{NO-LIF,nsct}} \text{constant interf.-LIF}$	# samples	2	2	6	3	4	5	2	2
	rand	0.7	0.6	2.8	4.3	4.0	4.0	0.7	4.1
	sys	3.8	19.2	2.8	17.2	7.4	2.8	2.1	1.4
	total	3.9	19.2	4.0	17.8	8.5	4.8	2.2	4.4
$\epsilon_{F_{NO-LIF,nsct}} \text{non-constant interf.-LIF}$	# samples	-	-	6			-	-	
	rand	-	-	3.1			-	-	
	sys	-	-	8.3			-	-	
	total	-	-	8.9			-	-	
$\epsilon_{F_{NO-LIF,nsct}/C_{opt}} \text{constant interf.-LIF}$	# samples	2	-	6			2	-	
	rand	0.9	-	0.1			0.4	-	
	sys	5.9	-	5.3			5.0	-	
	total	6.0	-	5.4			5.1	-	
$\epsilon_{F_{NO-LIF,nsct}/C_{opt}} \text{non-constant interf.-LIF}$	# samples	-	-	6			-	-	
	rand	-	-	0.6			-	-	
	sys	-	-	11.4			-	-	
	total	-	-	11.5			-	-	
$\epsilon_{X_{NO,nsct}} C_{lin,constant interf.-LIF}$	# seeding levels	-	1	-	1	2	3	-	1
	total	-	7.8	-	14.7	6.9	6.3	-	2.7
$\epsilon_{X_{NO,nsct}} C_{lin,non-constant interf.-LIF}$	# seeding levels	-	-	-	1	2	3	-	-
	rand	-	-	-	3.2	4.5	3.9	-	-
	sys	-	-	-	6.9	7.2	7.5	-	-
	total	-	-	-	7.6	8.4	8.5	-	-
$\epsilon_{X_{NO,nsct}} C_{opt,constant interf.-LIF}$	# samples	2	-	6			2	-	
	rand	0.9	-	0.1			0.4	-	
	sys	6.1	-	6.5			11.9	-	
	total	6.2	-	6.5			11.9	-	
$\epsilon_{X_{NO,nsct}} C_{opt,non-constant interf.-LIF}$	# samples	-	-	6			-	-	
	rand	-	-	0.6			-	-	
	sys	-	-	12.5			-	-	
	total	-	-	12.6			-	-	

References

- [1] P. Singh, D. Yadav, E. S. Pandian, Link between air pollution and global climate change, in: *Global Climate Change*, Elsevier Inc., 2021, pp. 79–108. doi:<https://doi.org/10.1016/B978-0-12-822928-6.00009-5>.
- [2] J. A. Miller, C. T. Bowman, Mechanism and modeling of nitrogen chemistry in combustion, *Progress in Energy and Combustion Science* 15 (1989) 287–338. doi:[https://doi.org/10.1016/0360-1285\(89\)90017-8](https://doi.org/10.1016/0360-1285(89)90017-8).
- [3] P. Glarborg, J. A. Miller, B. Ruscic, S. J. Klippenstein, Modeling nitrogen chemistry in combustion, *Progress in Energy and Combustion Science* 67 (2018) 31–68. doi:<https://doi.org/10.1016/j.pecs.2018.01.002>.
- [4] H. J. Curran, Developing detailed chemical kinetic mechanisms for fuel combustion, *Proceedings of the Combustion Institute* 37 (2019) 57–81. doi:<https://doi.org/10.1016/j.proci.2018.06.054>.
- [5] M. C. Drake, J. W. Ratcliffe, R. J. Blint, C. D. Carter, N. M. Laurendeau, Measurements and modeling of flamefront NO formation and superequilibrium radical concentrations in laminar high-pressure premixed flames, *Symposium (International) on Combustion* 23 (1990) 387–395. doi:[https://doi.org/10.1016/S0082-0784\(06\)80283-3](https://doi.org/10.1016/S0082-0784(06)80283-3).
- [6] A. A. Konnov, I. V. Dyakov, J. De Ruyck, Probe sampling measurements and modeling of nitric oxide formation in methane-air flames, *Combustion Science and Technology* 169 (2001) 127–153. doi:<https://doi.org/10.1080/00102200108907843>.
- [7] I. V. Dyakov, J. De Ruyck, A. A. Konnov, Probe sampling measurements and modeling of nitric oxide formation in ethane + air flames, *Fuel* 86 (2007) 98–105. doi:<https://doi.org/10.1016/j.fuel.2006.06.003>.
- [8] W. Kim, H. Do, M. G. Mungal, M. A. Cappelli, Investigation of NO production and flame structure in plasma enhanced premixed combustion, *Proceedings of the Combustion Institute* 31 (2007) 3319–3326. doi:<https://doi.org/10.1016/j.proci.2006.07.107>.
- [9] J. Blauwens, B. Smets, J. Peeters, Mechanism of “prompt” NO formation in hydrocarbon flames, *Symposium (International) on Combustion* 16 (1977) 1055–1064. doi:[https://doi.org/10.1016/S0082-0784\(77\)80395-0](https://doi.org/10.1016/S0082-0784(77)80395-0).
- [10] N. Lamoureux, P. Desgroux, *In situ* laser-induced fluorescence and *Ex situ* cavity ring-down spectroscopy applied to NO measurement in flames: Microprobe perturbation and absolute quantification, *Energy and Fuels* 35 (2021) 7107–7120. doi:<https://doi.org/10.1021/acs.energyfuels.0c03806>.
- [11] H. K. Newhall, E. S. Starkman, Direct spectroscopic determination of Nitric Oxide in reciprocating engine cylinders, *SAE Technical Papers* 76 (1968) 743–762. URL: <https://www.jstor.org/stable/44553495>.
- [12] M. D. Di Rosa, A. Y. Chang, R. K. Hanson, Continuous wave dye-laser technique for simultaneous, spatially resolved measurements of temperature, pressure, and velocity of NO in an underexpanded free jet, *Applied Optics* 32 (1993) 4074. doi:<https://doi.org/10.1364/AO.32.004074>.

- [13] D. S. Liscinsky, M. F. Zabielski, *In situ* resonant ultraviolet absorption of nitric oxide at high pressure, *Measurement Science and Technology* 11 (2000) 912–919. doi:10.1088/0957-0233/11/7/307.
- [14] H. Trad, P. Higelin, C. Mounaim-Rousselle, Nitric oxide detection inside the cylinder of an SI engine by direct UV absorption spectroscopy, *Optics and Lasers in Engineering* 43 (2005) 1–18. doi:https://doi.org/10.1016/j.optlaseng.2004.06.006.
- [15] R. S. Barlow, C. D. Carter, Raman/Rayleigh/LIF measurements of Nitric Oxide formation in turbulent hydrogen jet flames, *Combustion and Flame* 97 (1994) 261–280. doi:https://doi.org/10.1016/0010-2180(94)90020-5.
- [16] J. R. Reisel, C. D. Cartel, N. M. Laurendeau, Measurements and modeling of OH and NO in premixed C₂H₆/O₂/N₂ flames at atmospheric pressure, *Energy and Fuels* 11 (1997) 1092–1100. doi:https://doi.org/10.1021/ef9700341.
- [17] C. S. Cooper, R. V. Ravikrishna, N. M. Laurendeau, Comparisons of laser-saturated, laser-induced, and planar laser-induced fluorescence measurements of nitric oxide in a lean direct-injection spray flame, *Applied Optics* 37 (1998) 4823. doi:https://doi.org/10.1364/AO.37.004823.
- [18] W. G. Bessler, C. Schulz, T. Lee, D. I. Shin, M. Hofmann, J. B. Jeffries, J. Wolfrum, R. K. Hanson, Quantitative NO-LIF imaging in high-pressure flames, *Applied Physics B: Lasers and Optics* 75 (2002) 97–102. doi:https://doi.org/10.1007/s00340-002-0946-0.
- [19] N. Chai, W. D. Kulatilaka, S. V. Naik, N. M. Laurendeau, R. P. Lucht, J. P. Kuehner, S. Roy, V. R. Katta, J. R. Gord, Nitric Oxide concentration measurements in atmospheric pressure flames using electronic-resonance-enhanced coherent anti-Stokes Raman scattering, *Applied Physics B: Lasers and Optics* 88 (2007) 141–150. doi:https://doi.org/10.1007/s00340-007-2647-1.
- [20] L. Pillier, M. Idir, J. Molet, A. Matynia, S. De Persis, Experimental study and modelling of NO_x formation in high pressure counter-flow premixed CH₄/air flames, *Fuel* 150 (2015) 394–407. doi:https://doi.org/10.1016/j.fuel.2015.01.099.
- [21] C. Brackmann, T. Methling, M. Lubrano Lavadera, G. Capriolo, A. A. Konnov, Experimental and modeling study of nitric oxide formation in premixed methanol + air flames, *Combustion and Flame* 213 (2020) 322–330. doi:https://doi.org/10.1016/j.combustflame.2019.11.043.
- [22] P. Versailles, A. Durocher, G. Bourque, J. M. Berghthorson, Effect of high pressures on the formation of nitric oxide in lean, premixed flames, *Journal of Engineering for Gas Turbines and Power* 143 (2021) 051029. doi:https://doi.org/10.1115/1.4047748.
- [23] A. C. Eckbreth, *Laser diagnostics for combustion temperature and species*, second ed., 1996. doi:https://doi.org/10.1201/9781003077251.
- [24] K. Kohse-Höinghaus, Laser techniques for the quantitative detection of reactive intermediates in combustion systems, *Progress in Energy and Combustion Science* 20 (1994) 203–279. doi:https://doi.org/10.1016/0360-1285(94)90015-9.
- [25] A. Steinberg, S. Roy, *Optical diagnostics for reacting and non-reacting flows: Theory and Practice*, volume 264, 2023. doi:https://doi.org/10.2514/4.106330.

- [26] J. W. Daily, Laser induced fluorescence spectroscopy in flames, *Progress in Energy and Combustion Science* 23 (1997) 133–199. doi:[https://doi.org/10.1016/S0360-1285\(97\)00008-7](https://doi.org/10.1016/S0360-1285(97)00008-7).
- [27] N. M. Laurendeau, *Statistical thermodynamics: Fundamentals and applications*, 2005.
- [28] R. K. Hanson, R. M. Spearrin, C. S. Goldenstein, *Spectroscopy and optical diagnostics for gases*, 2016.
- [29] J. Brzozowski, P. Erman, M. Lyyra, Predissociation rates and perturbations of the A, B, B', C, D and F states in NO studied using time resolved spectroscopy, *Physica Scripta* 14 (1976) 290–297. doi:10.1088/0031-8949/14/6/009.
- [30] J. Luque, D. R. Crosley, Radiative and predissociative rates for NO $A^2\Sigma^+\nu' = 0 - 5$ and $D^2\Sigma^+\nu' = 0 - 3$, *Journal of Chemical Physics* 112 (2000) 9411–9416. doi:<https://doi.org/10.1063/1.481560>.
- [31] J. B. Simeonsson, S. A. Elwood, M. Niebes, R. Carter, A. Peck, Trace detection of NO and NO₂ by photoionization and laser induced fluorescence techniques, *Analytica Chimica Acta* 397 (1999) 33–41. doi:[https://doi.org/10.1016/S0003-2670\(99\)00389-X](https://doi.org/10.1016/S0003-2670(99)00389-X).
- [32] W. G. Bessler, C. Schulz, S. Volker, J. W. Daily, A versatile modeling tool for nitric oxide LIF spectra, in: *Proceedings of the Third Joint Meeting of the U.S. Sections of The Combustion Institute*, Chicago, 2003, p. P105.
- [33] P. Versailles, G. M. G. Watson, A. C. A. Lipardi, J. M. Bergthorson, Quantitative CH measurements in atmospheric-pressure, premixed flames of C₁-C₄ alkanes, *Combustion and Flame* 165 (2016) 109–124. doi:<https://doi.org/10.1016/j.combustflame.2015.11.001>.
- [34] S. V. Naik, N. M. Laurendeau, Spectroscopic, calibration and RET issues for linear laser-induced fluorescence measurements of nitric oxide in high-pressure diffusion flames, *Applied Physics B: Lasers and Optics* 79 (2004) 641–651. doi:<https://doi.org/10.1007/s00340-004-1604-5>.
- [35] T. Verreycken, R. M. Van Der Horst, N. Sadeghi, P. J. Bruggeman, Absolute calibration of OH density in a nanosecond pulsed plasma filament in atmospheric pressure He-H₂O: Comparison of independent calibration methods, *Journal of Physics D: Applied Physics* 46 (2013). doi:10.1088/0022-3727/46/46/464004.
- [36] J. W. Daily, W. G. Bessler, C. Schulz, V. Sick, T. B. Settersten, Role of nonstationary collisional dynamics in determining nitric oxide LIF spectra, in: *42nd AIAA Aerospace Sciences Meeting and Exhibit*, January, 2004. doi:<https://doi.org/10.2514/6.2004-389>.
- [37] W. P. Partridge, N. M. Laurendeau, Formulation of a dimensionless overlap fraction to account for spectrally distributed interactions in fluorescence studies, *Applied Optics* 34 (1995) 2645. doi:<https://doi.org/10.1364/AO.34.002645>.
- [38] J. Luque, D. R. Crosley, LIFBASE Version 2.1.1, Database and spectral simulation for diatomic molecules (v1.6), 1999.
- [39] J. R. Reisel, C. D. Carter, N. M. Laurendeau, M. C. Drake, Laser-saturated fluorescence measurements of nitric oxide in laminar, flat, C₂H₁₆/O₂/N₂ flames at atmospheric pressure, *Combustion Science and Technology* 91 (1993) 271–295. doi:<https://doi.org/10.1080/00102209308907649>.

- [40] P. Versailles, CH formation in premixed flames of C₁-C₄ alkanes: assessment of current chemical modelling capability against experiments, Phd, McGill University, 2017.
- [41] W. G. Bessler, C. Schulz, T. Lee, J. B. Jeffries, R. K. Hanson, Carbon dioxide UV laser-induced fluorescence in high-pressure flames, *Chemical Physics Letters* 375 (2003) 344–349. doi:[https://doi.org/10.1016/S0009-2614\(03\)00858-3](https://doi.org/10.1016/S0009-2614(03)00858-3).
- [42] P. Versailles, A. Durocher, G. Bourque, J. M. Bergthorson, Nitric oxide formation in lean, methane-air stagnation flames at supra-atmospheric pressures, *Proceedings of the Combustion Institute* 37 (2019) 711–718. doi:<https://doi.org/10.1016/j.proci.2018.05.060>.
- [43] A. Durocher, M. Meulemans, G. Bourque, J. M. Bergthorson, Nitric oxide concentration measurements in low-temperature, premixed hydrogen-air stagnation flames at elevated pressures, *Proceedings of the Combustion Institute* 39 (2023) 541–550. doi:<https://doi.org/10.1016/j.proci.2022.08.003>.
- [44] P. A. Berg, G. P. Smith, J. B. Jeffries, D. R. Crosley, Nitric oxide formation and reburn in low-pressure methane flames, *Symposium (International) on Combustion* 27 (1998) 1377–1384. doi:[https://doi.org/10.1016/S0082-0784\(98\)80543-2](https://doi.org/10.1016/S0082-0784(98)80543-2).
- [45] G. Suck, J. Jakobs, S. Nicklitzsch, T. Lee, W. G. Bessler, M. Hofmann, F. Zimmermann, C. Schulz, NO Laser-Induced Fluorescence Imaging in the Combustion Chamber of a Spray-Guided Direct-Injection Gasoline Engine, *SAE International* 113 (2004) 1043–1056. URL: <https://www.jstor.org/stable/44740824>.
- [46] T. Lee, J. B. Jeffries, R. K. Hanson, Experimental evaluation of strategies for quantitative laser-induced- fluorescence imaging of nitric oxide in high-pressure flames (1-60 bar), *Proceedings of the Combustion Institute* 31 (2007) 757–764. doi:<https://doi.org/10.1016/j.proci.2006.07.090>.
- [47] G. M. Watson, J. D. Munzar, J. M. Bergthorson, NO formation in model syngas and biogas blends, *Fuel* 124 (2014) 113–124. doi:<https://doi.org/10.1016/j.fuel.2014.01.079>.
- [48] A. B. Sahu, R. V. Ravikrishna, Quantitative LIF measurements and kinetics assessment of NO formation in H₂/CO syngas–air counterflow diffusion flames, *Combustion and Flame* 173 (2016) 208–228. doi:<https://doi.org/10.1016/j.combustflame.2016.09.003>.
- [49] G. M. G. Watson, P. Versailles, J. M. Bergthorson, NO formation in premixed flames of C₁-C₃ alkanes and alcohols, *Combustion and Flame* 169 (2016) 242–260. doi:<https://doi.org/10.1016/j.combustflame.2016.04.015>.
- [50] A. Durocher, M. Meulemans, P. Versailles, G. Bourque, J. M. Bergthorson, Back to basics - NO concentration measurements in atmospheric lean-to-rich, low-temperature, premixed hydrogen-air flames diluted with argon, *Proceedings of the Combustion Institute* 38 (2021) 2093–2100. doi:<https://doi.org/10.1016/j.proci.2020.06.124>.
- [51] M. Meulemans, A. Durocher, G. Bourque, J. M. Bergthorson, NO measurements in high temperature hydrogen flames : The crucial role of the hydrogen oxidation chemistry for accurate NO predictions, *Combustion and Flame* 261 (2024) 113279. doi:<https://doi.org/10.1016/j.combustflame.2023.113279>.

- [52] M. Uddi, N. Jiang, I. V. Adamovich, W. R. Lempert, Nitric oxide density measurements in air and air/fuel nanosecond pulse discharges by laser induced fluorescence, *Journal of Physics D: Applied Physics* 42 (2009) 075205. doi:10.1088/0022-3727/42/7/075205.
- [53] G. Cunge, J. P. Booth, J. Derouard, Absolute concentration measurements by pulsed laser-induced fluorescence in low-pressure gases: Allowing for saturation effects, *Chemical Physics Letters* 263 (1996) 645–650. doi:https://doi.org/10.1016/S0009-2614(96)01259-6.
- [54] M. Engelhard, W. Jacob, W. Möller, A. W. Koch, New calibration method for the determination of the absolute density of CH radicals through laser-induced fluorescence, *Applied Optics* 34 (1995) 4542. doi:10.1364/ao.34.004542.
- [55] P. A. Berg, D. A. Hill, A. R. Noble, G. P. Smith, J. B. Jeffries, D. R. Crosley, Absolute CH concentration measurements in low-pressure methane flames: Comparisons with model results, *Combustion and Flame* 121 (2000) 223–235. doi:10.1016/S0010-2180(99)00130-3.
- [56] K. T. Walsh, M. B. Long, M. A. Tanoff, M. D. Smooke, Experimental and computational study of CH, CH*, and OH* in an axisymmetric laminar diffusion flame, *Symposium (International) on Combustion* 27 (1998) 615–623. doi:10.1016/S0082-0784(98)80453-0.
- [57] J. T. Salmon, N. M. Laurendeau, Calibration of laser-saturated fluorescence measurements using Rayleigh scattering, *Applied Optics* 24 (1985) 65. doi:10.1364/ao.24.000065.
- [58] J. Luque, D. R. Crosley, Absolute CH concentrations in low-pressure flames measured with laser-induced fluorescence, *Applied Physics B: Lasers and Optics* 63 (1996) 91–98. doi:10.1007/BF01112843.
- [59] J. Luque, R. J. Klein-Douwel, J. B. Jeffries, G. P. Smith, D. R. Crosley, Quantitative laser-induced fluorescence of CH in atmospheric pressure flames, *Applied Physics B: Lasers and Optics* 75 (2002) 779–790. doi:https://doi.org/10.1007/s00340-002-1038-x.
- [60] D. E. Thomas, K. P. Shrestha, F. Mauss, W. F. Northrop, Extinction and NO formation of ammonia-hydrogen and air non-premixed counterflow flames, *Proceedings of the Combustion Institute* 39 (2023) 1803–1812. doi:https://doi.org/10.1016/j.proci.2022.08.067.
- [61] P. C. Palma, P. M. Danehy, A. F. Houwing, Fluorescence imaging of rotational and vibrational temperature in shock-tunnel nozzle flow, *AIAA Journal* 41 (2003) 1722–1732. doi:https://doi.org/10.2514/2.7290.
- [62] I. A. Mulla, G. Godard, G. Cabot, F. Grisch, B. Renou, Quantitative imaging of nitric oxide concentration in a turbulent *n*-heptane spray flame, *Combustion and Flame* 203 (2019) 217–229. doi:https://doi.org/10.1016/j.combustflame.2019.02.005.
- [63] M. Meulemans, A. Durocher, P. Versailles, G. Bourque, J. M. Bergthorson, How well do we know thermal-NO? An investigation of NO formation in flames over a wide temperature range, *Proceedings of the Combustion Institute* 39 (2023) 521–529. doi:https://doi.org/10.1016/j.proci.2022.07.189.
- [64] A. Durocher, M. Meulemans, G. Bourque, J. M. Bergthorson, Measurements of the laminar flame speed of premixed, hydrogen-air-argon stagnation flames, *Applications in Energy and Combustion Science* 7 (2021) 100028. doi:https://doi.org/10.1016/j.jaecs.2021.100028.

- [65] M. Zimmermann, N. Lindlein, R. Voelkel, K. J. Weible, Microlens laser beam homogenizer - from theory to application, *Laser Beam Shaping VIII* 6663 (2007) 666302. doi:<https://doi.org/10.1117/12.731391>.
- [66] M. D. Di Rosa, K. G. Klavuhn, R. K. Hanson, LIF spectroscopy of NO and O₂ in high-pressure flames, *Combustion Science and Technology* 118 (1996) 257–283. doi:10.1080/00102209608951981.
- [67] W. G. Bessler, C. Schulz, T. Lee, J. B. Jeffries, R. K. Hanson, Strategies for laser-induced fluorescence detection of nitric oxide in high-pressure flames. I. A–X(0,0) excitation, *Applied Optics* 41 (2002) 3547. doi:<https://doi.org/10.1364/AO.41.003547>.
- [68] D. G. Goodwin, H. K. Moffat, I. Schoegl, R. L. Speth, B. W. Weber, Cantera: An object-oriented software toolkit for chemical kinetics, thermodynamics, and transport processes (v.3.0.0), 2023.
- [69] G. Bagheri, E. Ranzi, M. Pelucchi, A. Parente, A. Frassoldati, T. Faravelli, Comprehensive kinetic study of combustion technologies for low environmental impact: MILD and OXY-fuel combustion of methane, *Combustion and Flame* 212 (2020) 142–155. doi:<https://doi.org/10.1016/j.combustflame.2019.10.014>.
- [70] Y. Song, L. Marrodán, N. Vin, O. Herbinet, E. Assaf, C. Fittschen, A. Stagni, T. Faravelli, M. U. Alzueta, F. Battin-Leclerc, The sensitizing effects of NO₂ and NO on methane low temperature oxidation in a jet stirred reactor, *Proceedings of the Combustion Institute* 37 (2019) 667–675. doi:<https://doi.org/10.1016/j.proci.2018.06.115>.
- [71] G. P. Smith, D. M. Golden, M. Frenklach, N. W. Moriarty, B. Eiteneer, M. Goldenberg, T. Bowman, R. K. Hanson, S. Song, W. C. Gardiner, V. V. Lissianski, Z. Qin, *GRI-Mech 3.0* (1999).
- [72] University of California at San Diego, *Chemical-Kinetic Mechanisms for Combustion Applications*, 2016.
- [73] P. H. Paul, C. Carter, J. A. Gray, J. L. Durant, J. Thomson, M. Furlanetto, Correlations for the NO A²Σ⁺ (ν'=0) electronic quenching cross-section, Technical Report, Sandia National Lab. (SNL-CA), Livermore, CA (United States), 1995.
- [74] P. H. Paul, J. A. Gray, J. L. Durant, J. W. Thoman, A model for temperature-dependent collisional quenching of NO A²Σ⁺, *Applied Physics B Photophysics and Laser Chemistry* 57 (1993) 249–259. doi:<https://doi.org/10.1007/BF00325203>.
- [75] M. Tamura, P. A. Berg, J. E. Harrington, J. Luque, J. B. Jeffries, G. P. Smith, D. R. Crosley, Collisional quenching of CH(A), OH(A), and NO(A) in low pressure hydrocarbon flames, *Combustion and Flame* 114 (1998) 502–514. doi:[https://doi.org/10.1016/S0010-2180\(97\)00324-6](https://doi.org/10.1016/S0010-2180(97)00324-6).
- [76] T. B. Settersten, B. D. Patterson, J. A. Gray, Temperature- and species-dependent quenching of NO A²Σ⁺ (ν'=0) probed by two-photon laser-induced fluorescence using a picosecond laser, *Journal of Chemical Physics* 124 (2006). doi:<https://doi.org/10.1063/1.2206783>.
- [77] T. B. Settersten, B. D. Patterson, C. D. Carter, Collisional quenching of NO A²Σ⁺ (ν'=0) between 125 and 294 K, *Journal of Chemical Physics* 130 (2009) 204302. doi:<https://doi.org/10.1063/1.3138178>.

- [78] B. C. Connelly, B. A. V. Bennett, M. D. Smooke, M. B. Long, A paradigm shift in the interaction of experiments and computations in combustion research, *Proceedings of the Combustion Institute* 32 (2009) 879–886. doi:<https://doi.org/10.1016/j.proci.2008.05.066>.
- [79] R. V. Ravikrishna, S. V. Naik, C. S. Cooper, N. M. Laurendeau, Quantitative laser-induced fluorescence measurements and modeling of nitric oxide in high-pressure (6-15 atm) counterflow diffusion flames, *Combustion Science and Technology* 176 (2004) 1–21. doi:<https://doi.org/10.1080/00102200490267331>.
- [80] A. Y. Chang, M. D. DiRosa, R. K. Hanson, Temperature dependence of collision broadening and shift in the NO A ← X(0, 0) band in the presence of argon and nitrogen, *Journal of Quantitative Spectroscopy and Radiative Transfer* 47 (1992) 375–390. doi:[https://doi.org/10.1016/0022-4073\(92\)90039-7](https://doi.org/10.1016/0022-4073(92)90039-7).
- [81] M. D. Di Rosa, R. K. Hanson, Collision-broadening and -shift of NO $\gamma(0,0)$ absorption lines by H₂O, O₂, and NO at 295K, *Journal of Molecular Spectroscopy* 164 (1994) 97–117. doi:<https://doi.org/10.1006/jmsp.1994.1059>.
- [82] M. D. DiRosa, High-resolution line shape spectroscopy of transitions in the gamma bands of nitric oxide, Ph.D. thesis, 1996.